

## **NOTE TO USERS**

**This reproduction is the best copy available.**

UMI<sup>o</sup>



*Vector Voltage Measurement of RFICs  
using Electrostatic Force Microscopy*

by

**Chris Falkingham**

A thesis  
submitted to the Faculty of Graduate Studies  
in partial fulfillment of the requirements  
for the degree of

**Master of Science**

Department of Electrical and Computer Engineering  
University of Manitoba  
Winnipeg, Manitoba  
Canada

©Chris Falkingham  
2001



National Library  
of Canada

Acquisitions and  
Bibliographic Services

395 Wellington Street  
Ottawa ON K1A 0N4  
Canada

Bibliothèque nationale  
du Canada

Acquisitions et  
services bibliographiques

395, rue Wellington  
Ottawa ON K1A 0N4  
Canada

*Your file Votre référence*

*Our file Notre référence*

The author has granted a non-exclusive licence allowing the National Library of Canada to reproduce, loan, distribute or sell copies of this thesis in microform, paper or electronic formats.

The author retains ownership of the copyright in this thesis. Neither the thesis nor substantial extracts from it may be printed or otherwise reproduced without the author's permission.

L'auteur a accordé une licence non exclusive permettant à la Bibliothèque nationale du Canada de reproduire, prêter, distribuer ou vendre des copies de cette thèse sous la forme de microfiche/film, de reproduction sur papier ou sur format électronique.

L'auteur conserve la propriété du droit d'auteur qui protège cette thèse. Ni la thèse ni des extraits substantiels de celle-ci ne doivent être imprimés ou autrement reproduits sans son autorisation.

0-612-57538-1

**Canada**

**THE UNIVERSITY OF MANITOBA**  
**FACULTY OF GRADUATE STUDIES**  
\*\*\*\*\*  
**COPYRIGHT PERMISSION PAGE**

**Vector Voltage Measurement of RFICs using Electrostatic Force Microscopy**

**BY**

**Chris Falkingham**

**A Thesis/Practicum submitted to the Faculty of Graduate Studies of The University  
of Manitoba in partial fulfillment of the requirements of the degree  
of  
Master of Science**

**CHRIS FALKINGHAM © 2001**

**Permission has been granted to the Library of The University of Manitoba to lend or sell copies of this thesis/practicum, to the National Library of Canada to microfilm this thesis/practicum and to lend or sell copies of the film, and to Dissertations Abstracts International to publish an abstract of this thesis/practicum.**

**The author reserves other publication rights, and neither this thesis/practicum nor extensive extracts from it may be printed or otherwise reproduced without the author's written permission.**

## ***Abstract***

The capability of internal node probing is becoming increasingly important in the field of microelectronics. Both digital and analog circuits are becoming increasingly dense as many different devices are interacting with each other on a mutual die. In these circuits, network ports are not available therefore an internal node probing technique must be employed. The ideal internal node probing instrument must be non-invasive, have high spatial resolution, a large dynamic range and have easy sample preparation.

In this research, a novel probing scheme will be introduced that employs scanning force probing techniques. The technique involves placing a small micromachined probe in close proximity to a measurement conductor. A voltage is driven onto the probe which causes a non-linear electrostatic force between the probe and measurement conductor. The applied force will cause the probe to deflect which can be measured to infer information about the signal of interest. In this research, the technique will be adapted for vector voltage measurement of RFICs.

Hardware and software implementations using I/Q modulation will be introduced to facilitate amplitude and phase measurement. Measurements will be made on several practical circuits which include: a Texas Instruments LNA, a GaAs single stage amplifier, a Nortel provided phase shifter and a wideband amplifier. The instrument's measurement capability will be demonstrated from 1 to 16 GHz. Higher frequency measurement techniques such as frequency upconversion will be explored and demonstrated at 16 GHz.

## ***Acknowledgements***

Written by Chris Falkingham.  
Patiently advised and supervised by Dr. Greg Bridges.  
Draft editing: Dr. Greg Bridges and Chris Falkingham  
References search assisted by Engineering librarians and the people who compiled the  
"reference/publication folders" in the SPM lab.  
Concept of vector voltage measurement conceived by Dr. Greg Bridges,  
Dr. R.A. Said, and D.J. Thomson.  
Micromachined cantilevers purchased by Dr. Greg Bridges.  
Mounting of the cantilever onto a circuit board and the mechanical probing structures by  
Dr. Greg Bridges and Chris Falkingham.  
Optical Beam Deflection Sensor on the mechanical probing structures were designed and  
manufactured by Richard Qi and Micron Force Instruments (MFI), respectively.  
Simulation results in Fig. 7.3 and 8.1 were provided by Dr. Greg Bridges  
All microphotographs supplied by Dr. Greg Bridges.  
Computer Software for automating the experiments by Chris Falkingham.  
All experimental implementations by Chris Falkingham.  
All measurements performed by Chris Falkingham.  
Equipments and commercial devices purchased by Dr. Greg Bridges with financial  
support by Natural Sciences and Engineering Research Council (NSERC), the Canadian  
Microelectronics Corporation (CMC), and Micronet.  
Cadence and HspiceS managed by Guy Jonatschuk.  
Single stage mesfet amplifier designed by Sunny Cheung and fabricated through CMC.  
LNA provided by Texas Instruments.  
10 GHz phase shifter provided by Nortel Networks.  
Wideband distributed amplifier provided by Nortel Networks.

## *Table of Contents*

Abstract.....	ii
Acknowledgements.....	iii
List of Figures.....	vii
List of Tables.....	xiii
List of Nomenclature.....	xiv
Chapter 1: Introduction	
1.1 Internal Node Test.....	1
1.2 Thesis Outline.....	2
Chapter 2: IC Probing Techniques	
2.1 Introduction to IC Probing.....	3
2.2 Contact Probes	
2.2.1 Low Impedance Probes.....	4
2.2.2 Medium Impedance Probes.....	5
2.2.3 High Impedance Probes.....	6
2.3 Repetitive Sampling Technique.....	8
2.4 Electro-Optic Probing.....	10
2.5 Electron Beam Probing.....	13
2.6 Photoconductive Sampling.....	15
Chapter 3: Scanning Force Probing	
3.1 Scanning Probe Microscopy.....	17
3.2 Micromachined Cantilevers.....	17
3.3 Mechanical Frequency Response.....	18
3.4 Deflection Sensors.....	20
3.4.1 Fiber Interferometer Technique.....	20
3.4.2 Tunnelling Electron Sensor.....	22
3.4.3 Laser Beam Bounce Method.....	22
3.5 Electrostatic Force Microscopy(EFM).....	25
3.6 Internal Node DC Voltage Measurements.....	26
3.7 High Frequency Internal Node Probing.....	29
3.8 Pulse Sampling Technique.....	32
3.9 Sinusoidal Sampling Technique.....	33
3.10 Heterodyne Nulling Technique.....	35
3.11 Measurement of Passivated Circuits.....	36
3.12 Sensitivity.....	37
3.13 Mechanical Structure of the EFM Probe Station.....	40
3.14 Summary.....	41
Chapter 4: Vector Voltage Measurements at 1 and 2 GHz	
4.1 Introduction.....	42
4.2 Hardware Description.....	42
4.3 1 GHz Hardware Description and Calibration.....	45

4.4 Measurement of a Texas Instruments LNA .....	49
4.5 1.9 GHz Hardware Description and Calibration .....	53
4.6 Measurement of a Mesfet Amplifier .....	54
4.7 Summary .....	58
 Chapter 5: I/Q Modulation	
5.1 Modulation Problem .....	59
5.2 Theory of I/Q Modulation .....	60
5.3 I/Q Modulation in EFM.....	62
5.4 GTMicrowave I/Q Modulator .....	63
5.5 I/Q Modulator Hardware Description .....	64
5.6 Software Interface .....	65
5.7 Automation of the Heterodyne Nulling Technique .....	66
5.8 Summary .....	70
 Chapter 6: Vector Voltage Measurements at 10 GHz	
6.1 Introduction .....	71
6.2 10 GHz Hardware Description.....	71
6.3 10 GHz Calibration of the I/Q Modulator .....	72
6.4 Vector Voltage Measurements of a CPW at 10 GHz.....	75
6.5 Amplitude and Phase Profiling of Transmission Lines .....	77
6.6 Measurement of a 10 GHz Phase Shifter.....	81
6.7 Measurement of a Distributed Amplifier .....	84
6.7.1 VSWR Measurement.....	86
6.7.2 Transmission Line Effects on Power/Ground Metal .....	88
6.7.3 Insertion Loss Measurement of Output T-Line .....	93
6.7.4 Internal Node Measurements of Distributed Amplifier .....	95
6.8 Summary .....	96
 Chapter 7: Invasiveness	
7.1 Invasiveness Model .....	98
7.2 Invasiveness in EFM .....	99
7.3 Simulation of Loading Capacitance.....	100
7.4 Probe Parasitic Capacitance.....	101
7.5 Capacitance Estimation on a MHIC 50 Ohm Microstrip.....	102
7.6 Capacitance Estimation using Small CPW Structures.....	106
7.7 Capacitance Estimation using Coupled Line Resonator .....	107
7.8 Summary .....	108
 Chapter 8: Spatial Resolution	
8.1 Definition of Spatial Resolution in EFM.....	109
8.2 Generalized Spatial Resolution in EFM .....	111
8.3 Amplitude and Phase Profile along Cross-Section of a CPW .....	114
8.4 Measured Amplitude Variation with Probe to Circuit Spacing .....	117
8.5 Summary .....	122

<b>Chapter 9: Vector Voltage Measurements at 16 GHz</b>	
9.1 High Frequency Considerations. . . . .	124
9.2 Hardware Description . . . . .	125
9.3 I/Q Modulator Calibration at 16 GHz . . . . .	126
9.4 Vector Measurements on a CPW Structure . . . . .	129
9.5 Measurement of a Distributed Amplifier at 16 GHz . . . . .	132
9.5.1 Insertion Loss Measurement of Output T-Line . . . . .	132
9.5.2 Amplitude and Phase Profile of Distributed Amplifier . . . . .	134
9.6 Summary . . . . .	136
<b>Chapter 10: Vector Voltage Measurements using Frequency Upconversion</b>	
10.1 High Frequency Sinusoidal Measurement. . . . .	137
10.2 Extending EFM for Higher Frequency Probing. . . . .	137
10.3 High Frequency EFM Hardware Description . . . . .	138
10.4 16 GHz Measurements using Frequency Upconversion . . . . .	142
10.4.1 Relcom Mixer Characterization at 1.95 GHz . . . . .	144
10.4.2 Upconversion Mixer Characterization. . . . .	145
10.4.3 Sideband Rejection Filters. . . . .	146
10.5 Transmission Line Measurements using Frequency Upconversion. . . . .	147
10.5.1 Phase Measurements . . . . .	148
10.5.2 Amplitude Measurements . . . . .	149
10.6 Summary . . . . .	150
<b>Chapter 11: Conclusions and Future Considerations</b>	
11.1 Concluding Remarks . . . . .	152
<b>References. . . . .</b>	<b>153</b>

## *List of Figures*

Fig. 1.1:	Internal node test. . . . .	1
Fig. 2.1:	50 Ohm matched impedance probe . . . . .	4
Fig. 2.2:	Resistive divider probe . . . . .	5
Fig. 2.3:	Passive high impedance probe. . . . .	6
Fig. 2.4:	Active high impedance probe . . . . .	7
Fig. 2.5:	Repetitive sampling technique #1 . . . . .	8
Fig. 2.6:	Repetitive sampling technique #2 . . . . .	9
Fig. 2.7:	Polarization shift in presence of electric field . . . . .	10
Fig. 2.8:	(a) Probing using electro-optic substrate (b) Probing using electro-optic crystal . . . . .	11
Fig. 2.9:	Electro-optic probing instrument. . . . .	12
Fig. 2.10:	Energy representation of electron emission. . . . .	13
Fig. 2.11:	E-Beam implementation . . . . .	14
Fig. 2.12:	Photoconductive sampling contact probe . . . . .	15
Fig. 3.1:	Silicon cantilever with conical tip . . . . .	18
Fig. 3.2:	Mechanical system transfer function. . . . .	19
Fig. 3.3:	Measured mechanical noise spectrum . . . . .	20
Fig. 3.4:	Fiber interferometer deflection sensor . . . . .	21
Fig. 3.5:	Reflection characteristic as a function of probe deflection . . . . .	21
Fig. 3.6:	Laser beam bounce method . . . . .	23
Fig. 3.7:	Electrostatic interaction between probe and measurement conductor. . . . .	25
Fig. 3.8:	Non-contact DC voltage measurement . . . . .	27
Fig. 3.9:	Non-contact DC measurement scheme . . . . .	28

Fig. 3.10:	Lockin amplifier block diagram. . . . .	29
Fig. 3.11:	Generic high frequency EFM measurement scheme. . . . .	30
Fig. 3.12:	High frequency circuit and probe signals . . . . .	31
Fig. 3.13:	Pulse sampling waveforms . . . . .	32
Fig. 3.14:	Sinusoidal sampling technique . . . . .	34
Fig. 3.15:	Sinusoidal sampling block diagram. . . . .	34
Fig. 3.16:	Heterodyne Nulling Technique . . . . .	35
Fig. 3.17:	Amplitude nulling at different probe to circuit spacings. . . . .	36
Fig. 3.18:	Noise transfer characteristic of probe . . . . .	37
Fig. 3.19:	Theoretical and experimental deflection noise density . . . . .	38
Fig. 3.20:	Sample sensitivity calculation for 200 nm probe to circuit spacing . . . . .	40
Fig. 3.21:	Photograph of EFM probing instrument . . . . .	41
Fig. 4.1:	Sinusoidal sampling hardware configuration. . . . .	42
Fig. 4.2:	Matching network using adjustable phase shifter . . . . .	43
Fig. 4.3:	Series attenuator matching scheme . . . . .	44
Fig. 4.4:	1 GHz measurement hardware block diagram. . . . .	45
Fig. 4.5:	1 GHz calibration setup . . . . .	46
Fig. 4.6:	Calibration curve at 1 GHz . . . . .	46
Fig. 4.7:	Mixer harmonics at 1 GHz . . . . .	47
Fig. 4.8:	Minicircuits TFM-2 mixer characteristic. . . . .	48
Fig. 4.9:	1 GHz deflection versus probe phase. . . . .	49
Fig. 4.10:	Circuit schematic of TI LNA. . . . .	50
Fig. 4.11:	TI LNA package and microphotograph of circuit die . . . . .	51

Fig. 4.12:	1.9 GHz calibration curve . . . . .	53
Fig. 4.13:	Circuit schematic of single stage GaAs amplifier . . . . .	54
Fig. 4.14:	GaAs amplifier layout . . . . .	54
Fig. 4.15:	Measurement setup for the GaAs amplifier . . . . .	55
Fig. 4.16:	Amplifier layout along with measurement points . . . . .	55
Fig. 4.17:	Simplified mesfet model . . . . .	57
Fig. 5.1:	Conventional modulation scheme . . . . .	59
Fig. 5.2:	Equivalence using I/Q modulation. . . . .	60
Fig. 5.3:	Internal block diagram of I/Q modulator. . . . .	61
Fig. 5.4:	2 dimensional I/Q space. . . . .	61
Fig. 5.5:	Required modulation vectors. . . . .	62
Fig. 5.6:	Output amplitude versus 12 bit control word . . . . .	63
Fig. 5.7:	Modulation using a multiplexer. . . . .	64
Fig. 5.8:	I/Q modulator hardware interface . . . . .	65
Fig. 5.9:	I/Q modulator software driver . . . . .	66
Fig. 5.10:	Typical nulling control system. . . . .	67
Fig. 5.11:	Modelling the lockin amplifier transfer function for phase nulling. . . . .	68
Fig. 5.12:	Lockin amplifier output deflection characteristic during phase nulling . . . . .	68
Fig. 5.13:	Deflection versus A parameter. . . . .	69
Fig. 5.14:	Nulling digital control system . . . . .	70
Fig. 6.1:	10 GHz EFM hardware configuration . . . . .	71
Fig. 6.2:	I/Q modulator calibration configuration . . . . .	72
Fig. 6.3:	I and Q attenuator characteristics . . . . .	73

Fig. 6.4:	Compensated attenuator characteristics. . . . .	74
Fig. 6.5:	Calibration CPW structure. . . . .	75
Fig. 6.6:	(a) Vector measurements compared to network analyzer (b) Calibration curve . . . . .	76
Fig. 6.7:	Open-circuited 50 Ohm CPW structure. . . . .	77
Fig. 6.8:	Standing wave measurement of CPW . . . . .	78
Fig. 6.9:	Travelling wave line. . . . .	79
Fig. 6.10:	Phase distribution along travelling wave line . . . . .	80
Fig. 6.11:	Nortel phase shifter circuit. . . . .	81
Fig. 6.12:	Internal node phase measurements versus analog control voltage . . . . .	82
Fig. 6.13:	Comparison curves using EFM, oscilloscope and Nortel measurements . . .	83
Fig. 6.14:	Nortel provided scattering parameters. . . . .	84
Fig. 6.15:	Nortel amplifier package . . . . .	85
Fig. 6.16:	Microphotograph of amplifier layout. . . . .	86
Fig. 6.17:	Input 50 Ohm transmission line feeding amplifier input pad . . . . .	87
Fig. 6.18:	Ground conductor models at high frequency. . . . .	89
Fig. 6.19:	Power and ground rails on die . . . . .	90
Fig. 6.20:	$V_{EE}$ rail along with first three measurement points. . . . .	91
Fig. 6.21:	Amplitude and phase distribution along $V_{EE}$ line . . . . .	92
Fig. 6.22:	Nortel amplifier output transmission line . . . . .	93
Fig. 6.23:	Nortel amplifier along with connecting transmission lines . . . . .	94
Fig. 6.24:	Cascaded distributed amplifiers and probe locations. . . . .	95
Fig. 7.1:	Invasiveness model . . . . .	98
Fig. 7.2:	Equivalent circuit model . . . . .	99

Fig. 7.3:	Loading capacitance simulation results.....	100
Fig. 7.4:	Different sources of loading capacitance.....	101
Fig. 7.5:	Coupling capacitance measurement setup.....	102
Fig. 7.6:	Coupling characteristic at position #1.....	103
Fig. 7.7:	Coupling characteristic at position #2.....	104
Fig. 7.8:	Coupling characteristic at position #3.....	105
Fig. 7.9:	Loading capacitance measurement using a CPW structure.....	106
Fig. 7.10:	Coupled line resonator.....	107
Fig. 8.1:	Capacitance gradient simulation overtop a 1 $\mu\text{m}$ wide conductor.....	109
Fig. 8.2:	Typical parasitic probing environment.....	110
Fig. 8.3:	Electrostatic interaction with the cantilever beam.....	111
Fig. 8.4:	Parasitic interaction with DC potential carrying conductors.....	112
Fig. 8.5:	CPW three conductor system.....	114
Fig. 8.6:	Amplitude and phase profile for ideal spatial resolution.....	115
Fig. 8.7:	GaAs CPW structure and cross-sectional view.....	115
Fig. 8.8:	Measured amplitude and phase profile versus probe position.....	116
Fig. 8.9:	Variable height measurement on the CPW structure.....	117
Fig. 8.10:	Amplitude null point versus probe to circuit spacing.....	118
Fig. 8.11:	Approximate functions for $F_k$ weights with probe to circuit spacing.....	120
Fig. 8.12:	Typical nulling trends with variable probe to circuit spacing.....	120
Fig. 8.13:	Nulling point gradient versus probe to circuit spacing.....	121
Fig. 9.1:	Bending of cables result in changes in electrical length.....	124
Fig. 9.2:	Equivalent circuit at 16 GHz.....	125

Fig. 9.3:	16 GHz measurement block diagram .....	126
Fig. 9.4:	I/Q modulator characterization setup.....	127
Fig. 9.5:	Measured I/Q modulator characterization at 16 GHz .....	128
Fig. 9.6:	Software compensated I/Q modulator characteristic at 16 GHz .....	129
Fig. 9.7:	16 GHz measurements on a CPW structure .....	130
Fig. 9.8:	EFM versus Network analyzer measurements at 16 GHz.....	131
Fig. 9.9:	Insertion loss measurement at 16 GHz .....	132
Fig. 9.10:	Output transmission line measurement at 16 GHz .....	133
Fig. 9.11:	Distributed amplifier with sample probing locations.....	134
Fig. 9.12:	Amplitude and phase measurement of a distributed amplifier .....	135
Fig. 10.1:	Frequency upconversion scheme .....	137
Fig. 10.2:	Upconversion of EFM modulated sampling signal .....	138
Fig. 10.3:	High frequency EFM hardware configuration. ....	139
Fig. 10.4:	Probe and circuit signals along with associated harmonics.....	140
Fig. 10.5:	Normalized deflection characteristic at different sideband rejections.....	141
Fig. 10.6:	Frequency upconversion hardware block diagram .....	143
Fig. 10.7:	Relcom mixer characterization at 1.95 GHz .. ..	144
Fig. 10.8:	Relcom mixer characteristic at 1.95 GHz .....	144
Fig. 10.9:	M1R0920 mixer characterization .....	145
Fig. 10.10:	Lower sideband rejection notch filter .....	146
Fig. 10.11:	Vector measurements of a CPW structure at 16 GHz .....	147
Fig. 10.12:	Mechanical deflection as a function of physical length .....	148
Fig. 10.13:	16 GHz calibration using frequency upconversion .....	150

## *List of Tables*

Table 4.1: EFM and contact probe measurements on TI LNA. . . . .	52
Table 4.2: EFM and simulation results for GaAs mesfet amplifier . . . . .	56
Table 6.1: Internal node measurements at 10 GHz. . . . .	95
Table 7.1: Capacitance measurements on a CPW structure . . . . .	107
Table 9.1: Network Analyzer measured attenuator characteristic at 16 GHz. . . . .	130
Table 9.2: $V_{EE}$ line measurements at 16 GHz . . . . .	136
Table 10.1: Simulated phase and amplitude errors under varying sideband rejection . .	142
Table 10.2: Filter insertion loss measurements. . . . .	147
Table 10.3: Attenuator phase measurements using EFM and network analyzer . . . . .	149

## ***List of Nomenclature***

**RFIC: Radio Frequency Integrated Circuit**

**PCB: Printed Circuit Board**

**MMIC: Monolithic Microwave Integrated Circuit**

**CPW: Coplanar Waveguide**

**DUT: Device Under Test**

**Passivation: Protective dielectric layer on top of integrated circuits**

**SNR: Signal to Noise Ratio**

**EFM: Electrostatic Force Microscopy**

**SPM: Scanning Probe Microscopy**

**LNA: Low Noise Amplifier**

## Chapter 1: Introduction

### 1.1 Internal Node Test

Presently in the field microelectronics, it is becoming increasingly important to have the capability to perform internal node test. This capability is required to determine the origin of failure in both digital and microwave integrated circuits. Presently in RFIC (Radio Frequency Integrated Circuits) technology it is critical to be able to perform amplitude and phase measurements at an internal node basis. This is becoming increasingly important as we strive for full system on chip (SOC) where multiple devices like amplifiers, filters and mixers are interacting with each other on the same die.



**Fig. 1.1:** *Internal node test*

A probing instrument must have both high spatial and temporal resolution, be non-invasive (small loading effect), have easy sample preparation and capability of arbitrary node probing without the need for predefined test points. This research will introduce a novel RFIC probing technique which satisfies the mentioned criteria.

## **1.2 Thesis Outline**

This research will commence with some discussion on existing probing techniques like contact probing, electro-optic, E-beam and photoconductive. The EFM (Electrostatic Force Microscopy) technique will be introduced along with a discussion of the key features of this kind of probing. Measurement results at 1 and 1.9 GHz on a variety of MMIC circuits will be presented and compared to simulation and known specifications.

The next chapter will discuss the implementation of the EFM instrument using I/Q modulation. This involves the development of the hardware and software to implement the I/Q modulation technique to achieve a completely automated amplitude and phase measurement system. The subsequent chapter will employ I/Q modulation to probe various circuits at 10 GHz. This will include a Nortel provided phase shifter, wideband amplifier and transmission line measurements including travelling and standing wave characterization.

The next few chapters will deal with the concept of spatial resolution and invasiveness in the context of EFM. These chapters will provide some simulation and measurement results to assess the invasiveness of the instrument. An attempt will also be made to understand and quantify the spatial resolution through experimentation. The next chapter will include vector voltage measurements at 16 GHz on a miniature 50 Ohm coplanar waveguide structure and distributed amplifier using I/Q modulation. The last chapter will discuss a frequency upconversion method for measuring higher frequency signals using existing lower frequency hardware. This method will be proven at 16 GHz through measurement of a 50 Ohm coplanar waveguide structure.

## ***Chapter 2: IC Probing Techniques***

### ***2.1 Introduction to IC Probing***

There are many different types of probing techniques which exist in the field of microelectronics. The most common type of probe is the basic contact probe. This includes low impedance probes designed for 50 Ohm measurements [1], medium impedance like resistive divider and high impedance probes. These probes require direct electrical contact between the measurement conductor and probe which is a disadvantage since they require unpassivated test points. These probes are often limited in both invasiveness, especially at high frequency and accessibility to internal nodes of the circuit. These problems introduce more exotic types of probing schemes which include Electron Beam [2], Electro-optic [3], Photoconductive [4] and, more recently Scanning Force Probing [5]. These new techniques are all based on repetitive sampling. This enables them to measure very high frequency internal node signals (GHz range) but cannot capture single events. In this chapter, all of the mentioned probing techniques will be summarized with a discussion on advantages and disadvantages. An assessment of each probing instrument will be done in terms of spatial resolution, bandwidth, invasiveness, and ease of implementation.

### ***2.2 Contact Probes***

The most common type of probe is the contact probe. These probes involve making direct contact with a measurement conductor using a small probing needle. The disadvantage of these probes is that they require unpassivated test points. Contact probing is often organized into the following categories: low impedance, medium impedance, and high impedance.

### 2.2.1 Low Impedance Probes

Low impedance probes typically have the highest bandwidth over any other type of probe. The unfortunate draw back is that these probes present a very large load to the circuit. This fact restricts their use to network ports of RFICs where low impedance loads and sources are expected. For most microwave applications, these probes are often impedance controlled at a system impedance of 50 Ohms. The basic structure of this probe is shown in Fig. 2.1.

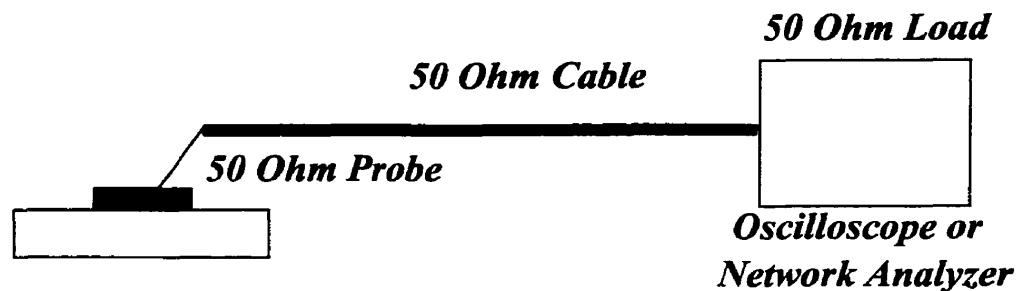


**Fig. 2.1:** 50 Ohm matched impedance probe

The probe makes contact with the measurement conductor and is connected to a 50 Ohm cable terminated in a matched load of a high frequency oscilloscope, network or spectrum analyzer. The 50 Ohm probe can be implemented using various techniques. The first utilizes a sharpened center conductor of a coaxial cable. The second uses a short probe needle which contacts the surface[6]. These probes are often limited by the inductance presented by the protruding center conductor (coaxial method) and the needle. Of course these methods will fail when the length of the protruding conductor approaches a significant fraction of a wavelength[6]. Another implementation uses a small 50 Ohm 3 finger CPW probe which makes contact with the circuit[7]. This allows for a 50 Ohm

impedance characteristic directly to the tip of the probe. Proper layout of the RFIC will provide a ground-signal-ground configuration to facilitate placement of the CPW probe.

These probes are very commonly used in on-wafer probe stations where RFICs can be characterized through network measurements. Using proper network analyzer calibration, scattering parameters can be measured with reference planes directly at the input and output pads. However, as mentioned before these probes present a 50 Ohm load which makes them too invasive for internal node test.

### 2.2.2 Medium Impedance Probes

Medium impedance probes typically exhibit smaller loading effects and have loading impedances in the  $K\Omega$ . The most popular example is the resistive divider probe. These probes are not as invasive as the matched impedance probe which makes them more suited for internal node probing. The resistive divider is quite easy to construct consisting of a larger series resistance connected to a transmission line terminated in its characteristic impedance as shown in Fig. 2.2. In this technique there is a tradeoff between loading and SNR(Signal to Noise Ratio).

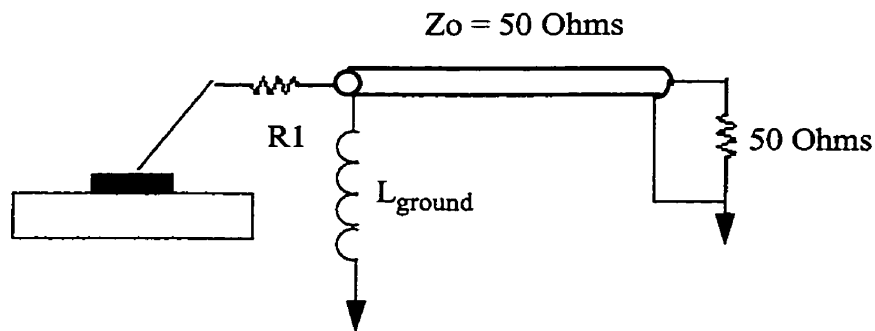


Fig. 2.2: Resistive divider probe

The bandwidth of this probe is typically limited by the inductance in the ground wire.

There is also a reduction in noise performance due to lossy elements in the probe.

### 2.2.3 High Impedance Probes

The last class of contact probe is the high impedance probe. This class of probe can be separated into two classes: active and passive. In a passive probe, the needle is connected through a large series resistor in parallel with a compensating capacitor which drives a high impedance transmission line into the high impedance load of a high impedance oscilloscope as shown in Fig. 2.3

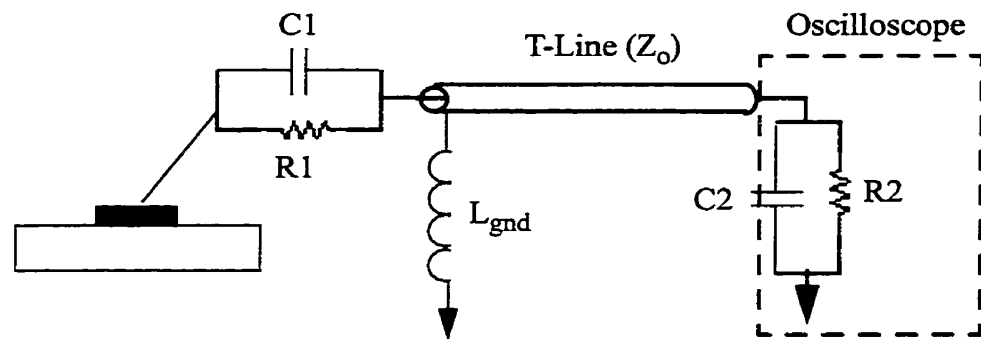


Fig. 2.3: Passive high impedance probe

The channel of a high impedance oscilloscope is typically modelled as a parallel resistor and capacitor. A typical 100 MHz Tektronics oscilloscope may have a resistance of 1 M $\Omega$  and an input capacitance of 20 pF. To decrease the loading effect, a series resistor ( $R_1$ ) is placed after the probe tip which is chosen by the divide ratio. A parallel capacitor ( $C_1$ ) is introduced to compensate for the RC time constant of the oscilloscope to achieve higher bandwidth. By choosing an appropriate compensating capacitance ( $C_1$ ), a flat frequency response can be achieved. Unfortunately this ideal frequency response is limited by when the length of the cable becomes a major fraction of a wavelength which can introduce resonances. The cable is usually too long to be of any use for measuring RF

signals in the GHz range. A typical bandwidth of this probe is 100-500 MHz. This probe is also quite invasive due to the large input capacitance which is usually in the picofarad range for most realtime oscilloscopes.

The problem of cable length can be rectified by introducing the active high impedance probe. This type of probe utilizes an active buffer to separate the loading effects of the cable and the oscilloscope with the circuit as shown in Fig. 2.4. Often in these probes, an input transistor is placed directly on the tip of the probe to create a less frequency sensitive high impedance plane at the probe tip. Commercial probe vendors like PicoProbe utilize this type of approach[7].

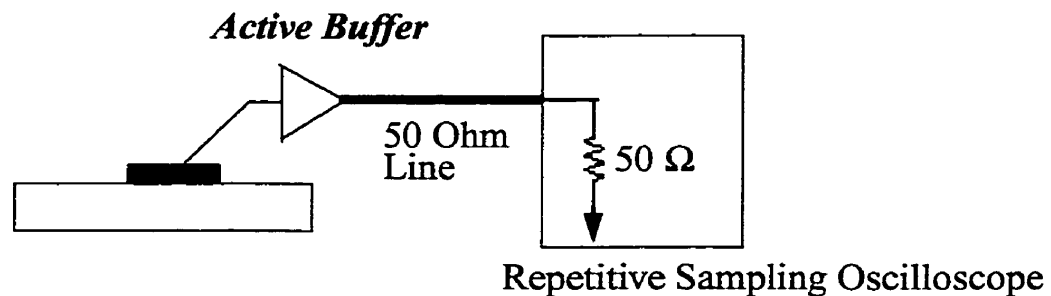


Fig. 2.4: Active high impedance probe

This type of probe is useful because it enables the use of high frequency oscilloscopes which typically have 50 Ohm input channels that are normally too invasive for internal node probing. The buffer presents a high impedance load to the circuit and drives the measured signal into a 50 Ohm load. The bandwidth of these probes are typically limited by the bandwidth of the buffer. The invasiveness is determined by the amount of gate capacitance of the FET and surrounding parasitics of the needle. A typical loading capacitance would be 100 fF and as small as 40 fF as in the case of the 1 GHz picoprobe[7],

which makes it suitable for high frequency internal node probing. Ground wire inductance has minimal effect since the capacitive reactance of the buffer is usually quite high. Commercial active probes have reported bandwidths up to 3 GHz[7]. These probes are useful for measuring most digital signals up to 1 Gbit/s, but for microwave applications this is not enough bandwidth, especially for millimeter wave measurements.

### 2.3 Repetitive Sampling Technique

As the frequency of the signal increases, the processing electronics in an oscilloscope are not fast enough to track the signal. These signals cannot be measured in real time due to the bandwidth restrictions of the electronics. This obstacle can be alleviated by using the repetitive sampling technique. This involves sampling some voltage signal using a train of narrow sampling pulses ( $\Delta(t)$ ). The synthesis of the pulse will vary on the type of probing instrument. There are two common methods of implementing this technique. The first includes sampling a signal with a low frequency modulated pulse train with the same fundamental frequency as the signal waveform and the second uses a sampling pulse train with a fundamental frequency slightly different than that of the signal waveform. The first technique is demonstrated in Fig. 2.5.

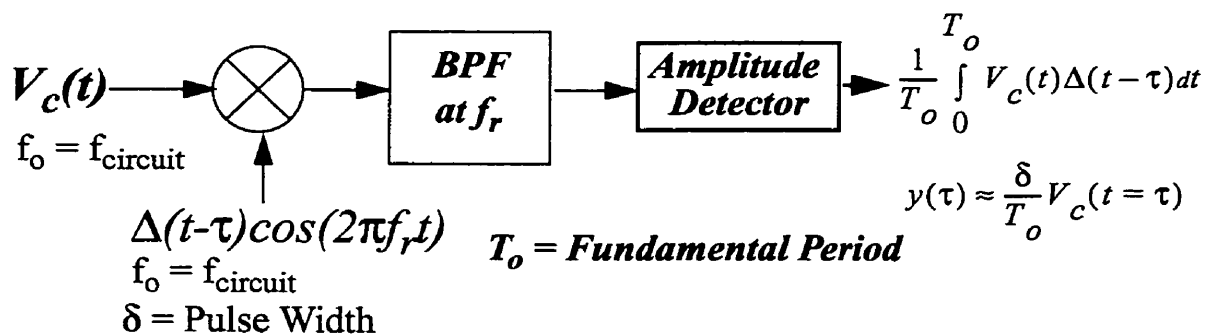


Fig. 2.5: Repetitive sampling technique #1

The sampled signal represents a downconverted version of the original circuit signal. Using a high Q bandpass filter at the low frequency ( $f_r$ ) and amplitude detector will produce a signal which is proportional to the circuit voltage at time  $\tau$ . The entire waveform can be reconstructed by shifting the pulse train over the entire period of the circuit waveform. This technique uses software techniques to shift the pulse train after each measurement point.

The second technique involves using a sampling pulse train which has a slightly smaller fundamental frequency as the circuit waveform. The implementation of this method is shown below in Fig. 2.6.

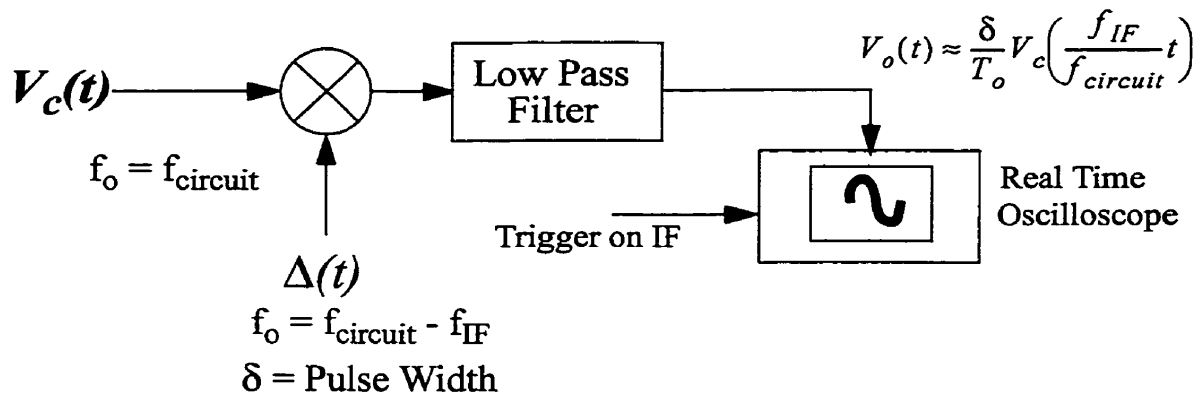


Fig. 2.6: Repetitive sampling technique #2

In this technique, all fourier coefficients of the circuit signal are downconverted down to the IF frequency. A low pass filtering operation will result in a signal which is essentially a time stretched version of the original signal with a fundamental frequency of  $f_{\text{IF}}$ . This low frequency signal can be measured easily using a real time oscilloscope triggering on the IF signal.

The most commonly used method is technique #2. In all repetitive sampling techniques the bandwidth is defined by the width of the pulse ( $\delta$ ). Repetitive sampling is the means to extend the bandwidth of most commercial oscilloscopes up to 50 GHz.

The next sections will discuss some probing schemes which employ this technique. Several examples are: photoconductive, electro-optic and electron beam probing.

## 2.4 Electro-Optic Probing

Electro-optic probing involves exploiting the birefringence properties of various materials to measure electric fields and infer information about the voltages under consideration. A birefringent material is one which exhibits changes in index of refraction as a function of electric field. There are two possible mechanisms: Pockel's effect which exploits the proportionality with electric field and the Kerr effect which is related by the square of the field. In the presence of an electric field, the index of refraction along one axis will change leaving the other the same. Imagine that the index of refraction along two perpendicular axis in a crystal is different. If we have a light wave polarized at  $45^\circ$ , the relative phase of the x and y components would change due to differing propagation velocities. This effect will result in a shift in polarization of the incident light as shown in Fig. 2.7.

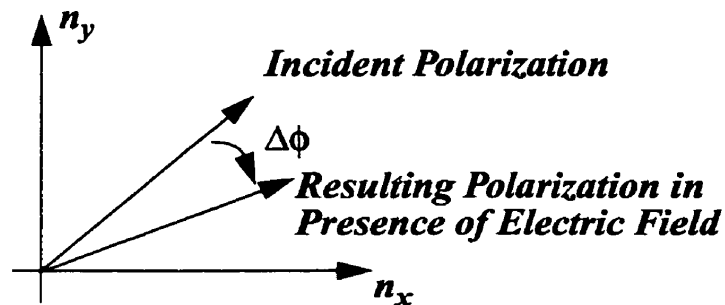
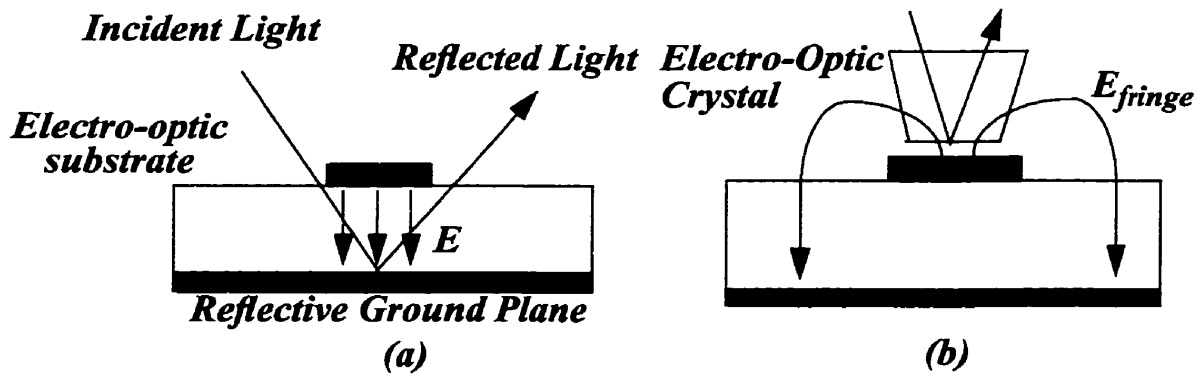


Fig. 2.7: Polarization shift in presence of electric field

For small fields, the polarization shift is approximately linear with Electric Field. This principle can be exploited using two different techniques. The first uses the electro-optic properties of the circuit substrate to probe fields under the conductor while the other utilizes a small electro-optic crystal which measures fringing fields above the target conductor[8].



**Fig. 2.8:** (a) Probing using electro-optic substrate (b) Probing using electro-optic crystal

The first technique is useful if the circuit under test has an electro-optic substrate like GaAs. Unfortunately for most integrated circuits, especially digital, silicon is the semiconductor of choice. Silicon by nature does not exhibit any electro-optic properties which means that option (b) of Fig. 2.8 must be employed. This involves using a small piece of electro-optic crystal which is moved in close proximity to the measurement conductor. This configuration will only measure the fringing field which is a disadvantage since most of the field is localized under the conductor as in a microstrip configuration. This technique operates better on differential and CPW transmission lines where there is ample field present above the conductor.

A typical electro-optic probing instrument is shown in Fig. 2.9[8].

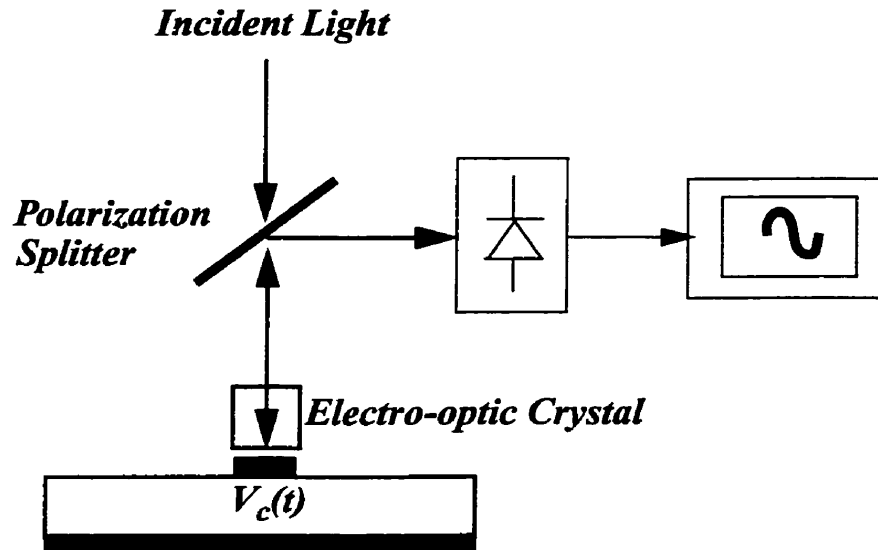


Fig. 2.9: Electro-optic probing instrument

In a real time system, the incident light would be a continuous beam with the photodetector output connected to a real time oscilloscope. In the repetitive sampling mode the incident light would be a periodic pulse train and the photodetector would be connected to a low pass filter and an oscilloscope or lockin amplifier.

The bandwidth of this instrument like any other kind of repetitive sampling technique is defined by the width of the optical pulse. Laser diodes with 10's of ps pulse widths are available on the market which provides bandwidth in the GHz range while more expensive die lasers can achieve pulse widths in the femtosecond range which provides Terahertz of bandwidth[8]. Spatial resolution is determined by both the size of the electro-optic crystal and the spot size of the laser beam. A spatial resolution of 2  $\mu\text{m}$  (spot size) has been reported[8]. Unfortunately this technique requires complex calibration to achieve absolute voltage measurement since field distributions are strongly dependent on conductor geometry.

## 2.5 Electron Beam Probing

Electron Beam probing operates on a very similar premise to the electro-optic but rather than using a small optical pulse, we use a small electron pulse. This technique operates on the principle that the electron energy is proportional to the voltage at that moment in time. If we bombard a conductor with electrons of known kinetic energy, it will eject secondary electrons from the metal only if the energy of the incident electrons exceeds the work function of the metal. The secondary electrons will have varying kinetic energies depending on the voltage levels at the ejection time. Monitoring the energy of the secondary electrons will allow for the determination of the desired voltage signal as indicated in Fig. 2.10[9].

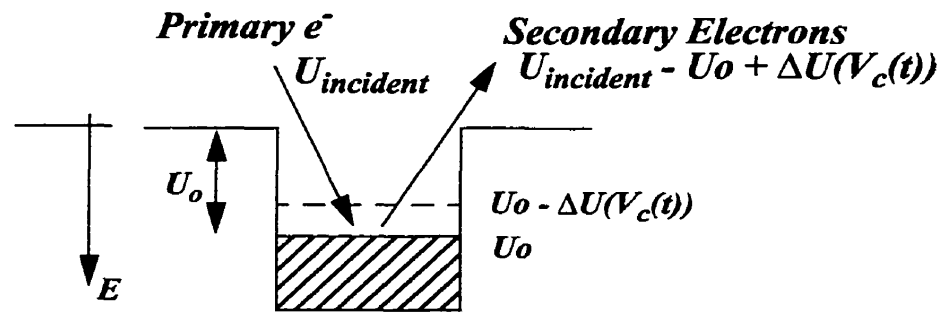


**Fig. 2.10:** Energy representation of electron emission

The incident electrons are typically accelerated to about 1 KeV[9]. Exceeding this energy can result in damage and charging effects on the measurement conductor. The E-Beam measurement scheme is shown in Fig. 2.11.

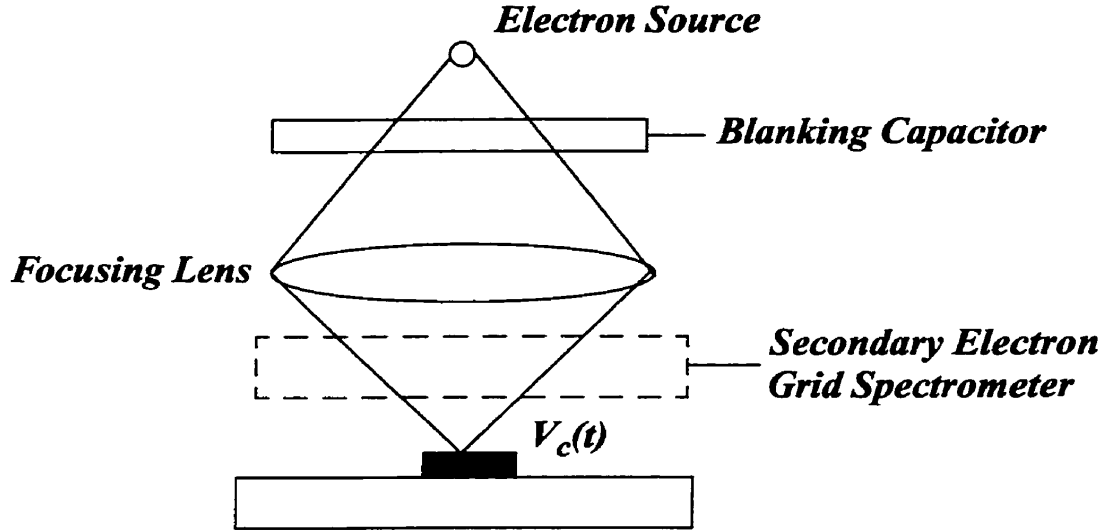


**Fig. 2.11:** *E-Beam implementation*

An electron beam is passed through a blanking capacitor which is used to provide the narrow electron pulses for the repetitive sampling technique. The pulsed beam is passed through a lens which focusses the beam onto the interconnect. The secondary electrons are collected using a grid potential spectrometer which measures their energy. This output signal varies linearly with the measured voltage on the interconnect line[10].

The bandwidth of the E-beam instrument like all other repetitive sampling techniques is defined by the width of the electron pulse. This depends highly on the speed of the blanking capacitor. An E-beam has a typical bandwidth of about 2-3 GHz[11]. Spatial resolution is defined by the spot size of the electron beam. Spot sizes for an incident energy of 1 KeV have been reported to be around 1  $\mu\text{m}$ [11]. Resolution can be improved by increasing the energy which can be described using the DeBroglie wavelength relation

$$\lambda = \frac{h}{\sqrt{2mE}} \quad (2.1)$$

Typically the electron energy does not exceed 1 KeV to ensure the interconnect does not become damaged. E-Beam is a very expensive probing solution which requires the use of a vacuum, large voltages and complex calibration.

## 2.6 Photoconductive Sampling

Another popular high frequency probing technique involves photoconductive sampling. This technique employs small semiconductor switches that can be turned on and off very rapidly. The switch can be controlled using a pulsed laser source. A typical photoconductive switch structure would be  $30 \times 30 \mu\text{m}$  interdigital gate fabricated on a low temperature grown GaAs[12]. The optical excitation will change the semi-conductor resistance from a few 10's of Ohms to several 100's of MOhms[12]. This switch can be integrated onto a contact probe to implement direct repetitive sampling as shown in Fig. 2.12.

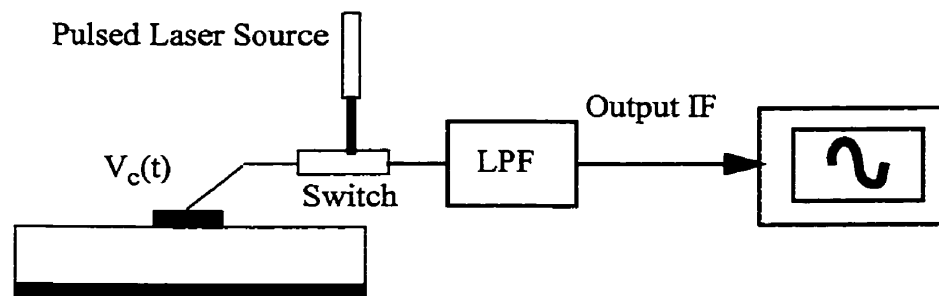


**Fig. 2.12:** Photoconductive sampling contact probe

The photoconductive probe uses a pulse train of optical pulses to gate the photoconductive switch which produces a down-converted IF signal that is recovered using a low pass filter. The resulting IF signal can be viewed using an oscilloscope, spectrum analyzer or lockin-amplifier.

Similar to all repetitive sampling techniques, the bandwidth is defined by the length of time the switch remains on. A 3.5 ps time response has been reported which provides a bandwidth over 100 GHz[13]. A typical photoconductive probe has a 7  $\mu\text{m}$  wide tip which provides less than 10  $\mu\text{m}$  of spatial resolution[12]. Invasiveness of the instrument is quite low since the “off” resistance of the switch is around 100 MOhms. Unfortunately, the capacitance associated with the switch and the probe tip could feasibly be around 100 fF making it quite invasive for millimeter wave measurements. Similar to contact probes, this technique requires unpassivated test points which is a definite disadvantage.

## ***Chapter 3: Scanning Force Probing***

### ***3.1 Scanning Probe Microscopy***

Scanning Probe Microscopy is becoming a popular area of research with diverse applications. A SPM (scanning probe microscopy) instrument makes use of a small micromachined cantilever designed to vibrate. The measurement process involves measuring the deflection of these small probes. The probe can be raster scanned along the surface of a material to infer topographical information such as in AFM (Atomic Force Microscopy). A SPM probe can have a typical radius of curvature of 20 nm which makes it ideal for resolving features in the nanometer range [14]. There are other applications which use the probe in a non-contact fashion like in scanning force probing. Several examples are MFM (Magnetic Force Microscopy) and EFM (Electrostatic Force microscopy). These techniques measure the force by observing the mechanical vibration of the cantilever.

### ***3.2 Micromachined Cantilevers***

Scanning force probing techniques make use of small micromachined cantilever probes. These probes are typically very small mechanical structures resembling a diving board or pyramid that are designed to vibrate. These probes can have lengths of 350  $\mu\text{m}$  with a 20 nm radius tip. These structures are commonly built using either silicon or silicon nitride. In EFM, we use cantilevers which are coated in tungsten for conductivity. It is necessary to have conductive probes since voltages must be applied to the probe tip while in AFM it is not necessary. A SEM image of a typical silicon cantilever is shown in Fig. 3.1. In this structure the beam length is approximately 350  $\mu\text{m}$  with a conical tip length of 10  $\mu\text{m}$ .

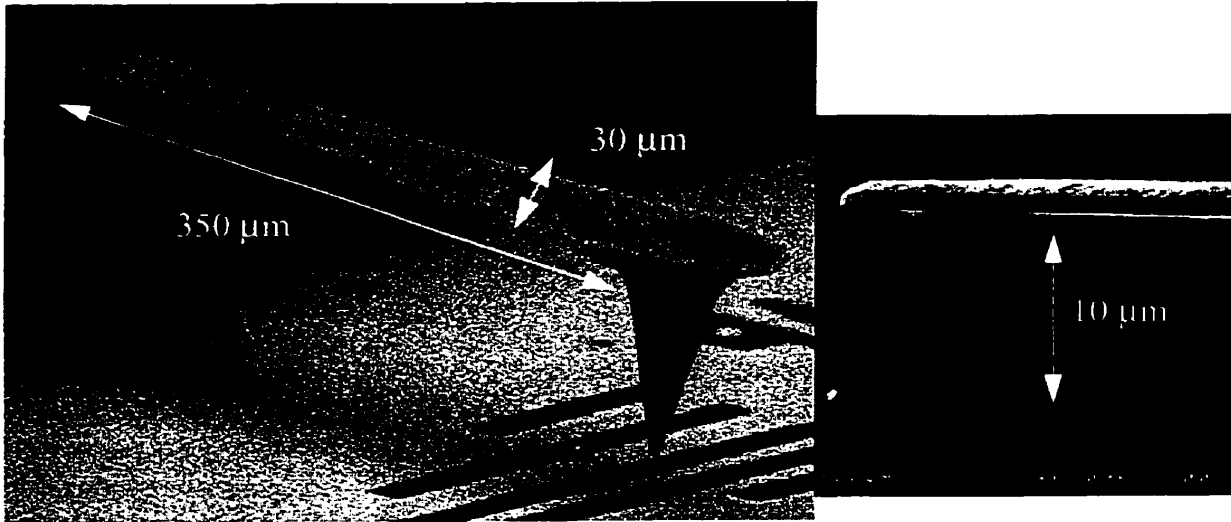


**Fig. 3.1:** Silicon cantilever with conical tip[15]

### 3.3 Mechanical Frequency Response

These mechanical structures behave very similar to that of a mass on a spring. Cantilever data sheets often specify spring constant and resonant frequency as typical parameters. The resonant frequency and spring constant can be calculated from equations 3.1 and 3.2 where  $E$  represents the modulus of elasticity,  $I$  is the moment of inertia,  $l$  being the length of the beam and  $m$  is the mass of the cantilever beam. The resonant frequency formula is similar to that of a point mass on a spring, but it also accounts for the non-zero mass of the cantilever beam[16].

$$k = \frac{3EI}{l^3} \quad (3.1)$$

$$\omega_o = \sqrt{\frac{k}{0.235m + m_{tip}}} \quad (3.2)$$

For the micromachined silicon cantilevers used in this research, typical numbers for spring constant and resonant frequency are 0.05 N/m and 13 KHz. Small spring constant cantilevers are always desirable for EFM since they provide more deflection per unit force and hence more signal.

In scanning force applications, the mechanical frequency response becomes a very important issue. When a time varying force is applied to the beam, it is necessary to determine the time varying deflection characteristic. Since the equation of motion is linear, we can treat this mechanical system as being linear time-invariant. The resonant behavior of the probe suggests the use of an underdamped second order system model where  $F(t)$  is the force,  $z(t)$  is the resulting deflection and  $H(s)$  is the transfer function as shown in Fig. 3.2.

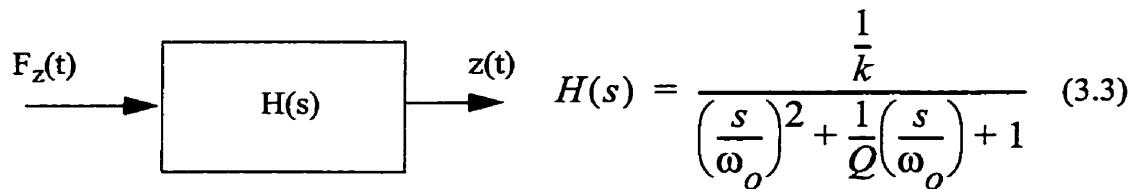


**Fig. 3.2:** Mechanical system transfer function

The resonant peak depends on the mechanical Q-factor of the probe. In a standard probing environment the Q may vary from 10-30 while in a vacuum the Q can approach several thousands. The frequency response can be easily measured by observing the mechanical noise spectrum on a spectrum analyzer. This involves connecting the deflection sensor output to a low frequency spectrum analyzer. This is assuming that the input noise force has a flat spectrum within the mechanical bandwidth of the probe. Fig. 3.3 demonstrates the noise spectrum around the resonant frequency of 12.3 KHz for the NT-MDT CSCS12/W2C silicon cantilever used in this research ( $l=350 \mu\text{m}$ ,  $w=35 \mu\text{m}$  and  $t=1.2 \mu\text{m}$ )[15]. The measured Q is approximately 30 in this situation.

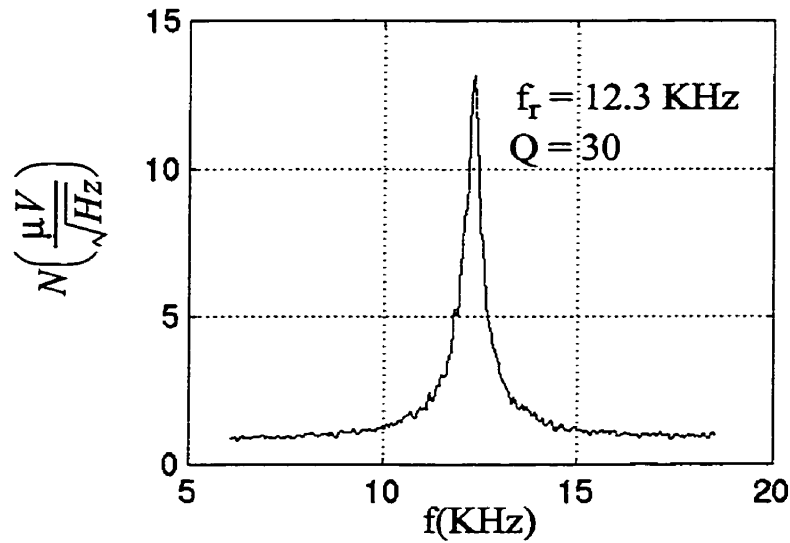


**Fig. 3.3:** *Measured mechanical noise spectrum*

Considering the mechanical frequency response of the probe, we are limited to a bandwidth of approximately 13 KHz. This makes it possible to measure low frequency signals ( $f < 13$  KHz) but it is not useful for high frequency signals. Later on in this research we will see techniques that allow for measurement of high frequency signals.

### **3.4 Deflection Sensors**

The second fundamental element of any scanning force probe is the deflection sensor. This sensor must have enough sensitivity to measure nanometer size deflections to be of any use in scanning force probes. The most common sensor types are: Fiber interferometer, scanning tunnelling microscope and laser beam bounce technique.

#### **3.4.1 Fiber Interferometer Technique**

This technique utilizes a fiber optic cable which is held in close proximity to the beam. As the cantilever bends, a combination of destructive and constructive interference occurs between the reflected beams at the air-dielectric and the air-cantilever interface that pro-

vides a signal approximately proportional to deflection on a small signal scale[14]. The fiber inferometer setup is shown in Fig. 3.4.

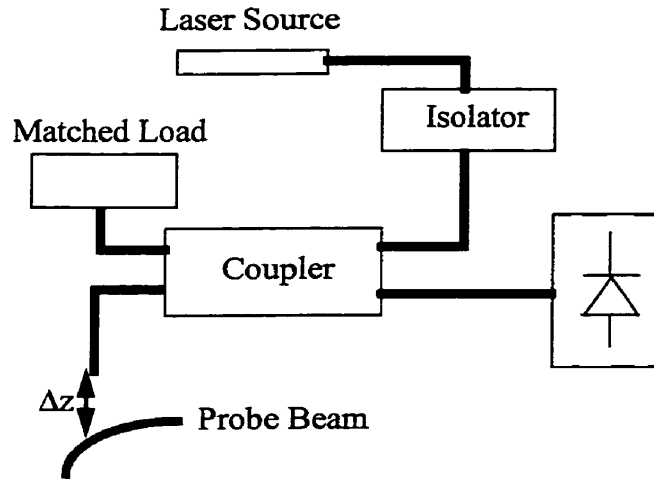


Fig. 3.4: Fiber inferometer deflection sensor

The ratio of reflected and incident power is shown in Fig. 3.5 and by eqn. 3.4. The reflectivity at each interface is given as  $r_1$  and  $r_2$ .

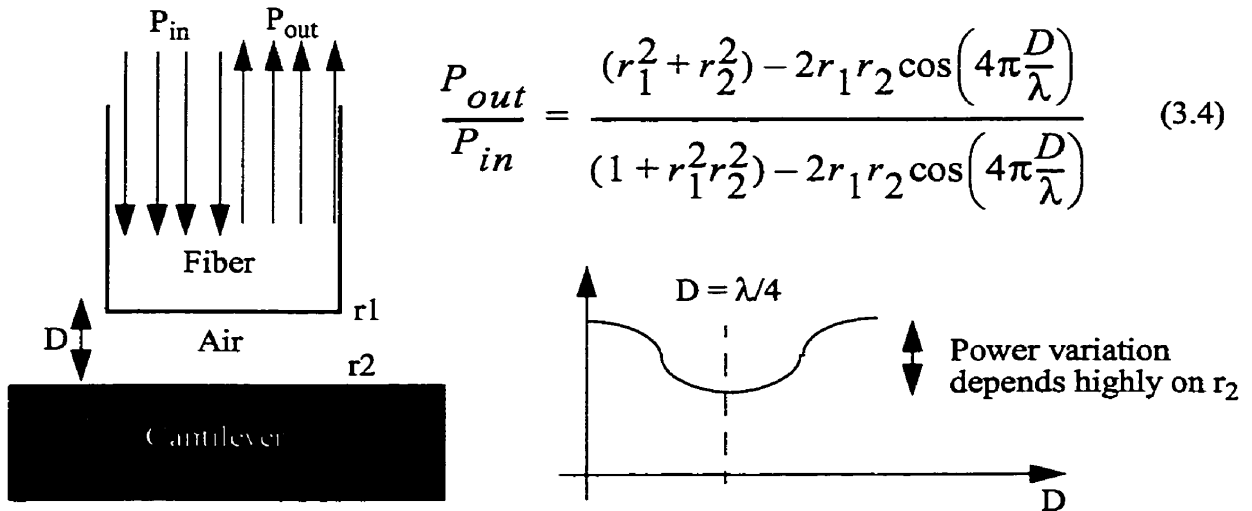


Fig. 3.5: Reflection characteristic as a function of probe deflection

The air interface acts as an impedance transformer that oscillates between maxima and minimum every quarter wavelength similar to a piece of transmission line. Unfortunately in EFM applications the cantilever must be coated with a conductive material that has high reflectivity ( $r_2 = 1$ ) which drastically reduces the sensitivity of this sensor.

### ***3.4.2 Tunnelling Electron Sensor***

In the past, tunnelling electron sensors were utilized to measure mechanical deflections[14]. This was done by placing a small wire in very close proximity to the cantilever. A dc bias voltage is applied which causes electrons to tunnel through the air. The tunnelling current follows an exponential variation with distance making this method very sensitive to angstrom sized displacements. This technique is not very practical since the wire must be several 10's of angstroms away from the cantilever beam which runs the risk of making contact since we expect nanometer scale deflections in EFM.

### ***3.4.3 Laser Beam Bounce Method***

The laser beam bounce method is probably the most commonly used deflection sensor in any scanning force application. It is not as sensitive compared to the fiber interferometer but it is both the simplest and least expensive solution. The beam bounce method is shown in Fig. 3.6[17].

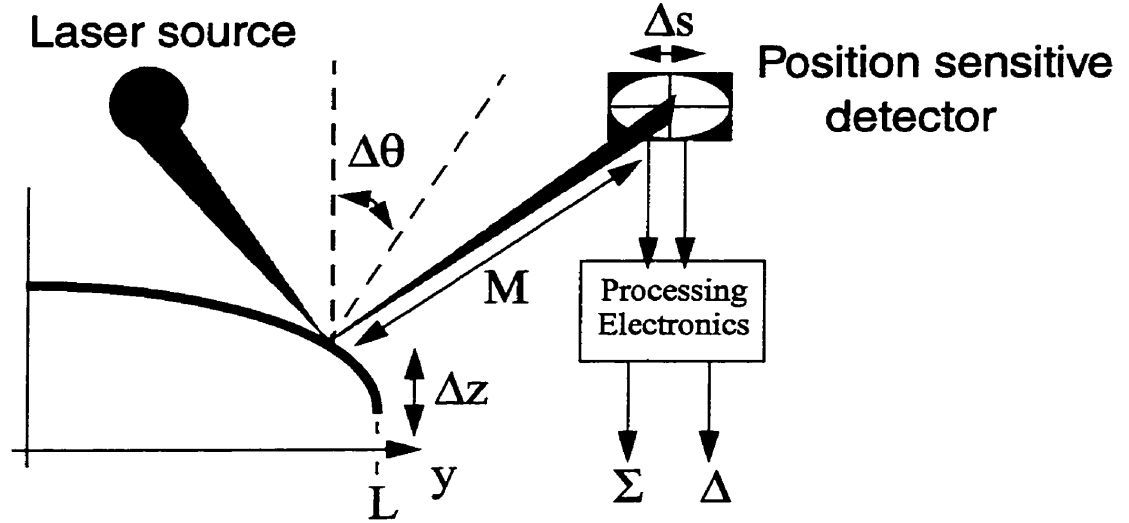


Fig. 3.6: Laser beam bounce method

This technique involves focusing a laser onto the beam of the cantilever where the reflected beam is collected by a split photodetector. The photodetector has two outputs representing either half, which run through processing electronics that generates a sum,  $\Sigma$  and difference signal,  $\Delta$ . As the probe cantilever moves, the angle of the reflected beam changes resulting in a difference signal approximately proportional to displacement for small deflections[14].

For a force applied at the tip of the probe( $y=L$ ), the deflection characteristic of the cantilever beam is given by

$$z = \frac{F}{6EI}y^2(3L - y) \quad (3.5)$$

The difference signal from the deflection sensor measures the deviation angle with the normal of the beam. For small deflections we can approximate the angle using

$$\Delta\theta \approx \left. \frac{dz}{dy} \right|_{y=L} = \frac{FL^2}{2EI} \quad (3.6)$$

Substituting the spring constant formula (eqn. 3.1) into the above equation provides us with an expression in terms of deflection

$$\Delta\theta \approx \frac{3\Delta z}{2L} \quad (3.7)$$

The movement of the laser beam at the photodetector can be approximated as

$$\Delta s \approx 3 \frac{M}{L} \Delta z \quad (3.8)$$

If we model the laser as a gaussian beam we can estimate the difference photocurrent by the following integral equation

$$I_d = 2Nq \int_0^{\Delta s} \frac{e^{-x^2/2\sigma^2}}{\sigma\sqrt{2\pi}} dx \quad \begin{array}{l} N = \text{photon density rate (photons/ms)} \\ q = \text{charge of electron} \\ \sigma = \text{spread of the beam} \end{array} \quad (3.9)$$

In most applications  $\Delta s \ll \sigma$ , therefore the above integral can be approximated as

$$I_d \approx 2Nq \left( \frac{\Delta s}{\sigma\sqrt{2}} \right) \frac{2}{\sqrt{\pi}} \quad (3.10)$$

Substituting eqn. 3.8 into 3.10 yields a relationship between the difference current and the deflection of the cantilever probe

$$I_d \approx \frac{6\sqrt{2}NqM}{\sigma L\sqrt{\pi}} \Delta z \quad (3.11)$$

This formula suggests that by increasing the optical path length (M), the sensitivity can be enhanced. This is not completely true since the beam spot size ( $\sigma$ ) will also increase with an increase in optical path length due to diffraction effects.

### 3.5 Electrostatic Force Microscopy (EFM)

Presently scanning force probing techniques are becoming very popular in the IC measurement arena, particularly EFM[18,19,20]. Electrostatic Force Microscopy is based on the electrostatic interaction between a small micromachined probe and a measurement conductor as shown in Fig. 3.7[16].

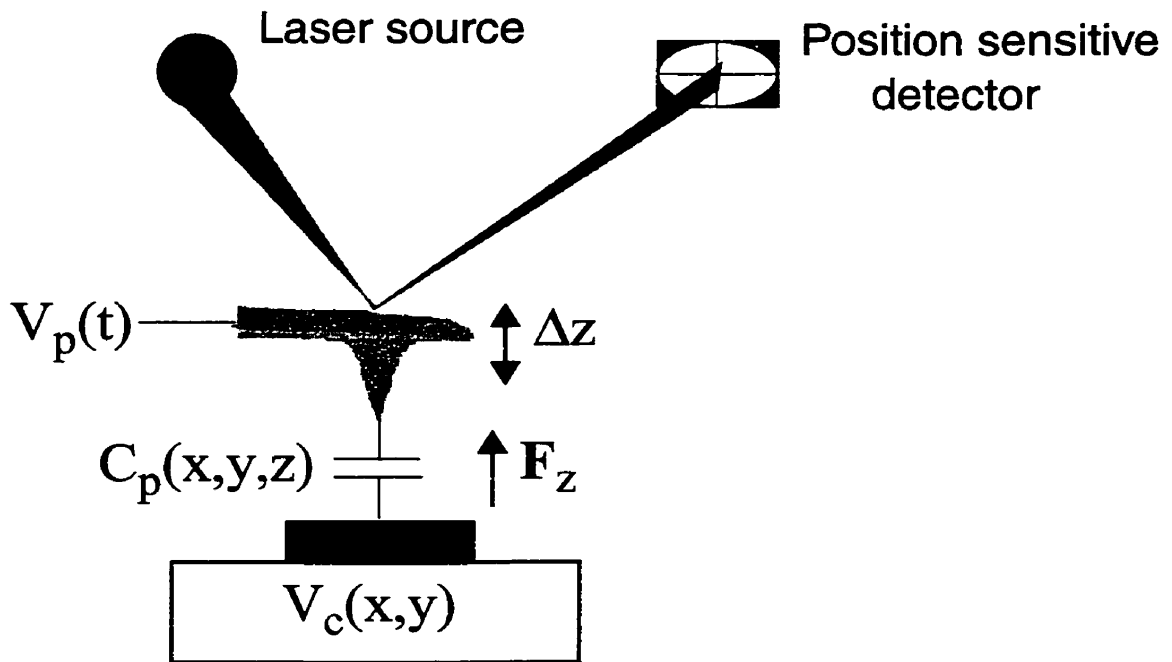


Fig. 3.7: Electrostatic interaction between probe and measurement conductor

If a voltage is placed on both the probe and the circuit, a small localized capacitor is formed and charges up. This brings rise to a coulomb force expressed by the non-linear force equation[21]

$$F_z = \frac{1}{2} \frac{\partial}{\partial z} C_p (V_p - V_c)^2 \quad (3.12)$$

A static force will cause the probe beam to deflect given by  $F_z/k$  where  $k$  represents the spring constant of the probe[22,23]. Time varying forces will cause time varying deflections according to the mechanical transfer function in eqn. 3.3. In this research, the deflection is measured using a laser beam bounce deflection sensor.

### **3.6 Internal Node DC Voltage Measurements**

The Electrostatic Force measurement technique can be employed to measure dc voltages levels inside integrated circuits[24]. Since this technique is non-contact, passivated power interconnect can be probed. The electrostatic formula can be used directly where a dc voltage is applied onto the probe until it nulls out the deflection. This technique will work in theory but noise performance is poor because the measurement is being made at DC. A modulation technique is typically employed to allow for measurement in regions of lower noise and allows for the use of a lockin amplifier to improve the overall SNR. Consider the case where a dc voltage  $\phi_{dc}$  is placed on a measurement conductor and a modulated voltage,  $A + K\cos(\omega_t t)$ , where  $\omega_t$  is a frequency within the mechanical bandwidth of the probe, is placed onto the probe as shown in Fig. 3.8.

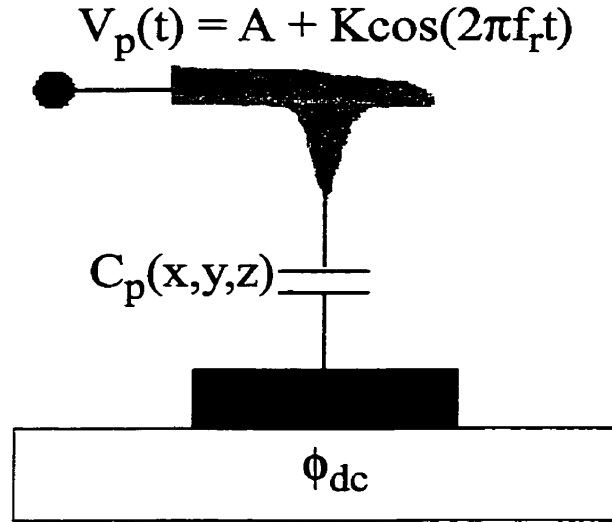


**Fig. 3.8:** Non-contact DC voltage measurement

Placing these voltages into the coulomb force equation will yield

$$F_z = \frac{1}{2} \frac{\partial C}{\partial z} (V_p(t) - \phi_{dc})^2 = \frac{1}{2} \frac{\partial C}{\partial z} (A + K \cos(2\pi f_r t) - \phi_{dc})^2 \quad (3.13)$$

Expanding the expression results in

$$F_z = \frac{1}{2} \frac{\partial C}{\partial z} (A^2 + 2AK \cos(2\pi f_r t) - 2A\phi_{dc} + K^2 (\cos(2\pi f_r t))^2 - 2K\phi_{dc} \cos(2\pi f_r t) + \phi_{dc}^2) \quad (3.14)$$

This produces force harmonics at dc,  $f_r$  and  $2f_r$ . If we concentrate on the  $f_r$  term, we have

the force expression

$$F_z|_{f_r} = \frac{\partial C}{\partial z} K (A - \phi_{dc}) \cos(2\pi f_r t) \quad (3.15)$$

If we choose  $f_r$  to be the resonant frequency of the probe we can compute the corresponding deflection harmonic according to the mechanical transfer function seen earlier in this research.

$$\Delta z|_{f_r} = \frac{Q}{k} K \frac{\partial C}{\partial z}^P (A - \phi_{dc}) \sin(2\pi f_r t) \quad (3.16)$$

By varying the A parameter, the deflection can be nulled which provides the corresponding dc voltage ( $A = \phi_{dc}$ ). This nulling technique is useful since it eliminates any dependence on the mechanical parameters like Q, k and more importantly  $dC/dz$  which is conductor geometry dependent. A block diagram of the instrument is shown in Fig. 3.9.

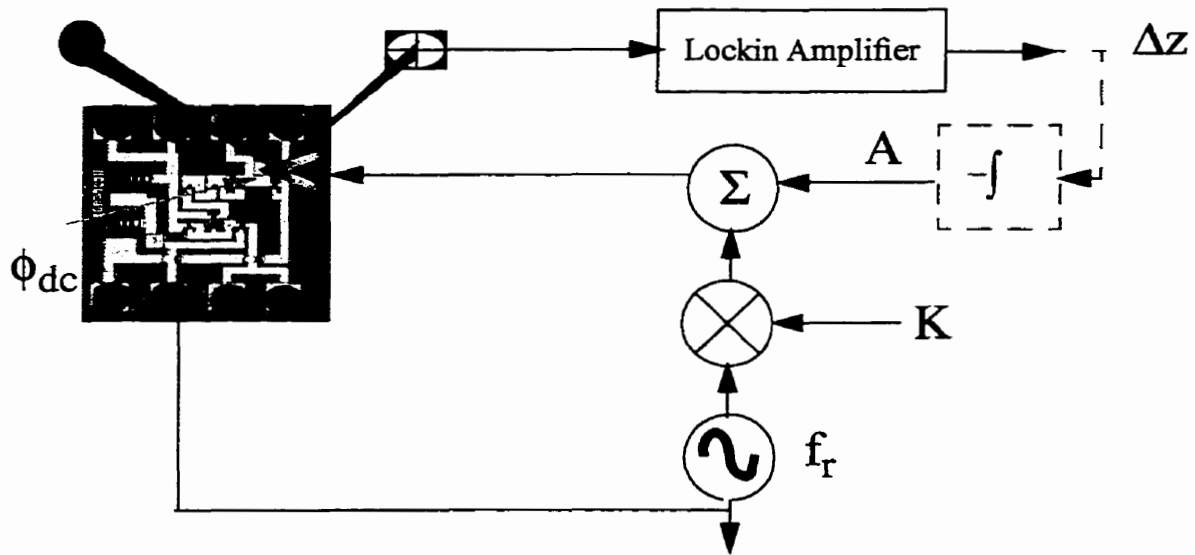
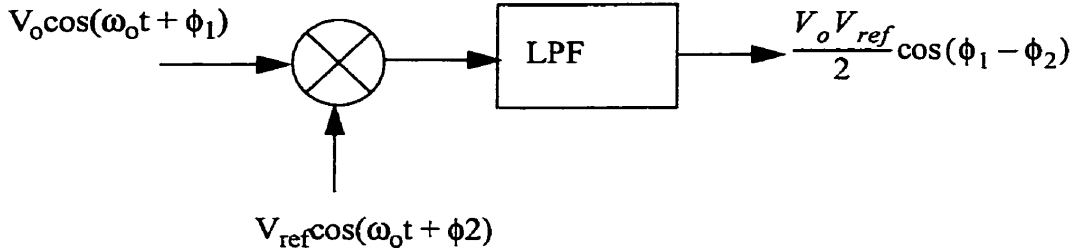


Fig. 3.9: Non-contact DC measurement scheme

The nulling process can typically be implemented using a negative feedback control system consisting of a low pass filter and integrator with the deflection signal being used as an error signal to modify the modulation parameter A. The output of the deflection sensor electronics is typically processed using a lockin amplifier. This type of amplifier uses a reference signal at  $f_r$  and down-converts the incoming signal down to baseband. The

baseband signal is then processed through a bandwidth adjustable low pass filter. A block diagram of the amplifier is demonstrated in Fig. 3.10[25].



**Fig. 3.10:** Lockin amplifier block diagram

This type of receiver essentially measures the amplitude of the input signal but done coherently which improves overall noise performance as compared to a simple envelope detector.

### 3.7 High Frequency Internal Node Probing

For probing high frequency signals (GHz) we cannot use the force equation directly. As shown before we are heavily bandlimited, in the range of 10-100 KHz, which makes it impossible to directly measure high frequency signals. To overcome this obstacle we can exploit the non-linearity in the force equation to implement a repetitive sampling technique very similar to that described in chapter 2[5,26,27]. In this work we use the repetitive sampling technique #1 discussed in chapter 2. Through the use of modulation we can perform the measurement at a maximum SNR location which would be at the mechanical resonant frequency of the probe. For all high frequency measurements the cantilever probe is mounted on a 50 Ohm transmission line to ensure that signal integrity is not compro-

mised. Consider the most general high frequency measurement scheme demonstrated in Fig. 3.11.

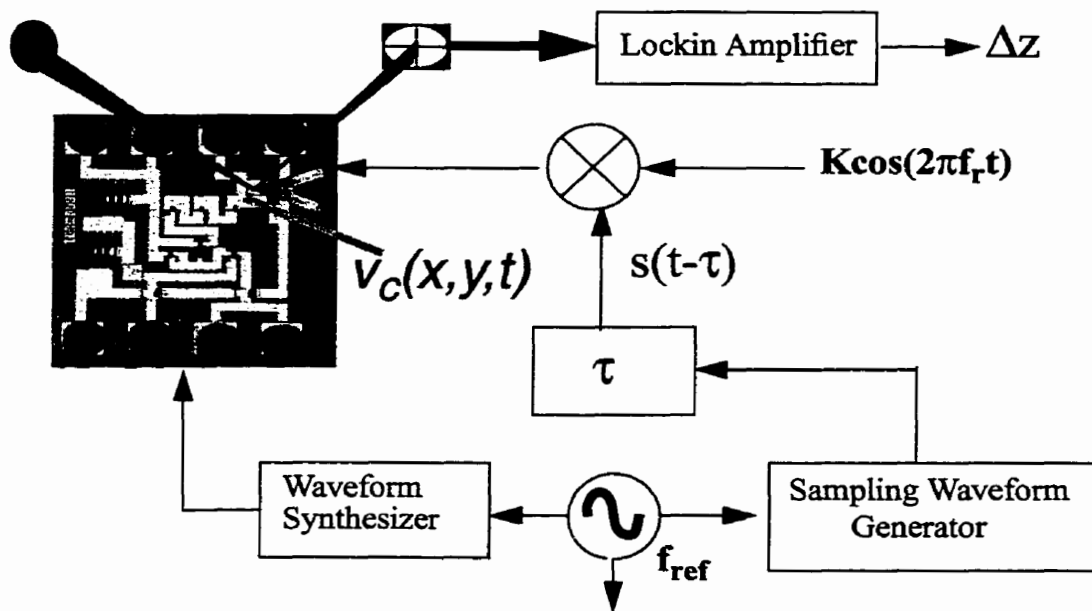


**Fig. 3.11:** *Generic high frequency EFM measurement scheme*

In this setup we use a synchronizing source to provide an excitation waveform with fundamental period  $T_0$  to drive the circuit. Using the same source, we synthesize a sampling waveform which possesses the same fundamental period as the excitation waveform. This waveform can be time shifted in respect to the measurement signal. The sampling waveform is then modulated at a low frequency within the mechanical bandwidth of the probe, namely the mechanical resonant frequency. The probe and circuit interaction occurs between the modulated sampling signal and the circuit voltage as shown in Fig. 3.12.

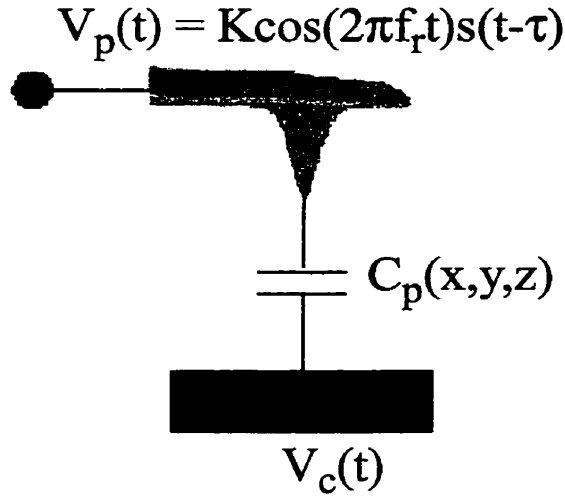


**Fig. 3.12:** High frequency circuit and probe signals

Using the force equation, the measured deflection is given as

$$F_z = \frac{1}{2} \frac{\partial C}{\partial z}^p (V_p(t) - V_c(t))^2 = \frac{1}{2} \frac{\partial C}{\partial z}^p (K \cos(2\pi f_r t) s(t-\tau) - V_c(t))^2 \quad (3.17)$$

Expanding the force equation will yield:

$$F_z = \frac{1}{2} \frac{\partial C}{\partial z}^p (K^2 (\cos(2\pi f_r t))^2 s^2(t-\tau) - 2K \cos(2\pi f_r t) s(t-\tau) V_c(t) + (V_c(t))^2) \quad (3.18)$$

This provides a force term at the  $f_r$  frequency which has one component given by

$$F_z|_{f_r} = -K \frac{\partial C}{\partial z}^p \cos(2\pi f_r t) \frac{1}{T_o} \int_{T_o} s(t-\tau) V_c(t) dt \quad (3.19)$$

The measured deflection from the lockin amplifier is given by

$$\Delta z|_{f_r} = -\frac{Q}{k} K \frac{\partial C}{\partial z}^p \frac{1}{T_o} \left( \int_{T_o} s(t-\tau) V_c(t) dt \right) \sin(2\pi f_r t) \quad (3.20)$$

This expression is similar to the one presented earlier in the section pertaining to repetitive sampling. The shifting of the sampling waveform,  $s(t)$ , through its fundamental

period  $T_o$ , we can reconstruct a transformed version of the input signal. The sampling signal can vary depending on the nature of the circuit voltage  $V_c(t)$ . In this chapter, two different sampling methods will be discussed. The first includes using a narrow sampling pulse to measure wideband signals while the other uses a sinusoidal sampling waveform to measure high frequency single tone signals.

### 3.8 Pulse Sampling Technique

This technique employs a sampling signal  $s(t)$  which attempts to emulate an impulse function. This method is targeted towards measuring wideband signals like digital waveforms. Example waveforms are shown in Fig. 3.13.

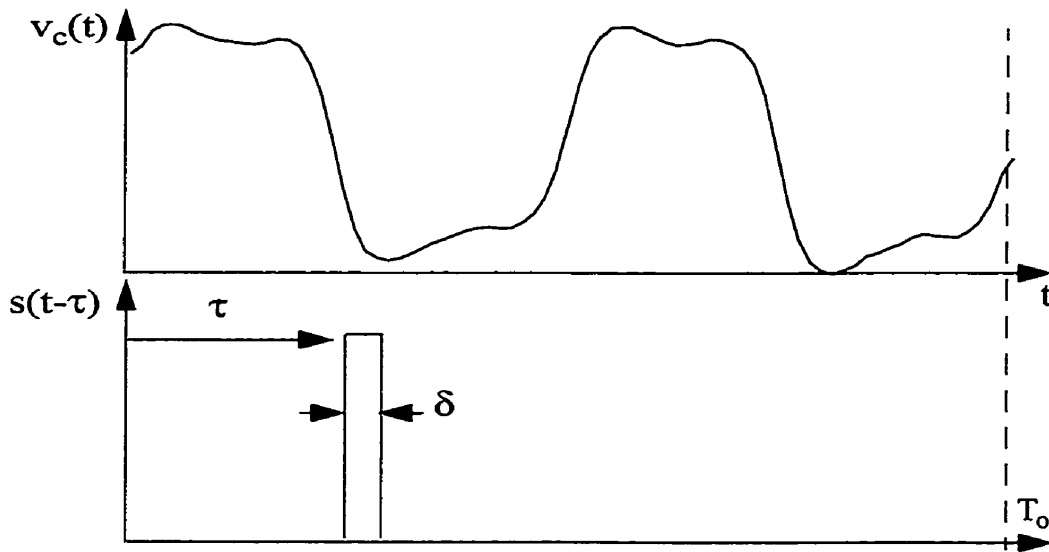


Fig. 3.13: Pulse sampling waveforms

Using eqn. 3.20 from the last section, we can approximate the measured deflection as

$$\Delta z|_{fr} \approx -\frac{Q}{k} K \frac{\partial C}{\partial z} \frac{\delta}{T_o} V_c(t=\tau) \sin(2\pi f_r t) \quad (3.21)$$

In this technique, as with any other repetitive sampling technique, the SNR depends on the pulse width and repetition rate. The smaller the pulse, the smaller the SNR of the instrument. The measurement bandwidth is defined by the width of the sampling pulse which is given by the Gaussian pulse approximation

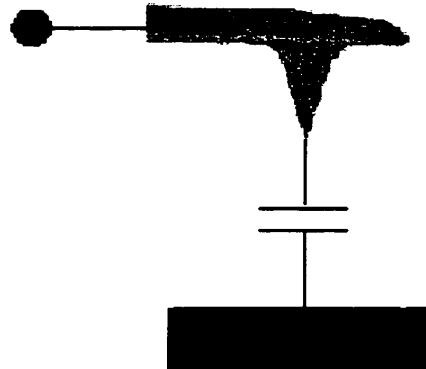
$$BW = \frac{0.45}{\delta} \quad (3.22)$$

The challenge with this technique is to synthesize a very narrow pulse which is often quite difficult to achieve. Reported bandwidths greater than 10 GHz have been achieved using EFM[21] and we have achieved greater than 10 GHz in this work.

### ***3.9 Sinusoidal Sampling Technique***

In microwave circuits, the ability to characterize amplitude and phase of single tone signals is very important. In these circuits, the internal node signals are all sinusoidal in nature which makes a sinusoidal sampling waveform more suited because it is much easier to synthesize than a pulse at high frequencies, especially above 10 GHz. In this method, a similar nulling technique can be employed as seen with the dc voltage measurement in section 3.6. Fig. 3.14 demonstrates the nature of the probe and circuit signals used in this technique.

$$V_p(t) = (A + K \cos(2\pi f_r t)) \cos(2\pi f_{RF} t + \phi_p)$$



$$V_c(t) = V_c \cos(2\pi f_{RF} t + \phi_c)$$

**Fig. 3.14:** Sinusoidal sampling technique

In this method, we need to determine the unknown amplitude ( $V_c$ ) and phase ( $\phi_c$ ) of the corresponding vector voltage. A block diagram of this method is shown in Fig. 3.15.

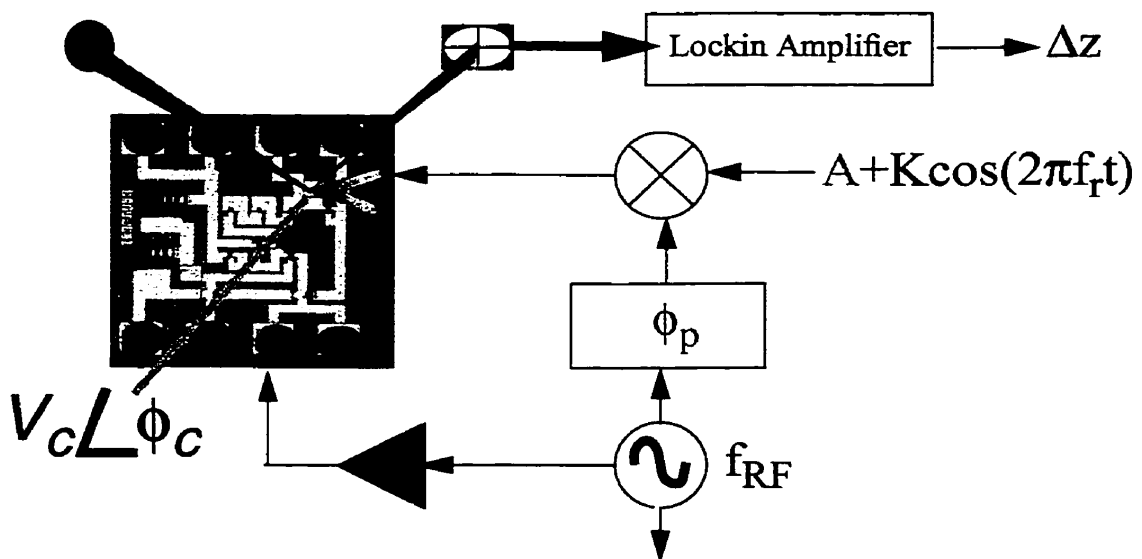


**Fig. 3.15:** Sinusoidal sampling block diagram

Performing similar mathematics we can solve for the deflection equation

$$\Delta z|_{fr} = \frac{1}{2} \frac{Q}{k} K \frac{\partial C}{\partial z} P (A - V_c \cos(\phi_p - \phi_c)) \sin(2\pi f_r t) \quad (3.23)$$

The measurement of  $V_c$  and  $\phi_c$  can be obtained by varying the  $A$  and  $\phi_p$  parameters[5]. This technique is known as the Heterodyne Nulling Technique which will be the focus of the next section.

### 3.10 Heterodyne Nulling Technique

The Heterodyne Nulling Technique is employed to solve for the unknown amplitude and phase of the measurement voltage[5,26]. The deflection characteristic as a function of  $A$  and  $\phi_p$  have been measured experimentally at 1 GHz as shown in Fig. 3.16.

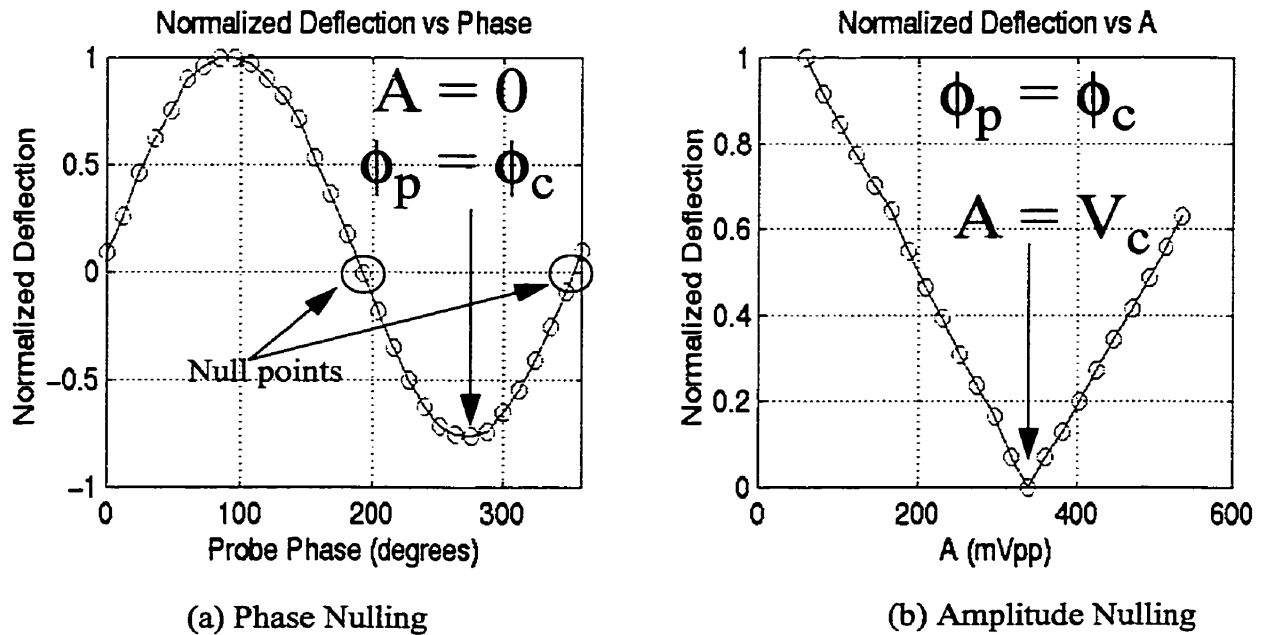


**Fig. 3.16:** *Heterodyne Nulling Technique*

Initially  $A$  is set to zero and the probe phase ( $\phi_p$ ) is varied to find the two zero crossings (null points) as shown in Fig. 3.16 (a). These null points are then averaged to find the

local minimum corresponding to the circuit phase ( $\phi_c$ ). The averaging is done to eliminate any effects of dc offset in the deflection characteristic. At this point the probe phase is set equal to the circuit phase and the A parameter is varied until the deflection is nulled again as shown in Fig. 3.16 (b). This null point corresponds to the amplitude of the measurement signal ( $V_c$ ).

### 3.11 Measurement of Passivated Circuits

The nulling technique allows for arbitrary node probing without the need for complex calibration schemes. The measurement becomes invariant to the mechanical parameters of the cantilever probe and more importantly  $dC/dz$  which is conductor geometry dependent. The independence on  $dC/dz$  allows for probing passivated circuits where the probe to circuit spacing is variable and often unknown depending on the process. The nulling technique allows for accurate measurement of amplitude and phase at different probe to circuit spacings as shown in Fig. 3.17.

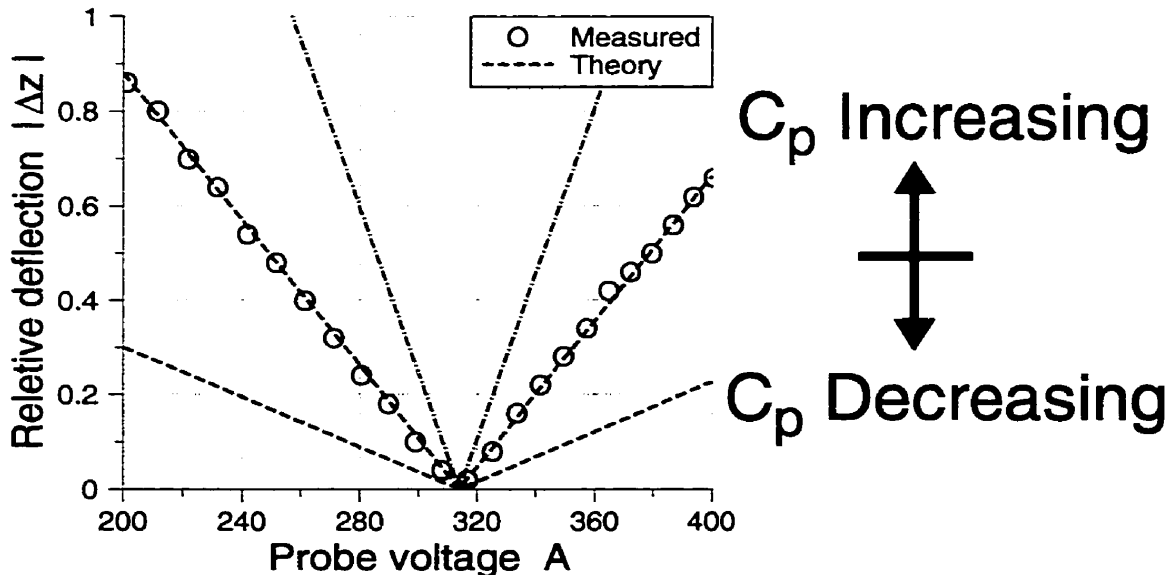


Fig. 3.17: Amplitude nulling at different probe to circuit spacings

When the probe is closer, the deflection is larger due to increasing  $dC/dz$  but the important thing is that all three curves null at the same point, hence the same voltage is measured. Of course there are limits to how far the probe can be moved away from the measurement conductor. As we move away from the target conductor, the SNR will decrease along with the spatial resolution, as the probe will begin to interact with other conductors on the die.

### 3.12 Sensitivity

In Scanning Force Probing, the dominant form of noise is the thermal vibration of the probe[28]. If we model the probe as being a mechanical spring capable of one dimensional motion, it will possess approximately  $0.5kT$  of thermal energy. The probe will vibrate at a noise bandwidth ranging from 10 to 100 KHz depending on the cantilever. The noise power spectral density can be estimated if we consider the input thermal force acting on the cantilever as a white Gaussian noise with a power density given by[28]

$$F_n^2(\omega) = \frac{4k_B T k_B}{\omega_r Q} \quad (3.24)$$

This noise source is passed through the mechanical transfer function of the probe as shown in Fig. 3.18.

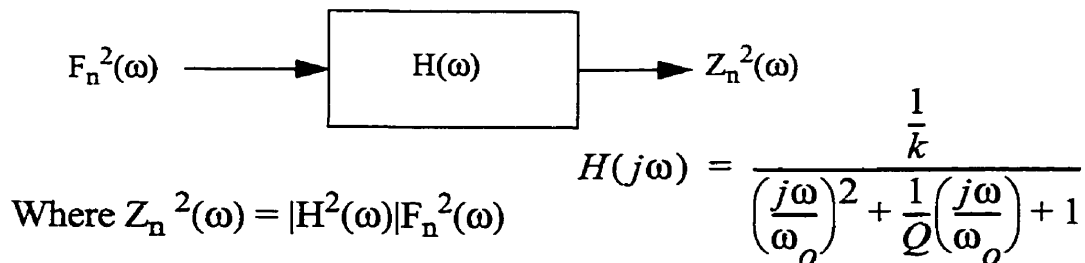


**Fig. 3.18:** Noise transfer characteristic of probe

Using the transfer function in eqn. 3.3, we can compute the expected spectral power density of the deflection signal to be

$$Z_n^2(\omega) = \frac{\left(\frac{Q}{k}\right)^2 \left(\frac{\omega_r}{\omega}\right)^2}{1 + Q^2 \left(\frac{\omega_r}{\omega} - \frac{\omega}{\omega_r}\right)^2} 4k_B T \frac{k}{\omega_r Q} = \frac{4k_B T \left(\frac{Q}{k}\right) \omega_r}{\omega^2 \left(1 + Q^2 \left(\frac{\omega_r}{\omega} - \frac{\omega}{\omega_r}\right)^2\right)} \quad (3.25)$$

A plot of the theoretical deflection power density is shown in Fig. 3.19 along with the measured spectrum using a spectrum analyzer.

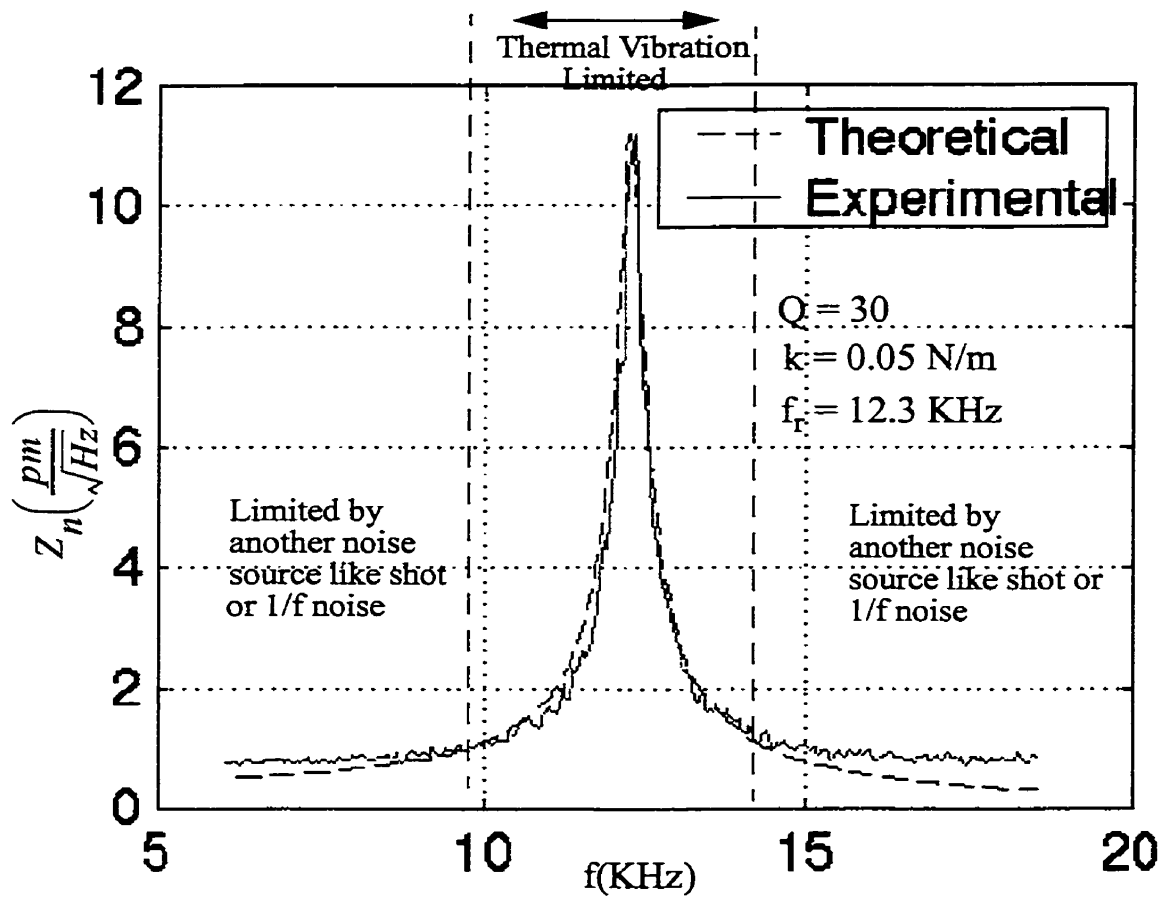


Fig. 3.19: Theoretical and experimental deflection noise density

Unfortunately the deflection spectrum cannot be measured directly, since the spectrum analyzer is connected to the photodetector difference signal. Knowledge of the deflection sensor transfer function is needed to translate the measured voltage to deflection signal. The deflection sensor transfer function was measured to be 0.8  $\mu\text{m}/\text{V}$ . The theoretical curve deviates from the measured one after moving 2 KHz away from resonance which may be due to the presence of other types of noise like 1/f and shot noise from the optics.

In most cases the measurement is made at the resonant frequency of the probe therefore we can approximate the rms noise with[14]

$$\Delta Z_n = \sqrt{Z_n^2(\omega = \omega_r)\Delta f} = \sqrt{\frac{4k_B T Q \Delta f}{\omega_r k}} \quad (3.26)$$

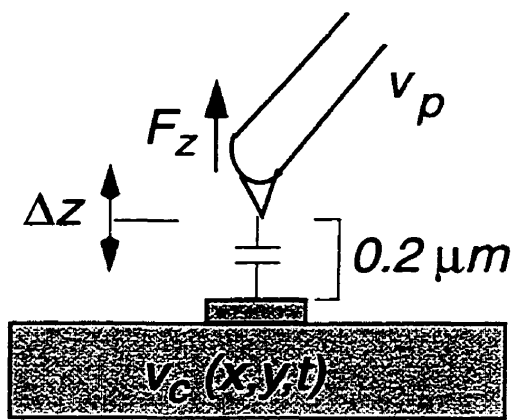
We can approximate the rms signal deflection as

$$\Delta z = \left| \frac{1}{\sqrt{2}} \frac{\partial}{\partial z} C \frac{Q \delta}{k T} v_p \right| v_c(x, y) \quad (3.27)$$

Equating this formula with eqn. 3.26, the sensitivity of the instrument is

$$V_{MIN} = \frac{\sqrt{2}}{\frac{\partial C}{\partial z} \frac{Q \delta}{T} v_p} \sqrt{\frac{4k_B T k \Delta f}{\omega_r Q}} \quad (3.28)$$

This expression indicates that the mechanical properties of the cantilever greatly effect the noise performance of the instrument. The optimal cantilever for EFM applications would be one with very large Q and small spring constant. Also using of a lockin amplifier, measurement bandwidths of 10's of Hz can be achieved for further noise reduction. If we consider a test scenario where the probe to circuit spacing is 200 nm (typical for unpassivated circuits) and using typical mechanical and electrical parameters we can estimate the sensitivity (Fig. 3.20).



$$Q \approx 50$$

$$k \approx 0.05 \text{ N/m}$$

$$f_r \approx 15 \text{ kHz}$$

$$C \approx 0.7 \text{ fF}$$

$$\frac{\partial C}{\partial z} \approx 80 \text{ pF/m}$$

$$\delta/T \approx 1$$

$$V_p = 1$$

$$V_{MIN} \approx 0.2 \frac{\text{mV}}{\sqrt{\text{Hz}}}$$

**Fig. 3.20:** Sample sensitivity calculation for 200 nm probe to circuit spacing

The calculated sensitivity is a little idealized especially when probing passivated circuits where the probe to circuit spacing could range from 1-3  $\mu\text{m}$ . Also the  $\delta/T$  term is often much smaller than unity especially in the case of the pulse sampling technique.

### 3.13 Mechanical Structure of the EFM Probe Station

A photograph of the EFM station used in this research is shown in Fig. 3.21. It includes the probe, probe PCB, piezo-positioners and the beam bounce deflection sensor.

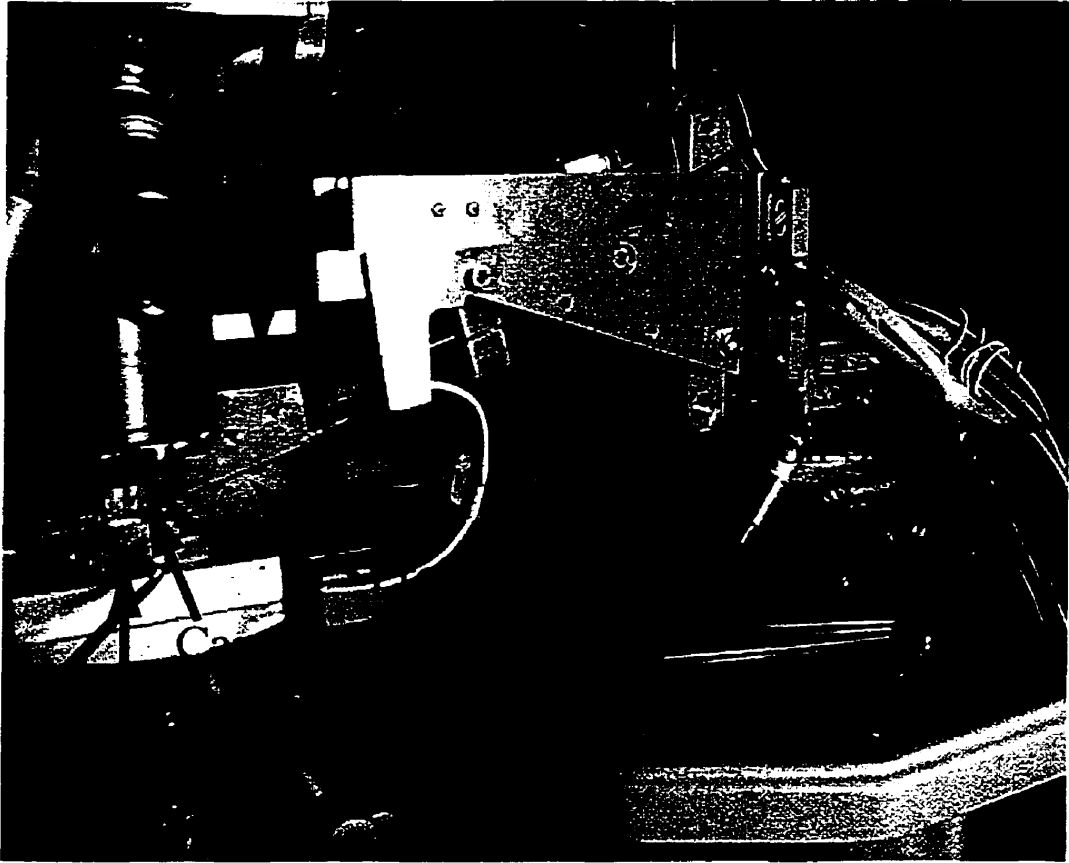


**Fig. 3.21:** *Photograph of EFM probing instrument*

The laser and piezo adjustments can be made using a computer connected to the probe instrument.

### **3.14 Summary**

In this chapter the fundamental components of scanning force probing have been introduced. In the subsequent chapters, the sinusoidal sampling technique will be used to probe a variety of different circuits at frequencies ranging from 1 to 16 GHz. Different hardware implementations of this technique will also be considered.

## Chapter 4: Vector Voltage Measurements at 1 and 2 GHz

### 4.1 Introduction

In this chapter, the experimental setup and results of 1-2 GHz measurements on several practical circuits will be discussed. The microwave components required to implement the mathematics will also be considered.

### 4.2 Hardware Description

In the previous chapter, a mathematical model for the sinusoidal sampling technique was introduced and now some detail can be provided on the required hardware needed to implement the mathematics. Fig. 4.1 demonstrates the microwave circuitry used to implement the 1-2 GHz measurements.

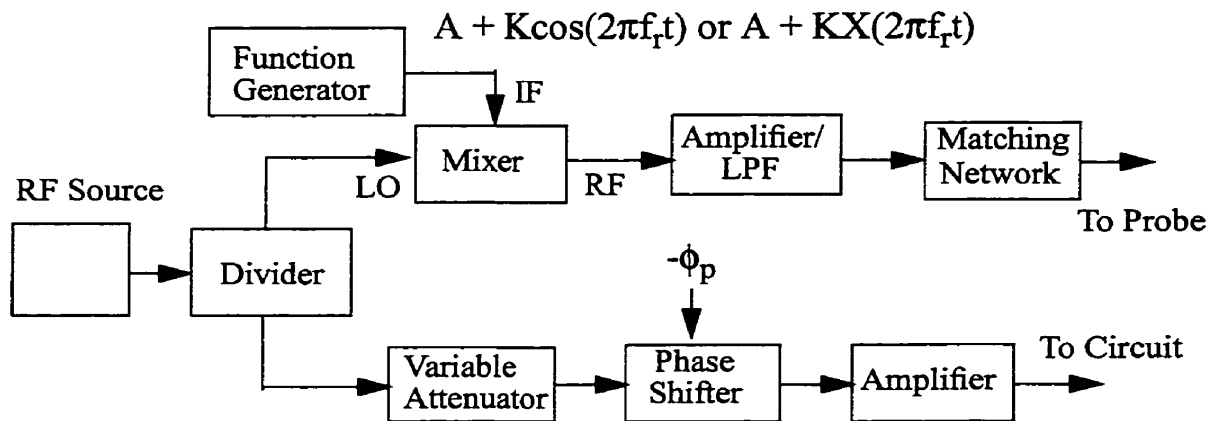
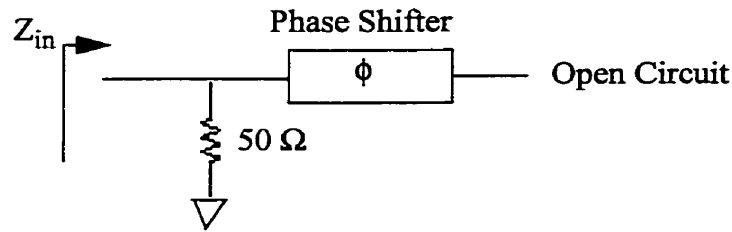


Fig. 4.1: Sinusoidal sampling hardware configuration

The typical EFM realization involves using a base RF source which is split using a power divider. One half of the power is passed through a mixer which uses a function generator to modulate the IF port at the resonant frequency of the probe. Often it is simpler to implement the modulation using square modulation ( $A + KX(t)$ ) rather than sinusoidal. This has no effect on the overall deflection expression, except it introduces an extra  $4/\pi$

factor in eqn. 3.23 from the fundamental fourier coefficient of a square wave. The modulated signal is typically passed through a low pass filter and an amplifier to overcome conversion loss of the mixer, filter out higher order harmonics and enhance the nulling dynamic range of the instrument. The amplified signal is passed through a matching network designed to present a 50 Ohm load to the amplifier.

The matching network can be implemented in one of two ways. The first involves using a shunt 50 Ohm resistor with a tunable phase shifter as shown in Fig. 4.2.



**Fig. 4.2:** Matching network using adjustable phase shifter

The input impedance can be expressed as a function of the phase using the open circuited transmission line equation

$$Z_{in} = \frac{-j2500 \cot(\phi)}{50 - j50 \cot(\phi)} \quad (4.1)$$

When the phase is any multiple of half wavelength ( $\phi=n\pi$ ) the input impedance will be 50 Ohms neglecting loss in the cable assembly. This method works adequately for lower frequency measurements like 1-2 GHz since parasitics associated with the 50 Ohm surface mount resistor is minimal. At higher frequencies we typically employ a series attenuator to reduce the magnitude of the reflected wave as shown in Fig. 4.3. Often only small

attenuators are needed since high frequency losses in the probe cable itself can bring the input impedance quite close to 50 Ohms.

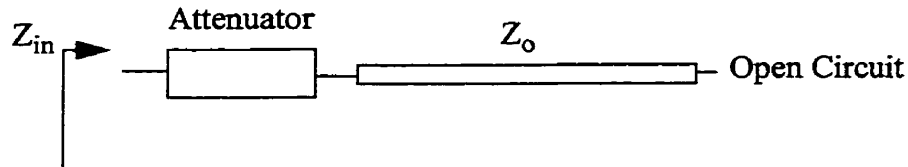


**Fig. 4.3:** *Series attenuator matching scheme*

In this technique the probe voltage is sacrificed for improved matching where the variable phase shifter scheme doesn't have that problem. In this chapter the variable phase shifter matching technique will be employed.

On the circuit side, the signal is passed through a combination of amplifier and variable attenuator to control the amount of input power to the circuit under test. Often a manual phase shifter is placed in series on the circuit side. In the previous chapter, the nulling technique involved modifying the probe phase, but in this setup we are modifying the circuit phase and doesn't affect the instrument since all phase measurements are relative. The important thing to note is that adding a phase lag on the circuit side effectively incurs a phase lead on the probe side.

### 4.3 1 GHz Hardware Description and Calibration

The 1 GHz hardware block diagram is shown below in Fig. 4.4.

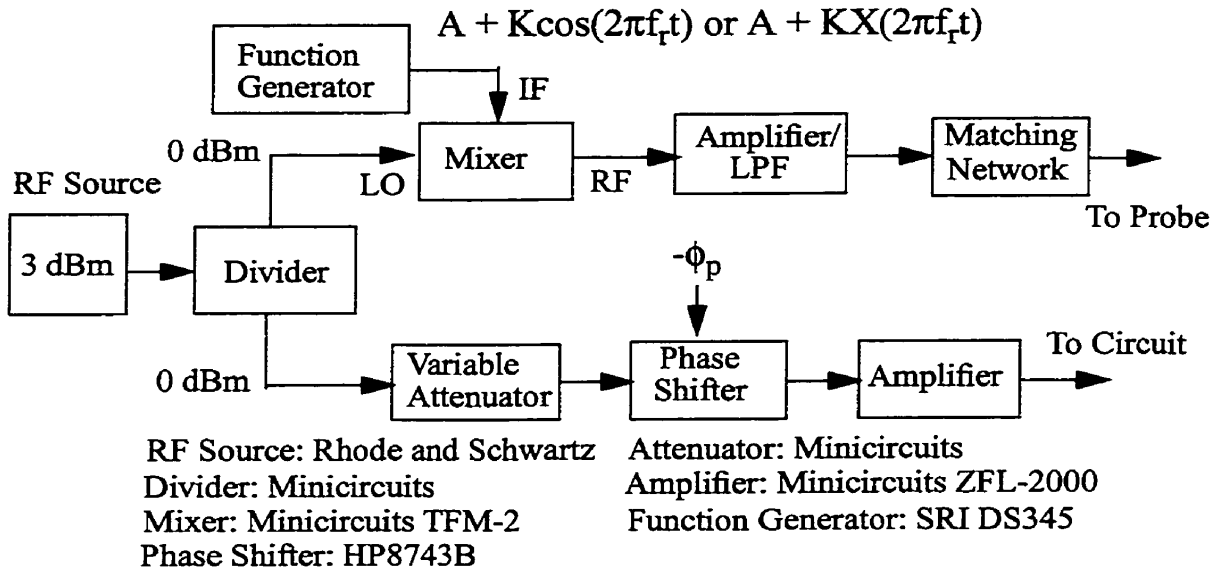


Fig. 4.4: 1 GHz measurement hardware block diagram

Before measurements can be made, a calibration process is required since nulling values are only known in terms of voltage settings on the DS345 function generator. The calibration takes into effect the mixer, cable loss and only has to be done once for each setup. The calibration procedure consists of varying a known voltage and plotting nulling values(A) as a function of voltage. The calibration setup involves probing a 50 Ohm microstrip transmission line. The input signal amplitude was varied using combinations of minicircuits attenuators as shown in Fig. 4.5.

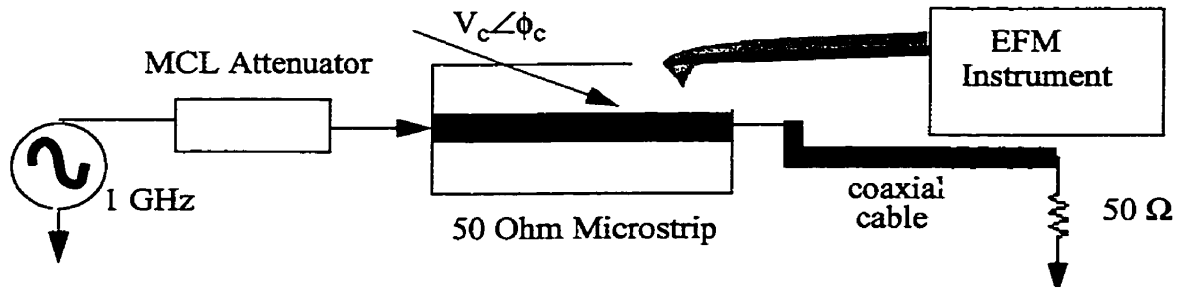


Fig. 4.5: 1 GHz calibration setup

The transmission line was terminated to 50 Ohms by a repetitive sampling oscilloscope where the signal amplitude was measured. The loss was measured for the coaxial cable feeding the oscilloscope which was factored out of the measured signal level. The experimental nulling point versus voltage curve is demonstrated in Fig. 4.6.

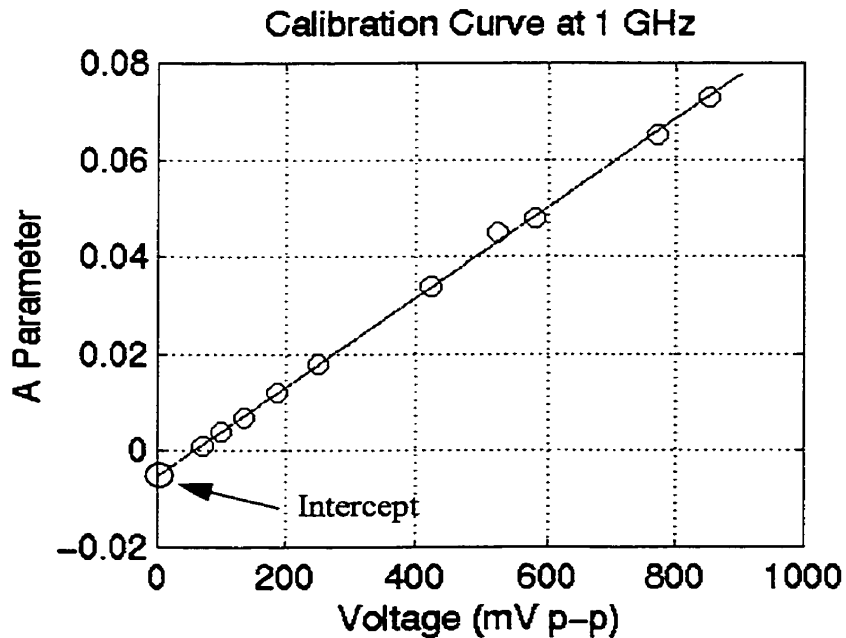


Fig. 4.6: Calibration curve at 1 GHz

Using the above curve enables us to map measured null points(A) with the corresponding signal amplitude. As expected, there is a linear relationship as suggested by the mathematical formula seen in the previous chapter. It is interesting to note the fact that the

curve does not pass through the origin as expected from the mathematical equation. This can be explained if we consider the nature of the mixer being used in this setup. In these measurements a 1 GHz RF signal is incident on the LO port while a modulating signal is used on the IF port as shown in Fig. 4.7.

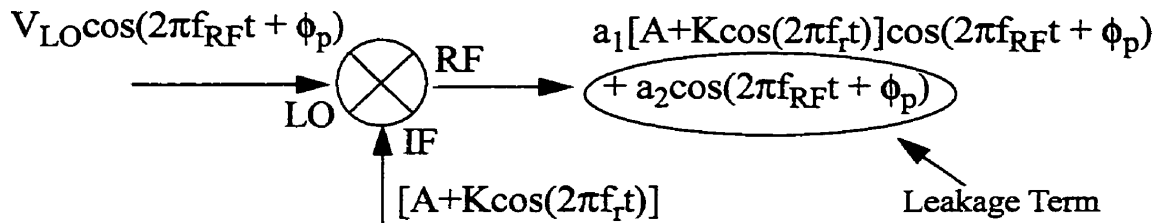
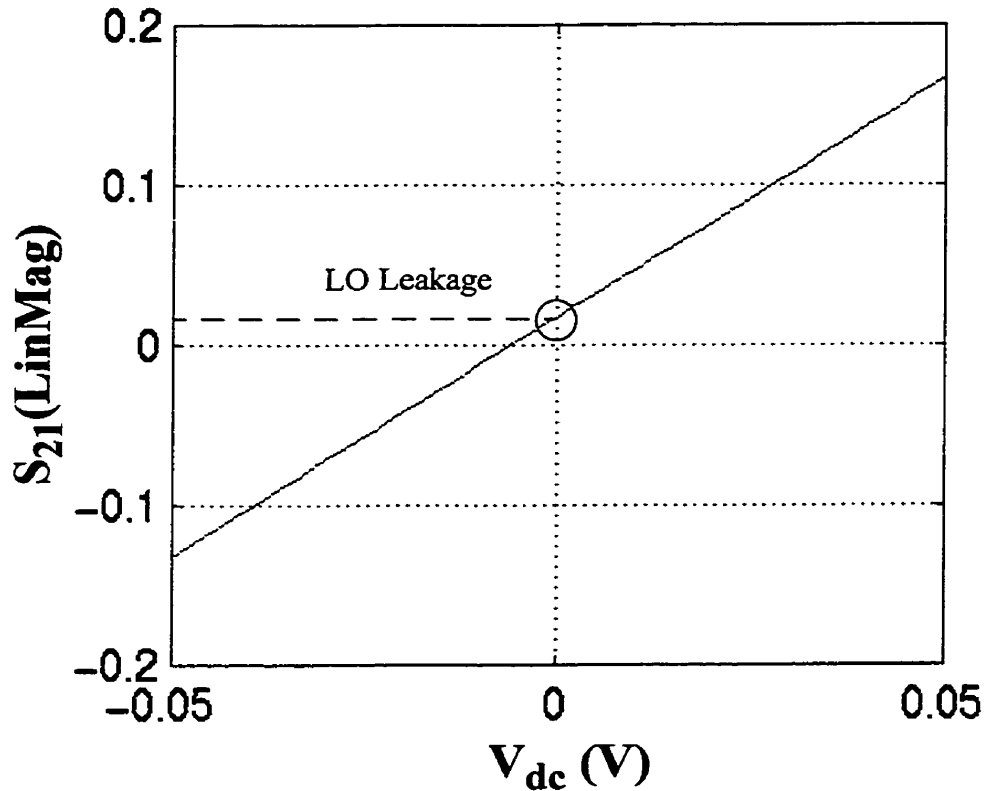


Fig. 4.7: Mixer harmonics at 1 GHz

Unfortunately mixers are far from ideal, since there is always a small leakage signal from the LO to the RF port as shown in Fig. 4.7. This is obvious if we consider the plot of RF amplitude versus a DC modulating IF signal as shown in Fig. 4.8.



**Fig. 4.8:** Minicircuits TFM-2 mixer characteristic

Notice that the characteristic is linear which is expected since the IF voltage is well below the 1 dB compression point of the mixer. There is an intercept on this curve due to the fundamental LO leakage term shown in Fig. 4.8. The minicircuits TFM-2 mixer has a LO to RF isolation of around -30 dB with 0 dBm of LO input power. This results in about -30 dBm of leakage signal at 1 GHz. Unfortunately this will build in a constant offset to the following deflection characteristic

$$\Delta z|_{fr} \propto A - V_c \cos(\phi_p - \phi_c) + V_{Leakage} \quad (4.2)$$

The effect is obvious in Fig. 4.9 where a DC level has been added to the expected sinusoidal deflection curve.

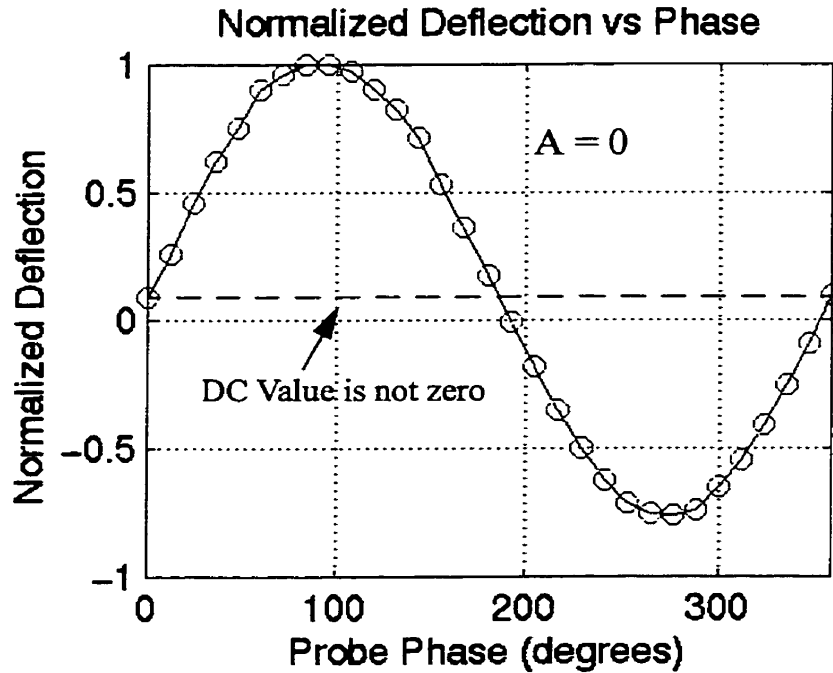


**Fig. 4.9:** Measured 1 GHz deflection versus probe phase including LO leakage effect

This effect is not detrimental to the phase measurement since null points are being averaged but it will add a small intercept on the calibration curve as seen in Fig. 4.6.

#### **4.4 Measurement of a Texas Instruments LNA**

In this section, amplitude and phase measurements will be presented on a GaAs LNA from Texas Instruments[29]. This circuit has a 3 dB bandwidth of 3.5 GHz with a nominal 19 dB gain over this bandwidth. The circuit schematic is shown in Fig. 4.10.

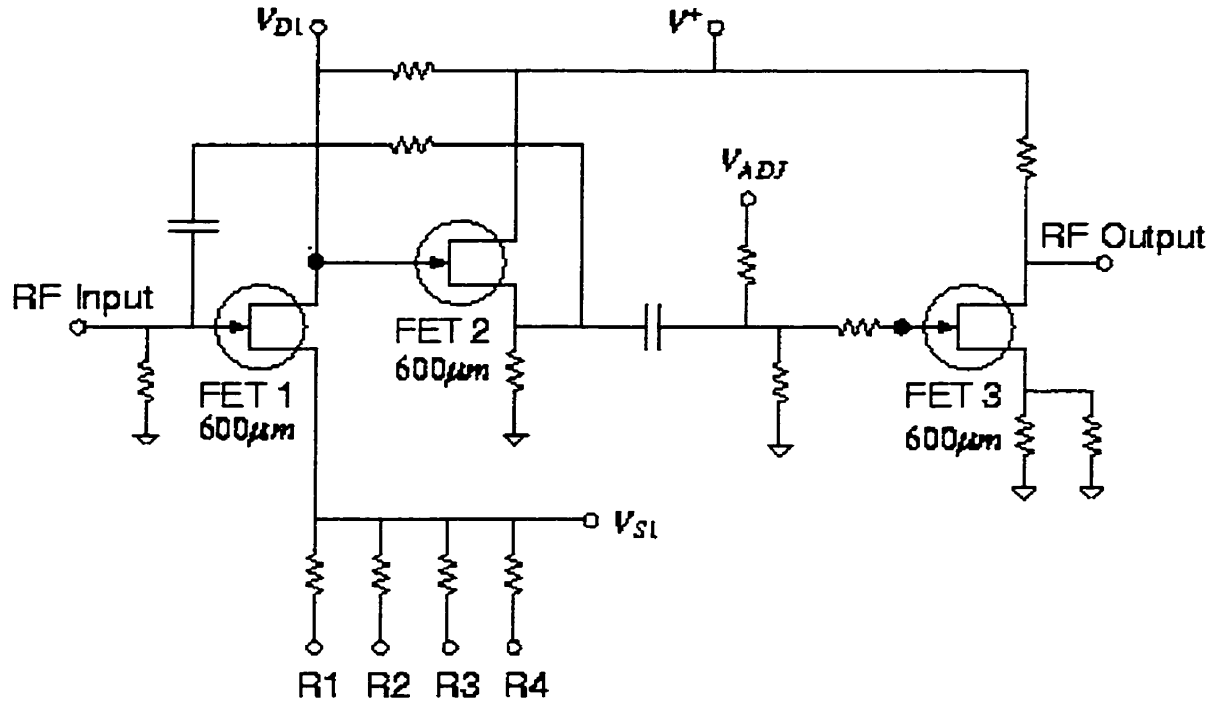
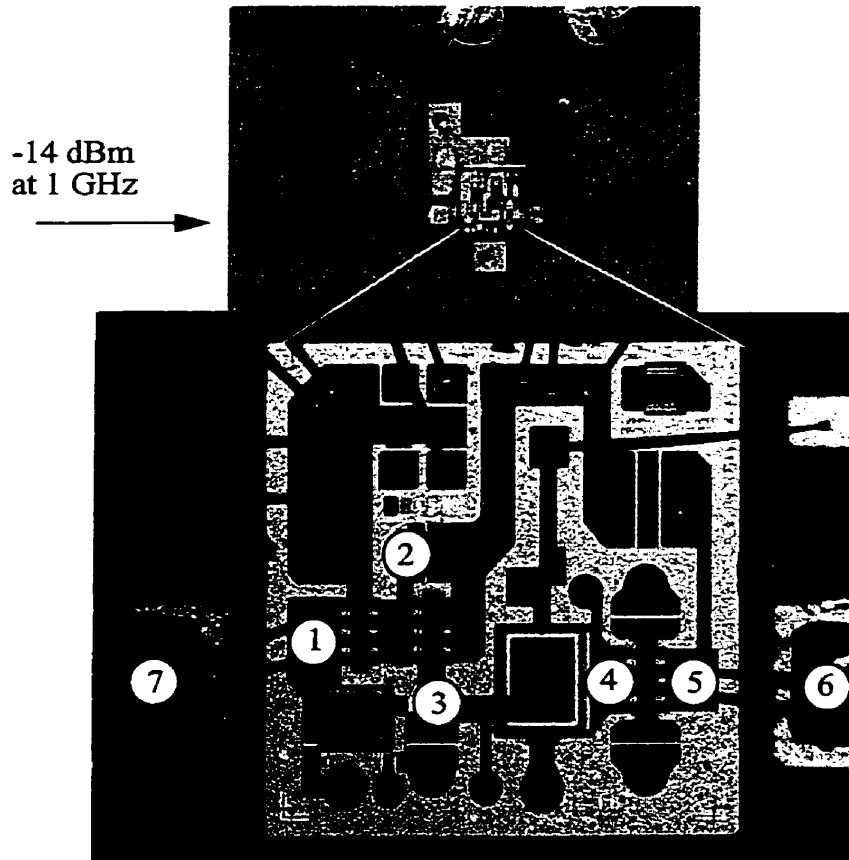


Fig. 4.10: Circuit schematic of TI LNA[29]

This circuit consists of a two stage amplifier with resistive feedback followed by an output buffer designed to drive a 50 Ohm load. Both the input and output pads are AC coupled using blocking capacitors integrated into the pads. The die is mounted on a sapphire substrate with the RF pads wirebonded to two 50 Ohm microstrip transmission lines which run to the input and output SMA connectors as shown in Fig. 4.11.



**Fig. 4.11:** TI LNA package and microphotograph of circuit die

The small microstrip lines are suitable for measuring the input and output signal of the amplifier for S-Parameter and gain measurements. Fig. 4.11 demonstrates the probing points which includes the input and output of each amplifier stage along with the input and output transmission lines.

Measurements at 1 GHz were done using both the calibrated EFM instrument and a 1 GHz bandwidth contact probe(picoprobe) at the nodes specified in Fig. 4.11. The results are tabulated in Table 4.1. Note, even though the picoprobe has a 1 GHz bandwidth, we assume it still behaves linearly and measurements are scaled by the appropriate factor at 1 GHz.

Node	EFM (mVpp)	Contact Probe (mVpp)
1	111∠0°	110∠0°
2	947∠167°	766∠173°
3	795∠164°	638∠173°
4	784∠163°	652∠165°
5	990∠-32°	823∠-28°
6 (output t- line)	947∠-32°	840∠-28°
7(input t- line)	111∠2°	110∠0°

**Table 4.1** : EFM and contact probe measurements on TI LNA

Using nodes 6 and 7 we can estimate the forward gain of the amplifier using both EFM and the contact probe in comparison to the specifications.

$$\text{EFM: } S_{21} = 18.6 \text{ dB} \angle -34^\circ$$

$$\text{Contact Probe: } S_{21} = 17.6 \text{ dB} \angle -28^\circ$$

$$\text{Data Sheet: } S_{21} = 18.5 \text{ dB} \angle -36^\circ$$

The agreement between the EFM and data sheet value is superior than that of the contact probe. In the contact probe method, the amplitude and phase must be deduced from the measured waveform on the oscilloscope making phase resolution much more difficult. It is also interesting to note the differences in measured amplitude suggesting a possible loading effect on the circuit. It is important to note that it is difficult to measure S-parameters using EFM since we cannot distinguish between direction of power flow as in the case of a network analyzer. We are actually measuring the voltage signal which is a com-

combination of an incident and reflected wave. In circuits where the input matching is poor, accurate measurement of the S-parameters using EFM is nearly impossible. In this case, our circuit was very well matched with an  $S_{11}$  around -20 dB which means that the measured input voltage is approximately the amplitude of the incident voltage wave.

#### 4.5 1.9 GHz Hardware Description and Calibration

The microwave components used for 1.9 GHz is very similar to the 1 GHz system except it utilizes a Relcom mixer for the modulation and a 2 GHz low pass filter. The calibration scheme used was identical to Fig. 4.5 with a resulting calibration curve shown in Fig. 4.12. Notice that the intercept is much smaller which suggests that the LO-RF leakage of the Relcom mixer is superior to that of the TFM-2 mixer used for the 1 GHz measurements.

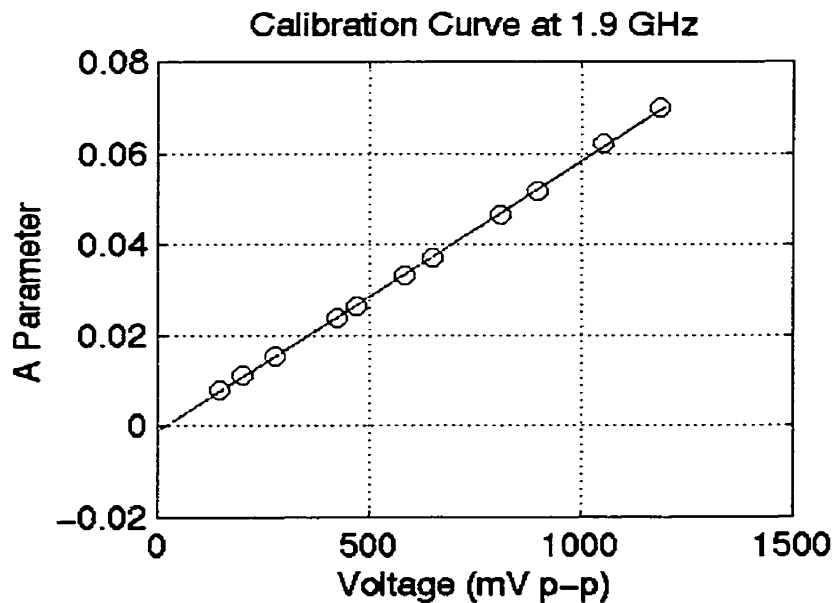
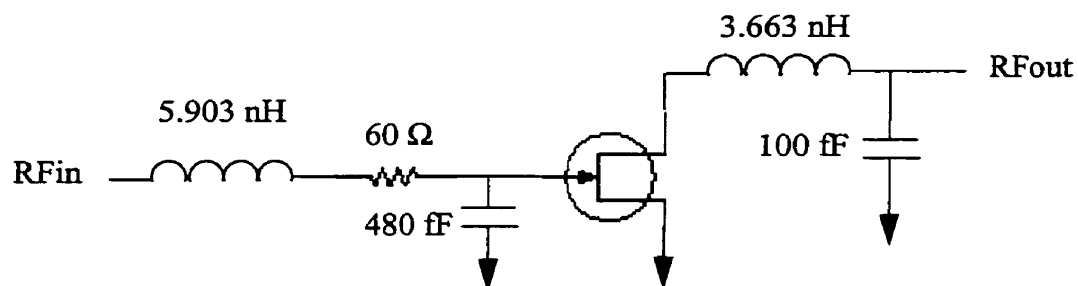


Fig. 4.12: 1.9 GHz calibration curve

### 4.6 Measurement of a Mesfet Amplifier

Measurements were made on a narrow band 1.9 GHz GaAs amplifier. This design was implemented using a CMC supported SAGRF technology using 0.5  $\mu\text{m}$  mesfets[30]. The design IGAMB016 consisted of a single transistor (mesfet) biased through the input and output RF pads as shown Fig. 4.13.



**Fig. 4.13:** Circuit schematic of single stage GaAs amplifier

A microphotograph of the circuit layout is shown in Fig. 4.14.

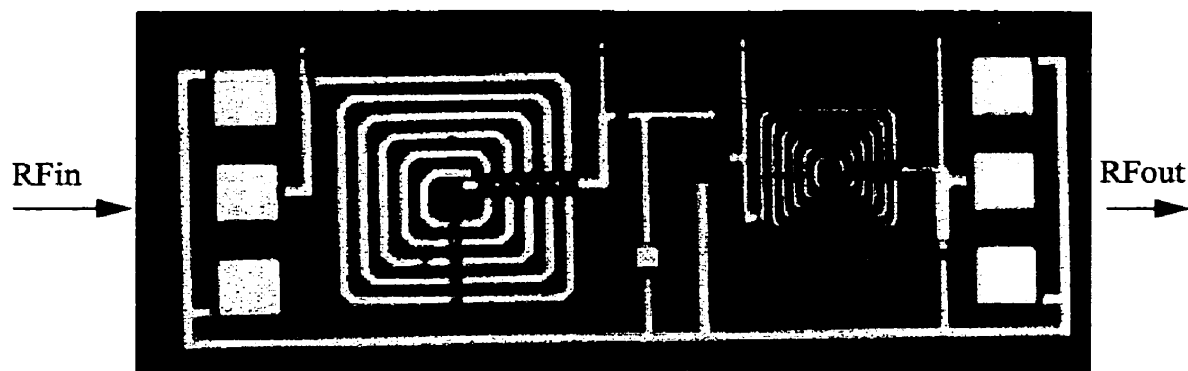


**Fig. 4.14:** GaAs amplifier layout[30]

The amplifier layout has a ground-signal-ground pad configuration to facilitate the use of coplanar on-wafer matched impedance probes which were discussed briefly in chapter 2. The on-wafer probes will supply the RF and the necessary biasing to the gate and drain of the mesfet. The amplifier measurement setup is shown next in Fig. 4.15.

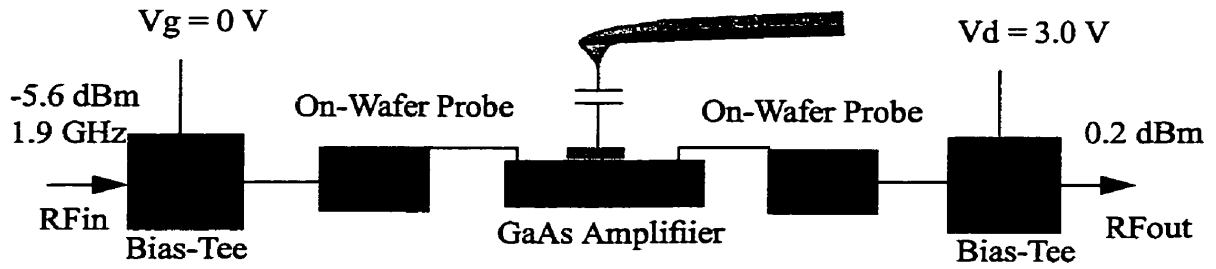


**Fig. 4.15:** Measurement setup for the GaAs amplifier

External bias-tees were used to supply the bias voltages to both the gate and drain of the transistor. The measurement nodes are shown in Fig. 4.16.

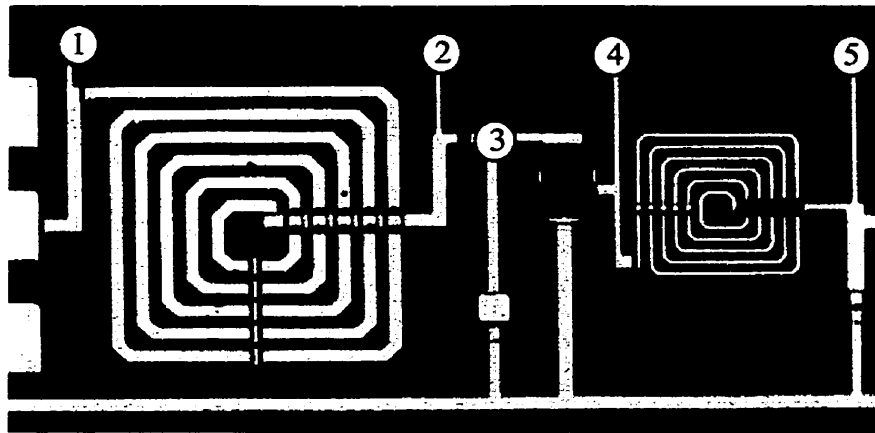


**Fig. 4.16:** Amplifier layout along with measurement points

The stimulus was a  $330 \text{ mV}_{pp}$  signal into  $RF_{in}$  while the output port was match terminated to 50 Ohms. The circuit was also simulated using HSPICE at each node but only in magnitude. The measurement and simulation results are shown in Table 4.2.

Node	EFM (mVpp)	HSPICE (mVpp)
1	473∠0°	360
2	660∠-31°	460
3	507∠-51°	308
4	1081∠105°	1800
5	886∠66°	1440

**Table 4.2:** EFM and simulation results for GaAs mesfet amplifier

The measured insertion gain results of the amplifier at 1.9 GHz using the network analyzer, EFM and HSPICE are

$$\begin{aligned} \text{Network Analyzer: } |S_{21}| &= 9.4 \text{ dB} \\ \text{EFM: } S_{21} &= 5.5 \text{ dB} \angle 66^\circ \\ \text{Simulation: } S_{21} &= 12.1 \text{ dB} \angle 65^\circ \end{aligned}$$

There is quite a large discrepancy between all three values. The simulation results are quite different than the network analyzer measurement which may be due to an inaccurate mesfet model in the HSPICE simulation. This difference is shown between measurement nodes 3 and 4 in the amplifier where the simulated transistor gain was roughly 15 dB while the actual EFM measurement suggests only 6.6 dB. Also, the matching resonant frequency was not quite at 1.9 GHz with an input reflection coefficient of -10 dB which means that the EFM input voltage measurement was a combination of incident and reflected voltage signals and was not indicative of the incident voltage wave.

The internal node measurements makes it possible to measure various transistor parameters. In this case we can estimate the transconductance of the mesfet at the operating bias point. A simple voltage controlled current source model will be employed for the mesfet as shown in Fig. 4.17.

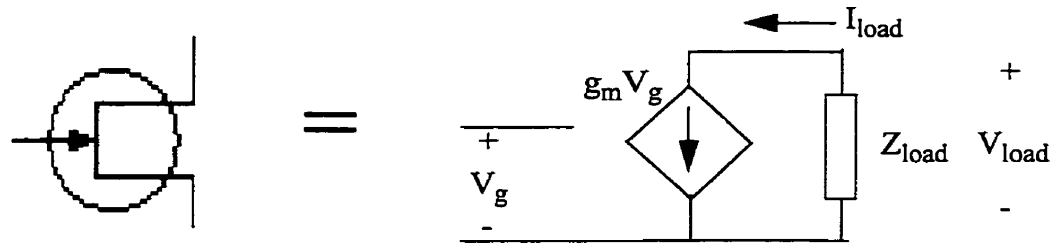


Fig. 4.17: Simplified mesfet model

Using EFM we have measured both  $V_g$  (node 3) and  $V_{load}$  (node 4) which allow for the estimation of  $I_{load}$  that yields the  $g_m$  of the transistor using the model values for the circuit elements.

$$V_g = 507 \angle -51^\circ \text{ mVpp}$$

$$V_{load} = 1081 \angle 105^\circ \text{ mVpp}$$

$$Z_{load} \text{ (at 1.9 GHz)} = 49.8 + j40.8 \ \Omega$$

$$I_{load} = -\frac{V_{load}}{Z_{load}} = 16.8 \text{ mA} \angle -114^\circ$$

$$\text{Therefore } g_m = \frac{I_{load}}{V_g} = 33 \angle -63^\circ \text{ mA/V}$$

The measured  $g_m$  appears to be realistic for a mesfet. Notice that the phase shift between the drain current and gate voltage is not quite  $0^\circ$  as expected. The measured transconductance is approximately  $63^\circ$  lagging which suggests that our simplified model is not quite accurate. A more accurate model would include the necessary parasitic capacitances associated with the gate, source and drain. Also, there may be inaccuracies in the

estimated load impedance due to parasitic resistance and capacitance in the inductor models.

#### ***4.7 Summary***

In this chapter, we have seen the capability of EFM to perform 1 and 2 GHz internal node measurements. A LNA and mesfet amplifier were probed providing results very similar to the data sheet specifications. These measurements require manual adjustments of phase and amplitude to implement the heterodyne nulling technique. This can be tedious since it lacks automation and data collection capability. In the next chapter, a different hardware approach will be introduced to allow for a more automated probing environment to implement higher frequency measurements.

## Chapter 5: I/Q Modulation

### 5.1 Modulation Problem

All measurements done in the previous chapter involved implementing the heterodyne nulling technique using manual phase shifters and mixers as shown in Fig. 5.1.

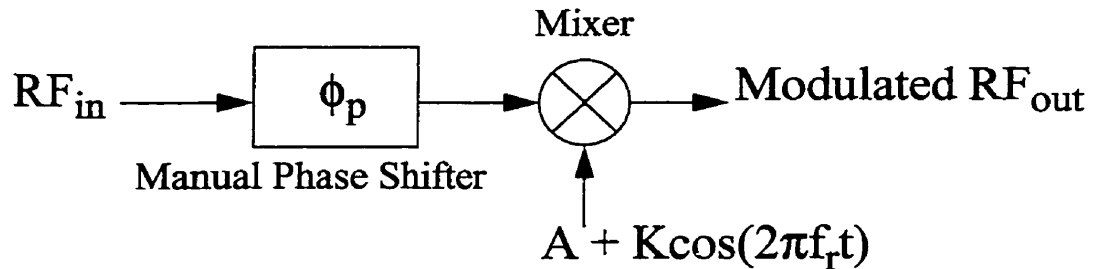


**Fig. 5.1:** Conventional modulation scheme

In the conventional system, the probe phase will be adjusted manually to implement the appropriate phase nulling. These phase shifters typically function on the principle of adding or removing physical length. At lower frequencies, adjusting physical lengths will provide enough phase resolution but as frequency increases, their resolution will decrease. The phase sensitivity can be assessed by

$$\Delta\phi = \frac{2\pi}{\lambda}\Delta L \quad (5.1)$$

where  $\Delta L$  is the smallest manually adjustable length. As wavelength decreases, the phase sensitivity degrades therefore for measurements above and including 10 GHz, a manual shifter is not very practical.

The modulation scheme is typically done using a mixer where a function generator is used to provide the modulation to the IF port. During amplitude nulling, the modulation offset  $A$  is adjusted manually until the deflection is nulled.

This configuration is very difficult to automate since both the modulating IF signal and the phase shifter must be controllable by a computer. The function generator can be controlled through an analog output, but the phase shifter cannot. For this to work properly, we need an analog or digital controllable phase shifter but the output phase is often very dependent on frequency.

This chapter will introduce a very efficient way of implementing both phase shifting and modulation in a digital control system environment.

### 5.2 Theory of I/Q Modulation

The phase and amplitude of the probe signal can be controlled using a single component called an I/Q modulator. This replaces both the manual phase shifter and microwave mixer as shown in Fig. 5.2.

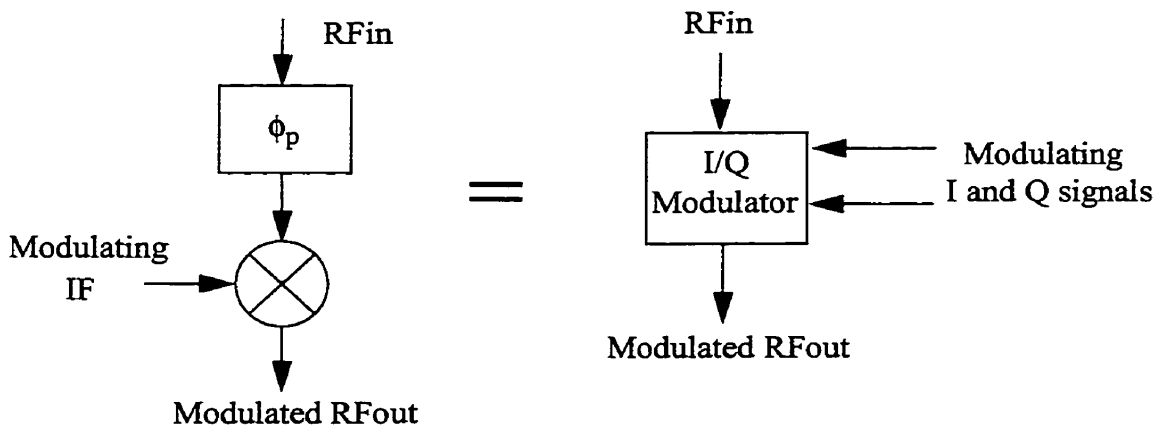


**Fig. 5.2:** Equivalence using I/Q modulator

The software implementation requires strategically modifying the I and Q control signals to implement the desired phase shift and modulation amplitude. An internal block diagram of a typical I/Q modulator is shown next in Fig. 5.3.

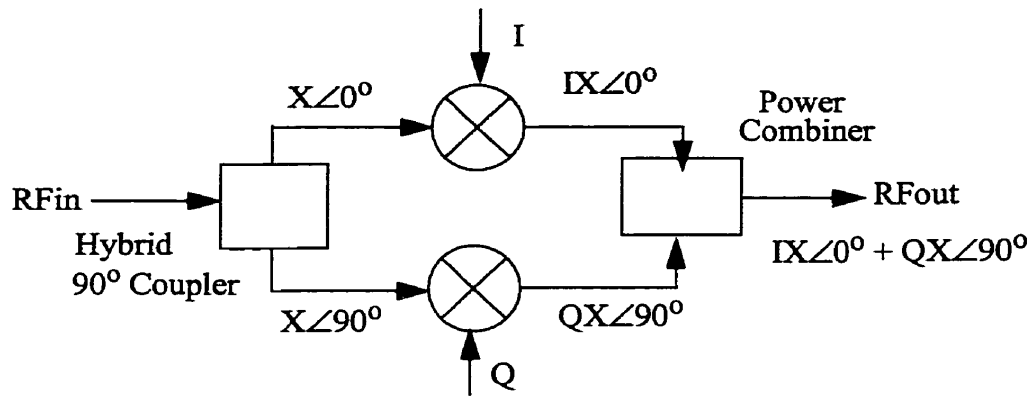


**Fig. 5.3 :** Internal block diagram of I/Q modulator

In the modulator, the input RF signal is passed through a  $90^\circ$  hybrid coupler which passes two equal amplitude signals in quadrature phase. These signals pass through separate attenuators controlled by the I and Q ports. The output of the attenuators are passed through an in-phase power combiner to vector sum the two phasers. By controlling the I and Q ports, we can effectively achieve any amplitude and phase in the output RF signal. This can be explained using a simple analogy in linear algebra. Consider two linearly independent vectors(orthogonal), I and Q as shown in Fig. 5.4.

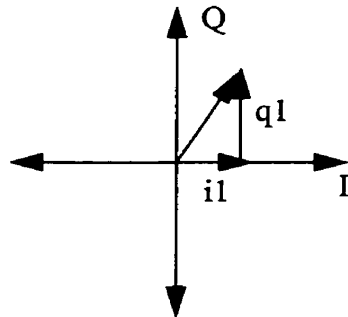


**Fig. 5.4 :** 2 dimensional I/Q space

Since I and Q are linearly independent, we can generate any vector in 2 dimensional space using some linear combination of these vectors. This is the same principle with the I/Q modulator. The I and Q are orthogonal therefore by adjusting the I and Q weights we

can generate the desired output vector with known amplitude and phase. This will be the technique employed to control the phase and amplitude of the sampling signal used in the EFM probing instrument.

### 5.3 I/Q Modulation in EFM

During the measurement process we have to synthesize a probe signal of the form

$$V_p(t) = (A + KX(t)) \cos(2\pi f_{RF}t + \phi_p) \quad (5.2)$$

where  $X(t)$  is a modulation square wave of fundamental frequency  $f_r$  (resonant frequency of the probe). To synthesize this waveform using the I/Q modulator requires the modulation between two different vectors  $180^\circ$  out of phase in I/Q space as shown in Fig. 5.5.

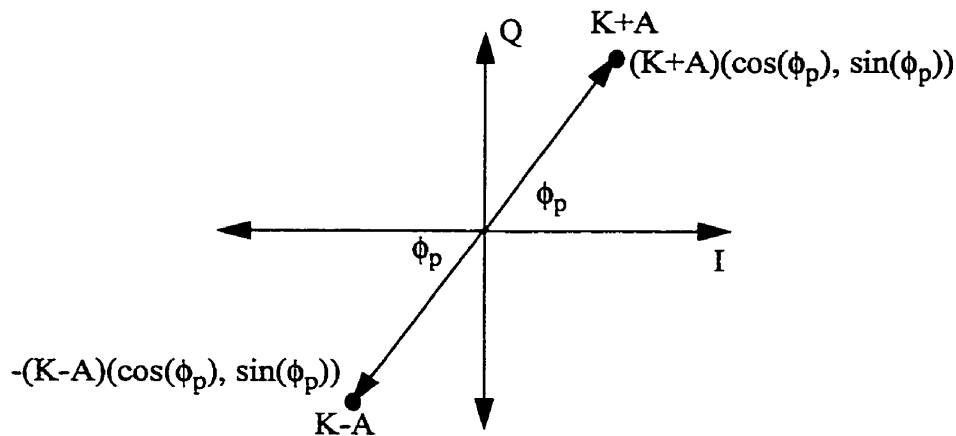


**Fig. 5.5 : Required modulation vectors**

The above figure demonstrates the two different vectors along with their respective I/Q coordinates. The I and Q ports must be modulated at  $f_r$  between the two sets of coordinates to implement the required modulation waveform with all the necessary nulling parameters.

### 5.4 GTMicrowave I/Q Modulator

In this research, we made use of an I/Q modulator provided by GTMicrowave[31].

The part has the following specifications:

- Frequency range: 6-18 GHz
- I and Q I/O : 12 bit
- Conversion Loss: -8.6 dB
- Calibrated Input Power: 0 dBm

This modulator has a built in lookup table to compensate for non-linearities in the I and Q attenuators. Unfortunately the device has a very large conversion loss and therefore the use of an output amplifier is definitely required. The modulator I and Q control is done digitally through the use of two 12 bit vectors. Fig. 5.6 demonstrates the output characteristic of each attenuator as a function of input 12 bit control word.

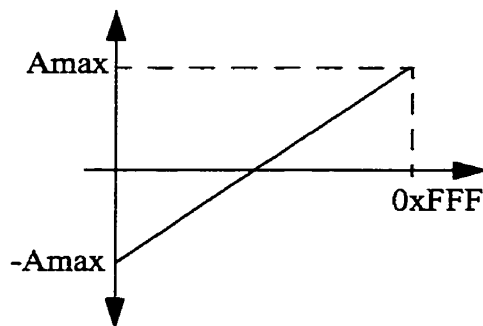


**Fig. 5.6 :** Output amplitude versus 12 bit control word

The LO leakage signal at 10 GHz was measured for an I and Q setting of 0x800 (turned off) which yielded -50 dBm for a 0 dBm input signal. There is 50 dB of isolation which suggests that there will be minimal offset in the deflection characteristic which was seen using the Minicircuits mixer in chapter 4.

### 5.5 I/Q Modulator Hardware Description

To implement the necessary modulation of the instrument, we need to decide on the necessary hardware to facilitate the modulation between two I/Q vectors. The modulation can be done using a multiplexer switching at the resonant frequency of the probe as shown in Fig. 5.7[32].

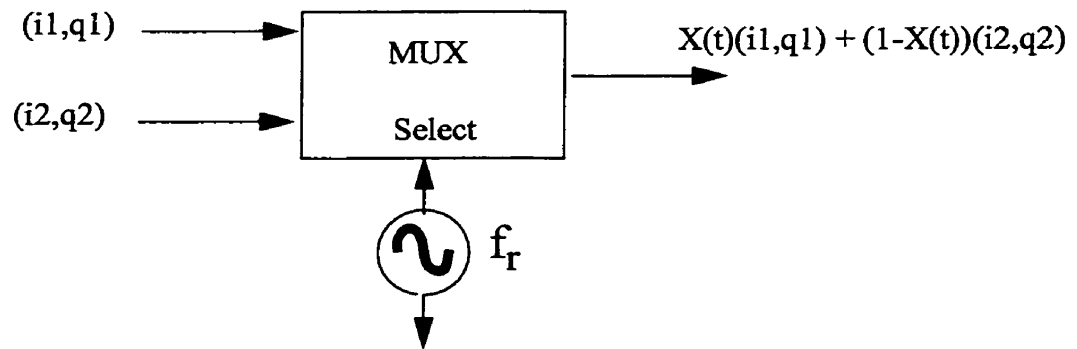


**Fig. 5.7 :** Modulation using a multiplexer

In the case of the GTMicrowave device, the I and Q ports require digital input. This was implemented using a National Instruments Digital I/O card and several CMOS parallel multiplexers. The National Instruments card provides a software interface to the control words while the multiplexers switch between each I/Q vector present on the output of the NI card. The hardware configuration is shown in Fig. 5.8.

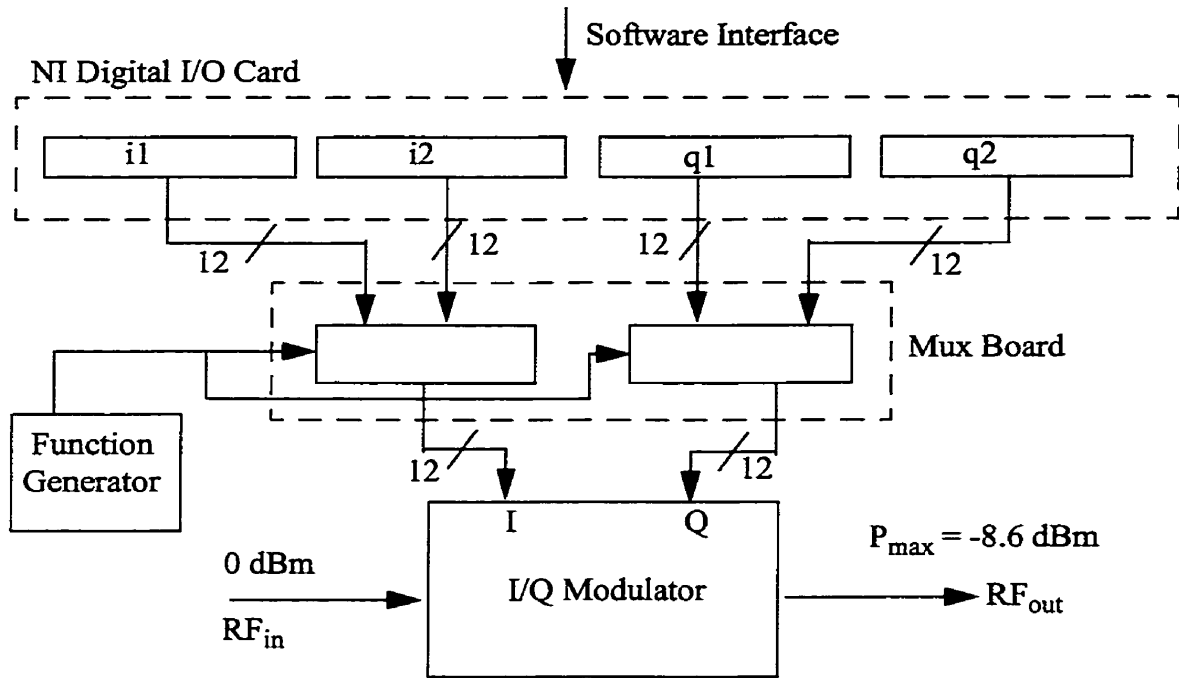


**Fig. 5.8 : I/Q modulator hardware interface**

Both I/Q coordinates (i1,q1) and (i2,q2) are stored in four software writable digital output registers. These outputs are connected to a Mux board which uses a function generator to switch between both coordinates at the resonant frequency of the probe.

### 5.6 Software interface

The hardware interface discussed in the previous section implements the necessary modulation but now it is necessary to calculate the I/Q coordinates in terms of the previously discussed nulling parameters. Recalling Fig. 5.5, we can solve for all the coordinate values given by

$$\begin{aligned}
 i1 &= (A+K)\cos(\phi_p) & i2 &= -(K-A)\cos(\phi_p) \\
 q1 &= (A+K)\sin(\phi_p) & q2 &= -(K-A)\sin(\phi_p)
 \end{aligned}
 \tag{5.3}$$

The software driver will receive parameters  $A$ ,  $K$  and  $\phi_p$  as input and calculate the corresponding  $i_1$ ,  $i_2$ ,  $q_1$ ,  $q_2$  parameters using equations 5.3.  $\phi_p$  will assume the range of 0 to  $360^\circ$  while  $K$  and  $A$  are normalized in the interval between 0 and 1. Fig. 5.9 demonstrates the structure of the I/Q modulator software driver.

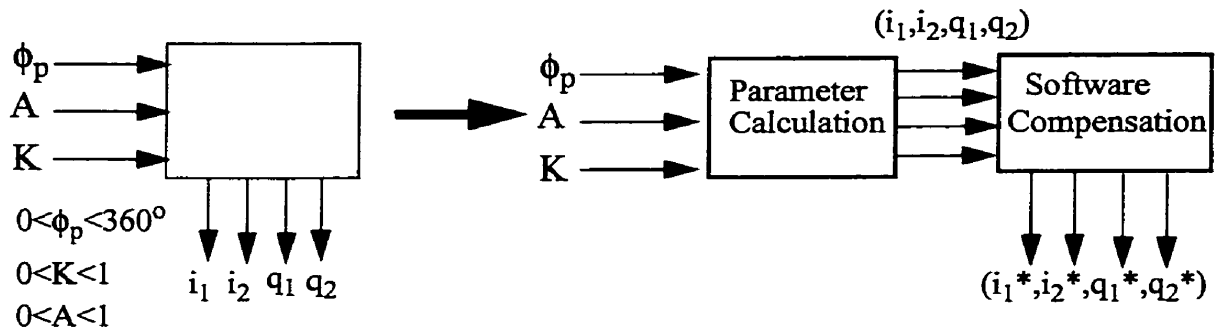


**Fig. 5.9 : I/Q modulator software driver**

In the software driver a compensation block has been added. Since we are using realistic devices, the I and Q attenuator characteristics may not be identical for a given input 12 bit word. The software compensation block will attempt to correct for these inconsistencies. This block will be discussed in more detail in the next chapter since it is very frequency dependent.

### **5.7 Automation of the Heterodyne Nulling Technique**

Using both the hardware and the software driver we can implement a control system to perform the amplitude and phase measurement and thus automate the Heterodyne Nulling Technique.

There are many different approaches to solve this problem, but the most efficient and deterministic would be using a forced nulling technique. Forced nulling is implemented using a combination of positive and negative feedback control systems to force a desired

signal to zero. In EFM we strive to null the measured deflection to extract both amplitude and phase. Let us consider a typical control system used for either phase or amplitude nulling as shown in Fig. 5.10.

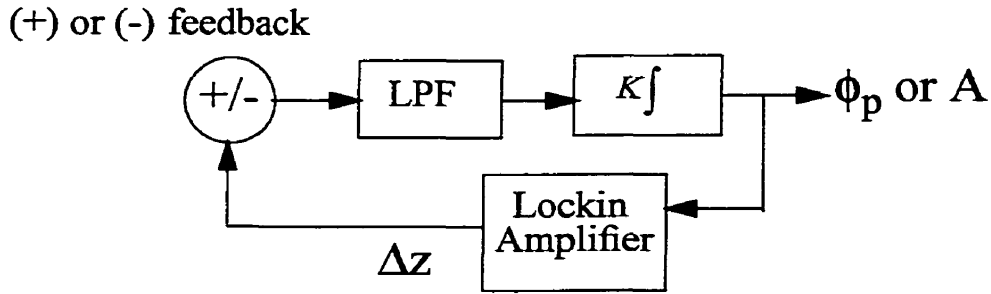


**Fig. 5.10:** Typical nulling control system

In this system, the measured deflection from the lockin amplifier is used as an error signal in either positive or negative feedback mode. The output is passed through a low pass filter to suppress noise and into an integrator with variable gain  $K$ . The control system will continue to modify the  $\phi_p$  or  $A$  until the measured deflection approaches zero and the system is nulled. The question is why do we need to control the type of feedback? In amplitude nulling this is not important but for phase nulling it is crucial.

In phase nulling mode, we can model the transfer function of the lockin amplifier with the following non-linear unit step transfer function as shown in Fig. 5.11. This is assuming a step input starting from  $\phi_{p0}$  to  $\phi_p$ .

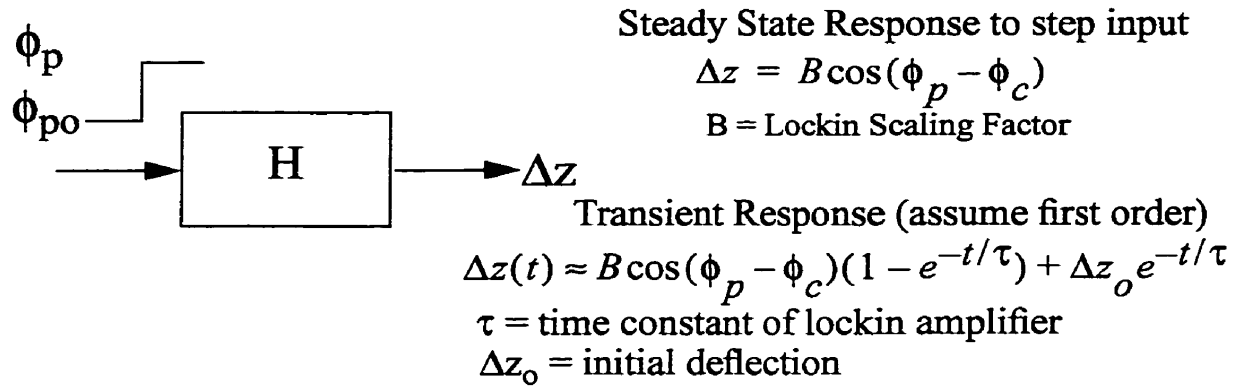


Fig. 5.11: Modelling the lockin amplifier transfer function for phase nulling

For the moment let us assume all signals are in a steady state mode. If we plot the steady state deflection versus input phase( $\phi_p$ ) of the lockin amplifier, we can determine the relative stability of the null points.

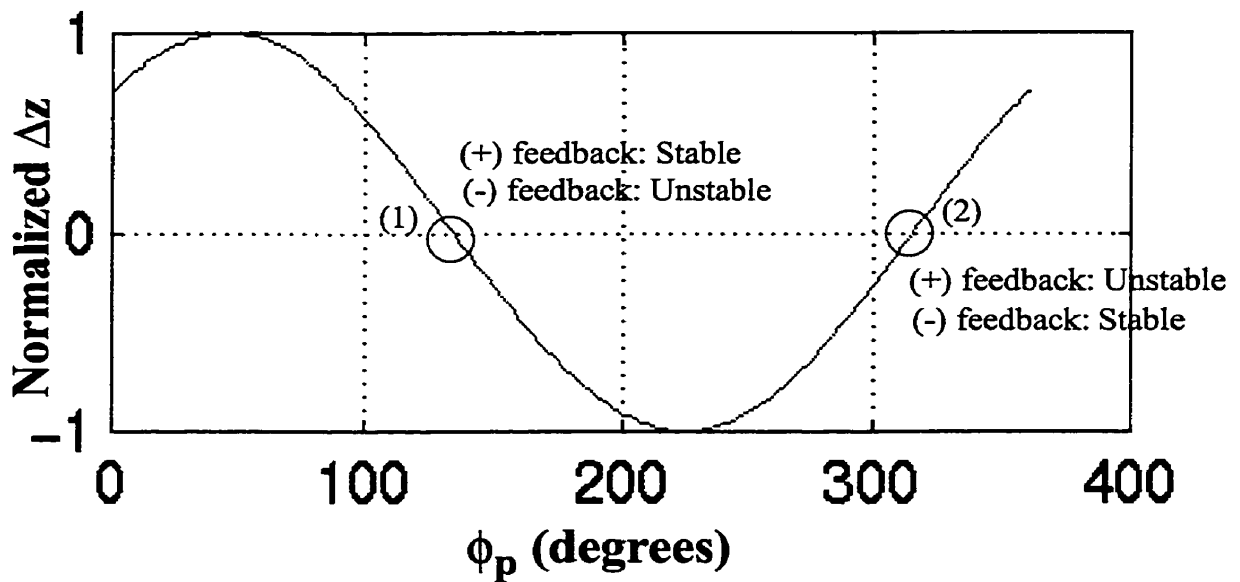


Fig. 5.12: Lockin amplifier output deflection characteristic during phase nulling

From Fig. 5.12 it is apparent that the stability of each null point depends on the sign in the feedback path. We can use this to our advantage to solve for both null points. If we

use positive feedback, we can find null point (1) and if negative feedback is used, the other null point (2) can be extracted. This simplifies the overall software since the same control system can be used to find both null points with only the feedback sign being alternated.

In amplitude nulling, the lockin amplifier unit step transfer characteristic can be described using the equations

$$\text{Steady State: } \Delta z = BA + C \quad (5.4)$$

$$\text{Transient: } \Delta z(t) \approx (BA + C)(1 - e^{-t/\tau}) + \Delta z_0 e^{-t/\tau} \quad (5.5)$$

where B and C are constants and  $\Delta z_0$  is the initial deflection value.

Depending on the phase settings on the lockin amplifier, the slope of the deflection vs A may be positive or negative. In the event of a positive slope, negative feedback must be used where as positive feedback is needed for a negative slope.

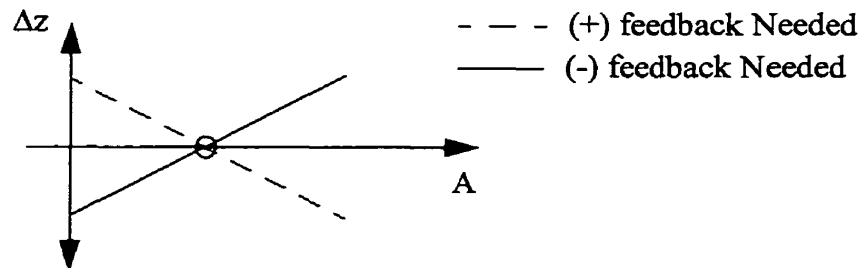


**Fig. 5.13 :** Deflection versus A parameter

The control systems in this research were implemented as a digital system using Lab-view. A more accurate representation of the digital control system is shown in Fig. 5.14.

(+) or (-) feedback

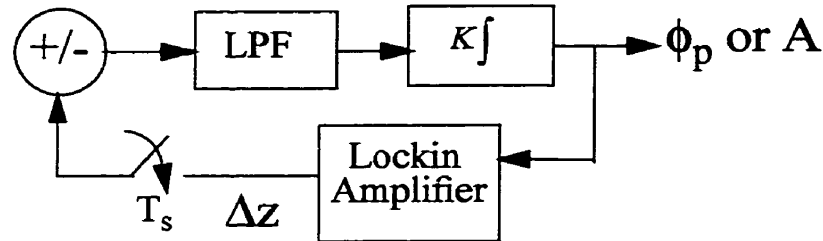


**Fig. 5.14 :** Nulling digital control system

In this system the low pass filter is implemented by averaging a user controllable number of samples from the lockin amplifier. As shown earlier the lockin amplifier has a non-zero analog time constant which can be overcome by introducing a delay between each iteration of the control system. This will ensure that the the lockin amplifier has reached steady state for the next error computation. The software delay must satisfy the requirement that the delay  $> \tau$  of lockin amplifier to avoid sampling of the transient. A lockin time constant of 100 ms is used in most measurements. The integrator gain,  $K$ , is software programmable and can vary for different situations.

The measurement software is implemented using different combinations of this similar control system to measure both amplitude and phase.

## 5.8 Summary

In this chapter the I/Q modulation theory and implementation has been introduced. In theory, this technique should simplify much of the measurement process. In the next chapter the I/Q modulation technique will be used to perform a variety of measurements at 10 GHz including transmission line profiling, phase shifter and distributed amplifier measurements.

## Chapter 6: Vector Voltage Measurements at 10 GHz

### 6.1 Introduction

In this chapter we will make use of the previously discussed I/Q modulator to perform measurements at 10 GHz. The calibration of both the I/Q modulator and instrument will be demonstrated along with measurements of amplitude and phase at 10 GHz. Also several circuits will be probed including a Nortel provided phaseshifter and wideband amplifier. The chapter will also include some transmission line measurements on small CPW structures.

### 6.2 10 GHz Hardware Description

In these experiments, the I/Q modulator has replaced both the manual phase shifter and the RF mixer. The hardware block diagram is shown in Fig. 6.1.

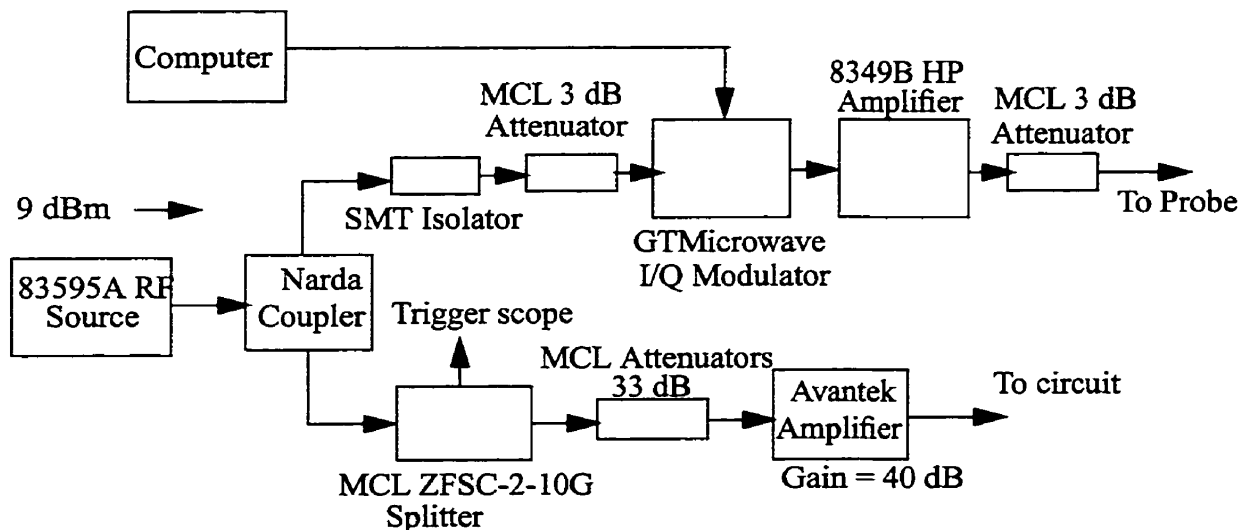


**Fig. 6.1:** 10 GHz EFM hardware configuration

In this setup, the probe circuitry uses a combination of an isolator and attenuator to ensure that the input power into the modulator is 0 dBm. The isolator prevents reflections

off the modulator from propagating into the circuit section. This eliminates any reflection dependency on the I and Q vectors.

The output of the modulator is run through a high gain power amplifier which drives the probe and matching network. For our 10 GHz measurements, the variable phase shifter matching approach has been discontinued and a simple 3 dB series attenuator has been inserted to decrease the driving return loss of the cable by 6 dB. At 10 GHz there is enough loss in the cable that the input impedance is not far from 50 Ohms.

On the circuit side, a splitter has been inserted to provide a trigger signal for a repetitive sampling oscilloscope. To prevent reflections from the DUT (Device Under Test) a combination of attenuators and amplifier have been added. This provides approximately 12 dBm of available power with over 50 dB of isolation. This allows us to drive an open circuit and matched load without seeing any effects in the probe circuitry.

### 6.3 10 GHz calibration of the I/Q Modulator

Before any measurements can be made, it is necessary to characterize the modulator performance at 10 GHz. This measurement involved disconnecting the HP amplifier from the probe and connected it directly into a repetitive sampling oscilloscope as shown in Fig. 6.2. An input power of 0 dBm was injected into the modulator.

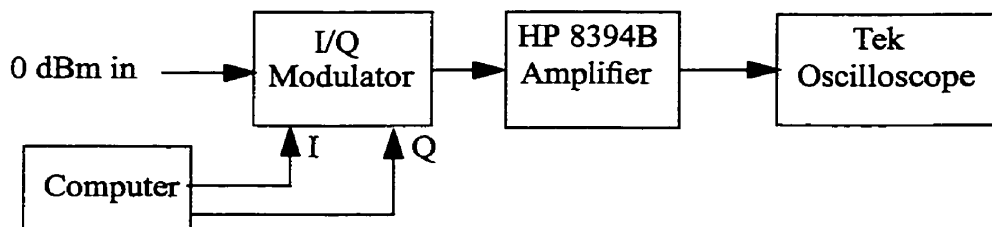


Fig. 6.2: I/Q modulator calibration configuration

The calibration consisted of varying the control word on both I and Q attenuator while the other was effectively turned off. The amplitude of the output RF signal was measured using a repetitive sampling oscilloscope. The control parameters used in the software were normalized floating point numbers where 1 represents no attenuation and 0 was maximum attenuation (turned off). Fig. 6.3 demonstrates the I and Q attenuator characteristics as a function of attenuation factor.

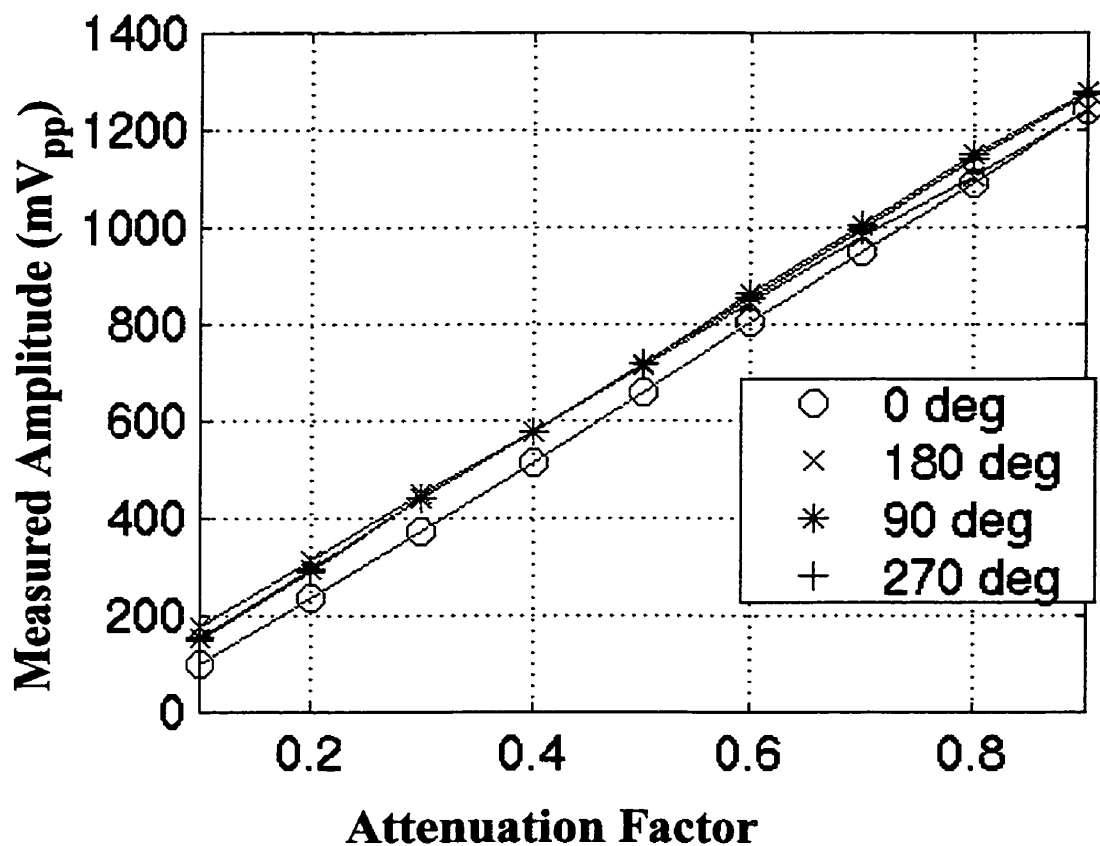


Fig. 6.3: I and Q attenuator characteristics

The measurement was made from 0.1 - 0.9 due to non-linearities in the modulator characteristic from LO leakage. It is apparent from Fig. 6.3 that the characteristics of each attenuator is quite different. This will introduce some errors between actual and software

computed phase. In the previous chapter, we had introduced a compensation block in the I/Q modulator driver which corrects for the differences in all four curves. This was done by modelling each characteristic by a linear equation. This is a reasonable assumption since all curves are linear due to the internal lookup tables in the device. Using the software, we can compute the desired I and Q components and pass these values through the inverse linear function to find the corrected I and Q parameter which in turn gets written to the I/Q modulator. This type of compensation was attempted and the corrected plot is shown in Fig. 6.4.

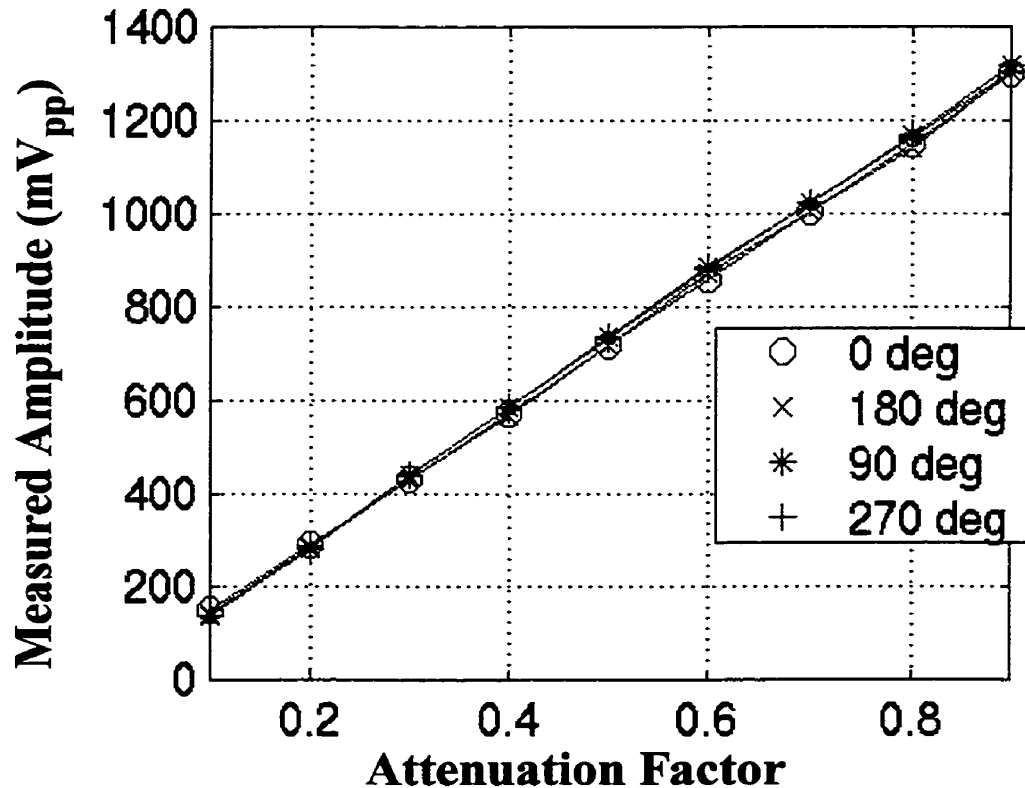


Fig. 6.4 : Compensated attenuator characteristics

It is apparent from the previous plot that the compensation did in fact work. We have achieved essentially the same characteristic on both the I and Q axis which suggests that the software computed amplitude and phase will be very close the actual ones.

### 6.4 Vector Voltage Measurements of a CPW at 10 GHz

10 GHz calibration measurements were performed on a small 50 Ohm CPW structure with an embedded 50 Ohm termination. This structure is more suitable for high frequency measurements since conductor sizes are much smaller to minimize capacitive coupling to the probe. The measurement structure is shown in Fig. 6.5.

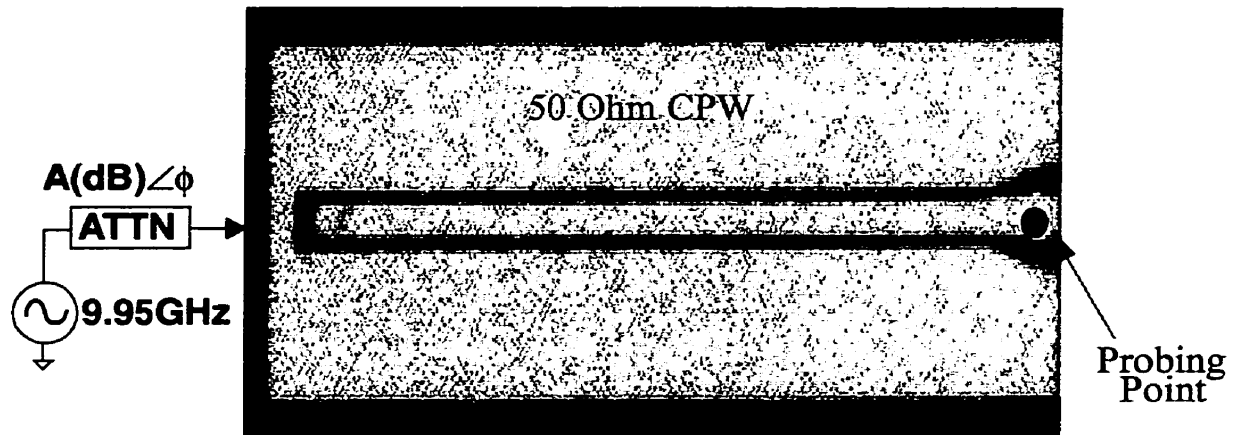
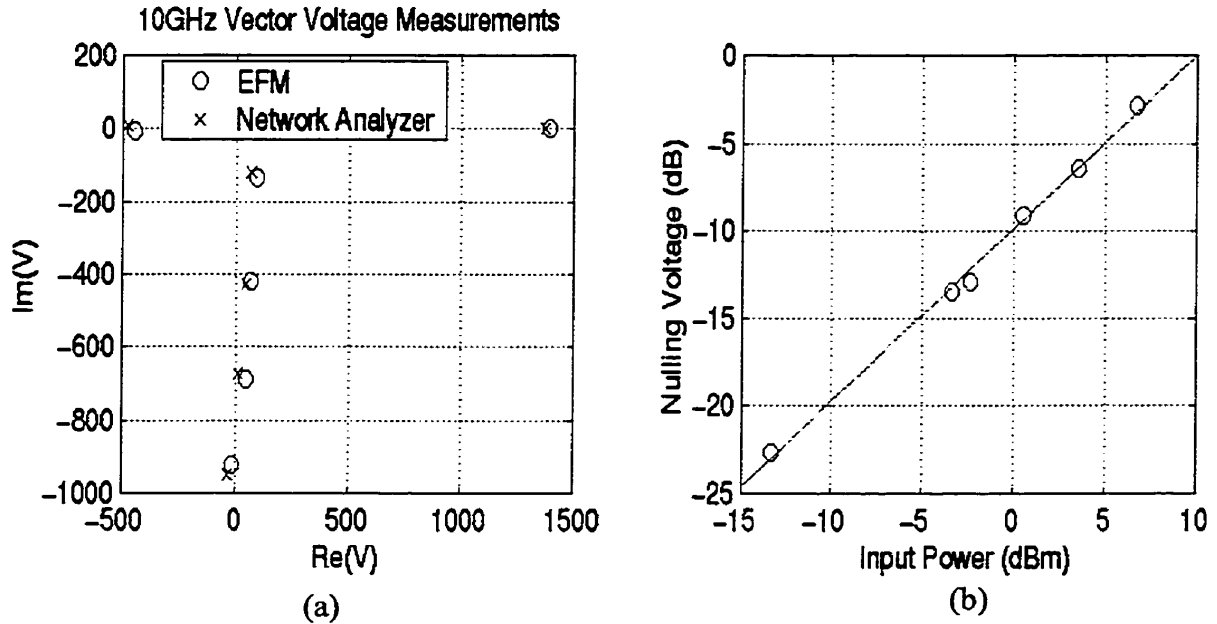


Fig. 6.5: Calibration CPW structure

The operating frequency was slightly less than 10 GHz due to the 9.95 GHz operation of the Nortel phase shifter that will be measured later on in the chapter. The signal was placed on the CPW using a coplanar on-wafer probe. The signal level was varied over a 20 dB dynamic range using a combination of attenuators which were accurately calibrated using a network analyzer. Fig. 6.6 demonstrates the EFM results in comparison to the network analyzer results.



**Fig. 6.6 :** (a) Vector measurements compared to network analyzer (b) Calibration curve

The measured amplitude and phase show close agreement with the calibrated values (Fig. 6.6(a)). This was done at different operating amplitude and phases which indicates that the I/Q modulator is properly compensated. Fig. 6.6(b) demonstrates the calibration curve. There is a linear relationship between the input power level (in dBm) and the normalized force nulling value which is expected from the mathematics presented earlier. The calibration curve provides some insight on the expected dynamic range of the instrument at 10 GHz. The maximum measurable signal being approximately 10 dBm which corresponds in linear scale to about  $2 V_{pp}$ . The minimum signal level depends highly on the noise levels. For probing unpassivated circuits, a typical sensitivity would be -17 dBm where for passivated circuits (assuming 1-2  $\mu\text{m}$  spacing), the sensitivity is in the area of -14 dBm. Either way, we still have a 20 dB dynamic range at this frequency.

### 6.5 Amplitude and Phase Profiling of Transmission Lines

The first circuit which was probed was a small CPW structure similar in geometry to the calibration standard used in the previous section. At 10 GHz, the amplitude and phase distribution along the line was profiled. The first structure consisted of a 13.5 mm long 50Ω CPW structure which was open-circuited at the load end as shown in Fig. 6.7.

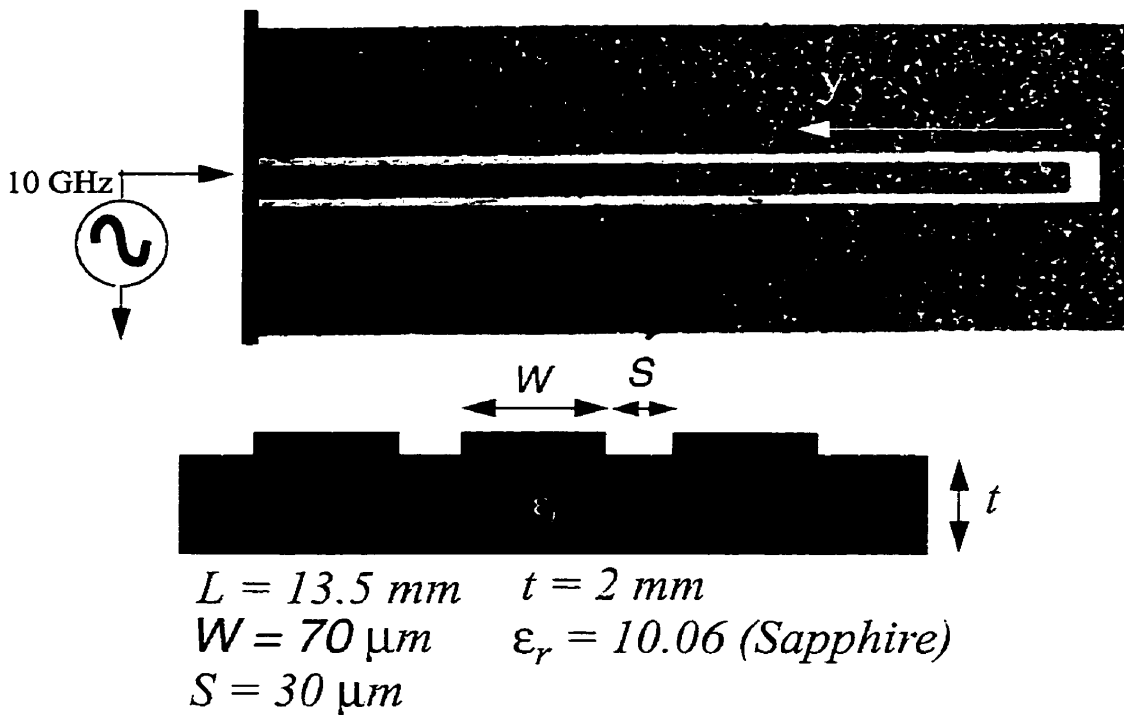


**Fig. 6.7:** Open-circuited 50 Ohm CPW structure

The signal was injected onto one end of the line using a coplanar on-wafer probe. The EFM probe's initial position was at the open-circuited end and moved towards the source with course 300 μm steps. At each point, the amplitude and phase was measured and plotted in Fig. 6.8.

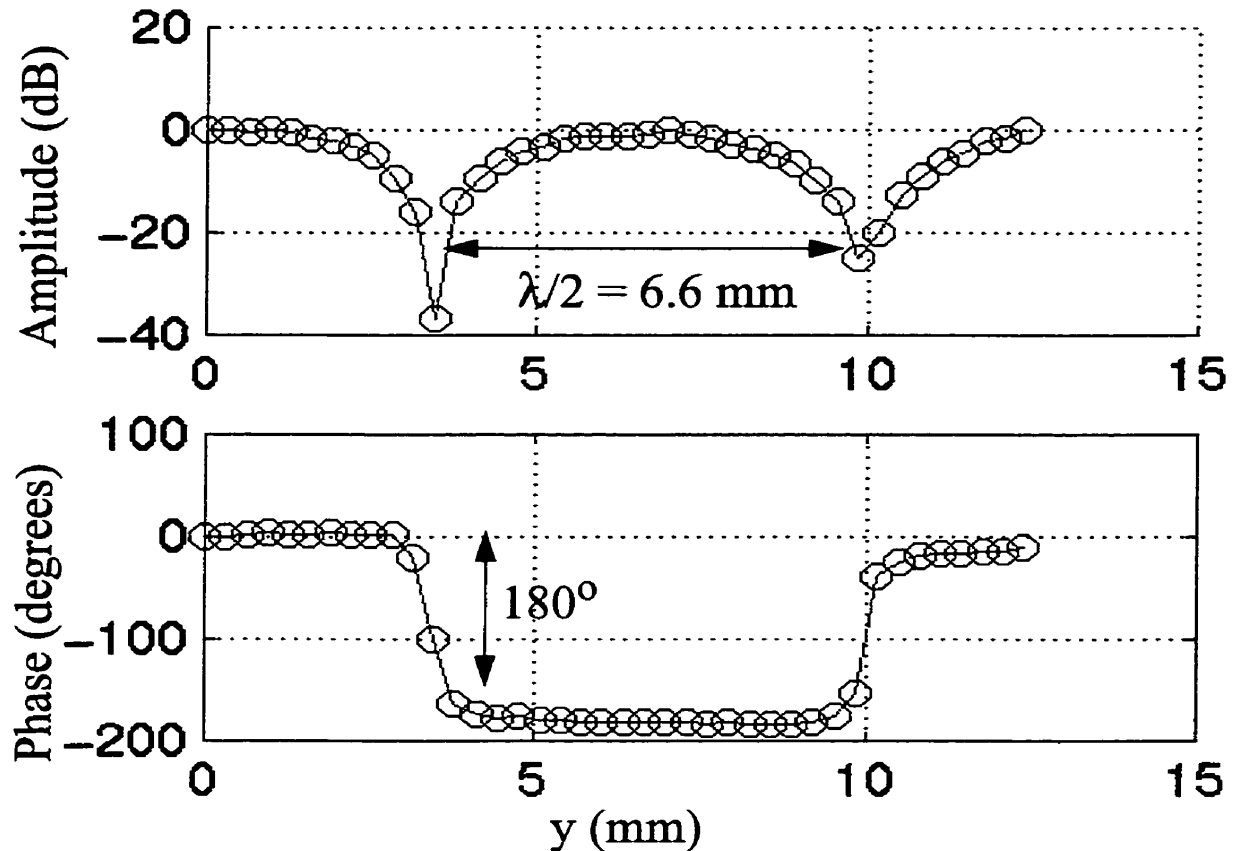


Fig. 6.8: Standing wave measurement of CPW

The measurement results suggest the presence of a standing wave which is expected on an open-circuited transmission line. Notice at the null points the phase shifts by  $180^\circ$  and remains very constant between these points as expected for a standing wave distribution. From transmission line theory we can use the measurement results to solve for the effective dielectric constant of the CPW by computing a wavelength of

$$\frac{\lambda}{2} = 6.6 \text{ mm} \quad \text{Therefore } \lambda = 13.2 \text{ mm}$$

With a wavelength of 13.2 mm, the calculated effective dielectric constant is

$$\lambda = \left(\frac{c}{f}\right) \frac{1}{\sqrt{\epsilon_{eff}}} \quad (6.1)$$

Solving for  $\epsilon_{eff}$ :

$$\epsilon_{eff} = \left(\frac{c}{f\lambda}\right)^2 = 5.1 \quad (6.2)$$

The validity of this number can be verified through simulation. Using the same conductor geometry specified in Fig. 6.7, the effective dielectric constant was simulated using the Lincalc software yielding a  $\epsilon_{eff}$  of 5.2. The simulation result seems to be in close agreement with the measured value. The simulation assumed a dielectric constant of 10.06 for Sapphire[33].

For purposes of repeatability, the effective dielectric constant was again measured using a different CPW structure with the same cross-sectional geometry but match terminated as shown in Fig. 6.9.

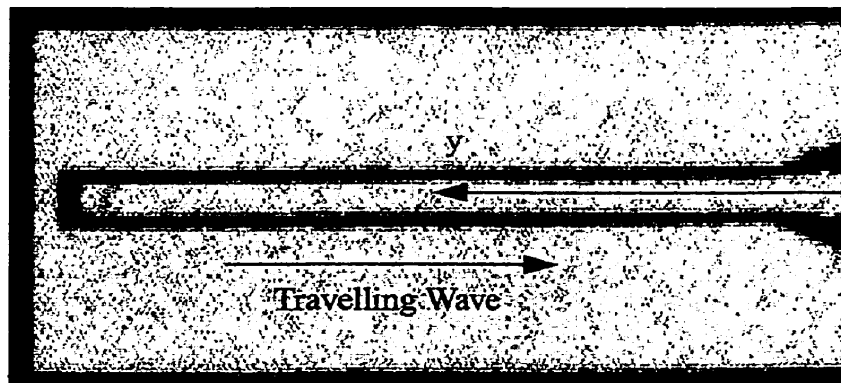


**Fig. 6.9:** Travelling wave line

In this case the expected voltage distribution would be that of a travelling wave where the dielectric properties can be deduced by the phase characteristic along the line. As

before, the probe started from the load end and moved towards the source recording only the phase as shown in Fig. 6.10.

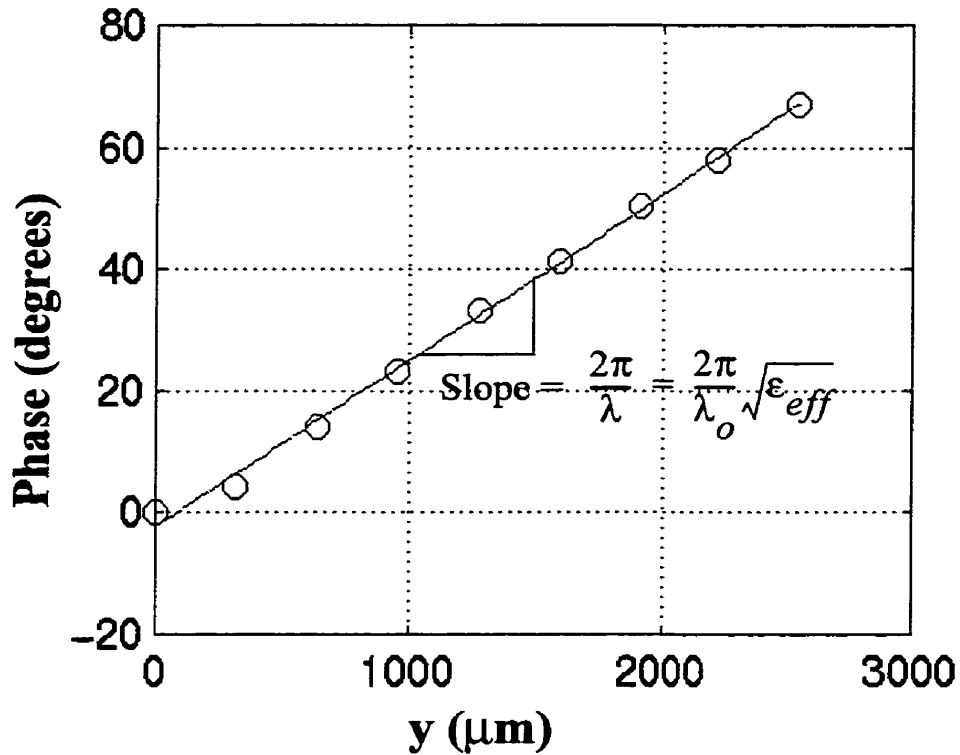


Fig. 6.10: Phase distribution along travelling wave line

As expected from a travelling wave line, the phase is a linear function of position. Again using transmission line theory we can estimate the effective dielectric constant from the slope of the line. The measured results are

$$\text{slope} = 474.73 \text{ rads/m} = \frac{2\pi}{\lambda_0} \sqrt{\epsilon_{eff}} \quad (6.2)$$

$$\text{Solving for } \epsilon_{eff}: \quad \epsilon_{eff} = 5.13$$

This number is also in close agreement with the simulated and previously measured values. These numbers makes sense if we consider a CPW structure with air( $\epsilon_r = 1$ ) on top

and sapphire ( $\epsilon_T \approx 10$ ) on the bottom where the effective dielectric constant should be near the average of the two.

### 6.6 Measurement of a 10 GHz Phase shifter

In this section, 10 GHz measurements on a Nortel phase shifter will be presented. The circuit has 5 identical analog phase shifter sections along with a coarse digital shifter followed by output buffers and limiters. A microphotograph of the circuit along with a sample probe point is shown in Fig. 6.11.

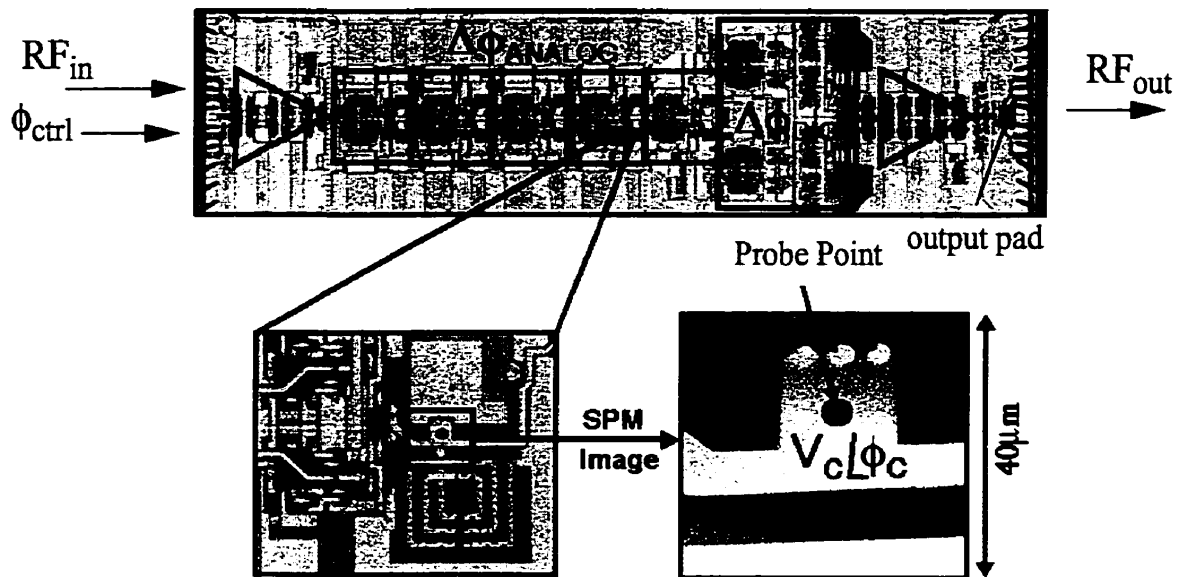


Fig. 6.11: Nortel phase shifter circuit

Measurements were made on the output of each analog phase shifter. The probing was performed on a via between a large capacitor and inductor as indicated in Fig. 6.11. The analog phase shift control voltage ( $\phi_{ctrl}$ ) was varied from -3 to 3 Volts and the relative phase was measured. The output phase was also measured on the output pad for comparison with the repetitive sampling oscilloscope measurements provided by Nortel and performed by us.

The measurement setup involved injecting a 300 mV<sub>pp</sub> input signal at 9.95 GHz. This frequency is necessary since the device utilizes a high Q bandpass filter at the front end. The output was terminated to 50 Ohms by a repetitive sampling oscilloscope. Fig. 6.12 demonstrates the measured phase characteristic at the output of each analog phase shifter section.

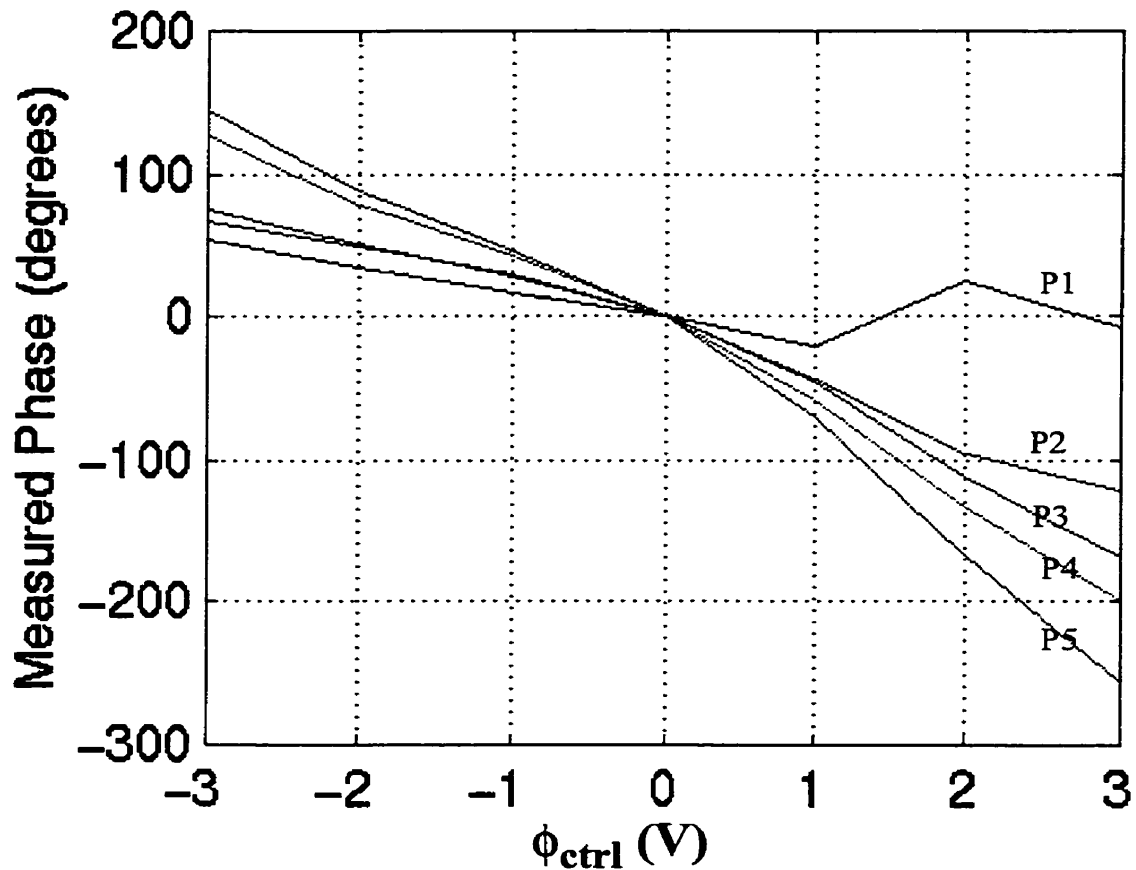


Fig. 6.12: Internal node phase measurements versus analog control voltage

From Fig. 6.12, we can see the cumulative contribution of all phase shifters measured from an internal node perspective. There are a few anomalies such as in the case of phase shifter 1(P1) where its characteristic is not monotonic. This may be explained by the substantial level of ground bounce measured in the circuit. This kind of measurement

will be discussed in more detail in the subsequent section dealing with the measurement of the Nortel wideband amplifier.

In Fig. 6.13, the phase characteristic was also measured on the output pad (100x100  $\mu\text{m}$ ) which compares well to the Nortel measured curve and the one measured using a repetitive sampling oscilloscope. The last phaseshifter (P5) also compares well to the other three measurements.

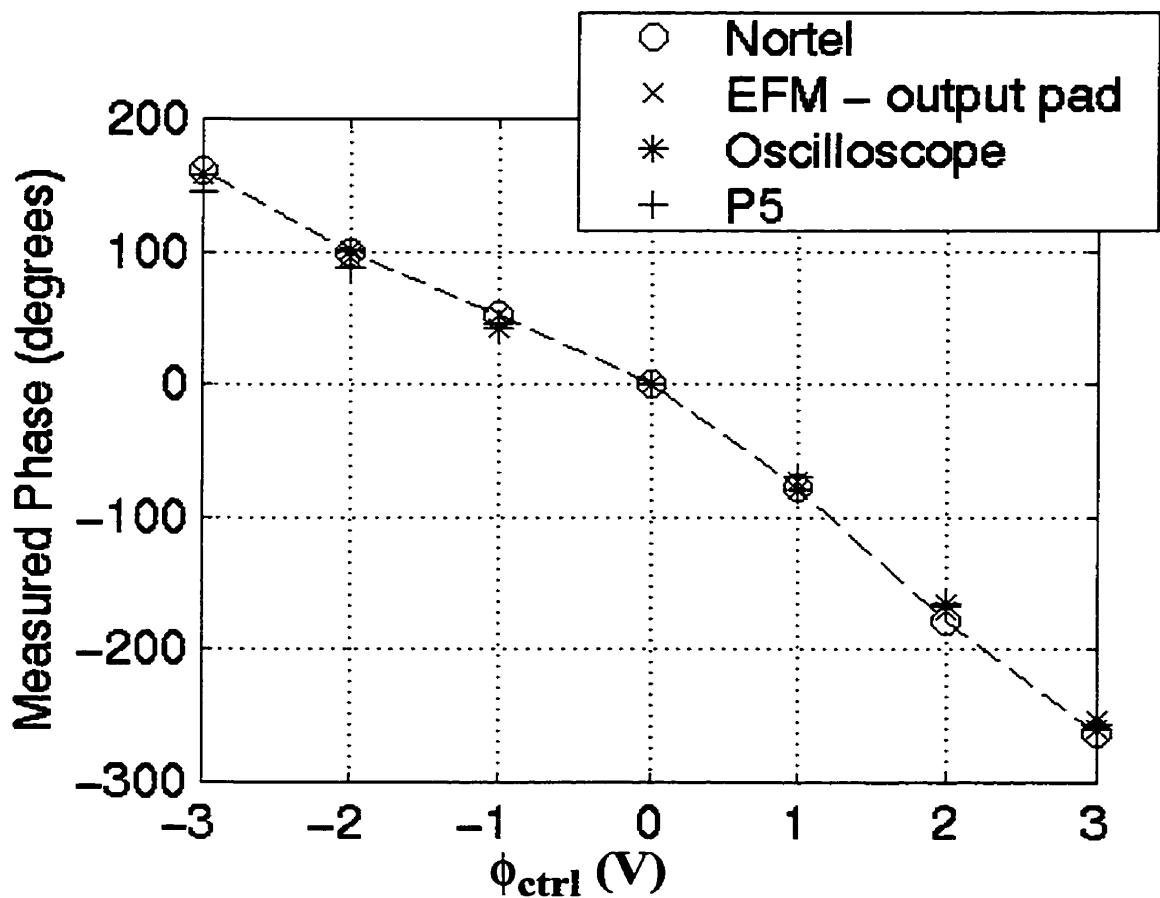


Fig. 6.13: Comparison curves using EFM, oscilloscope and Nortel measurements

### 6.7 Measurement of a Distributed Amplifier

Vector voltage measurements on a distributed amplifier provided by Nortel Networks were performed. The provided scattering parameters are indicated below in Fig. 6.14.

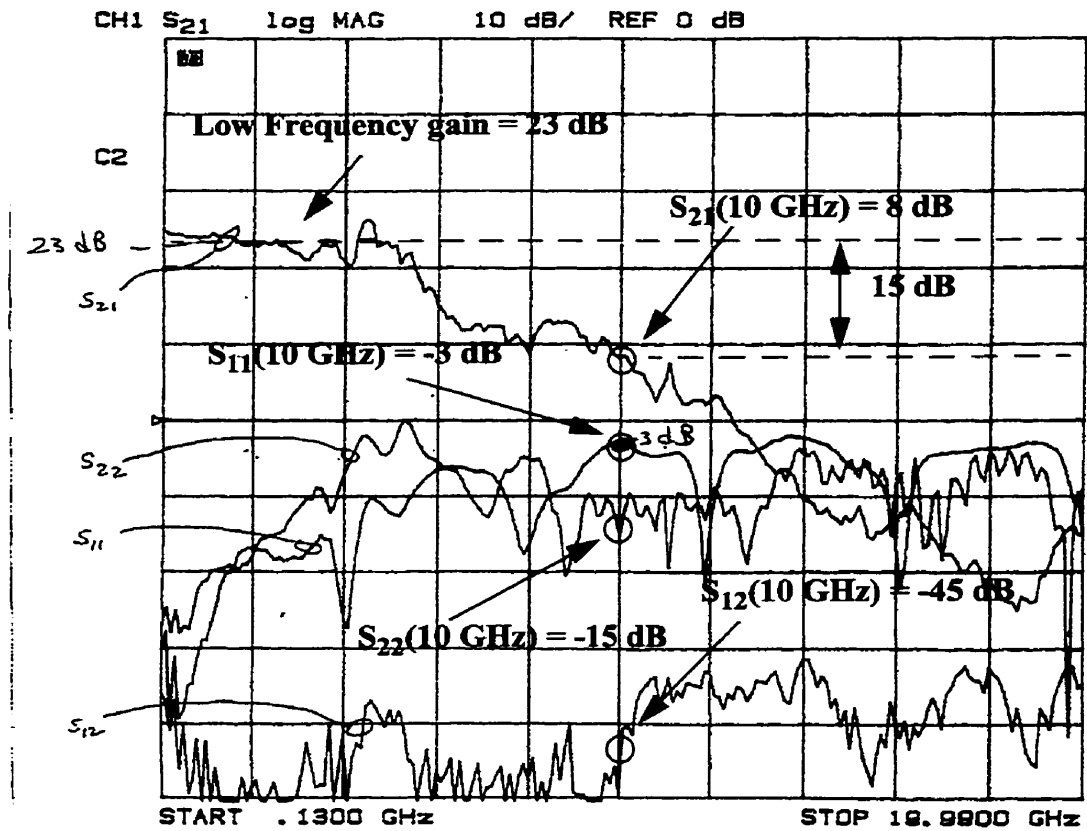
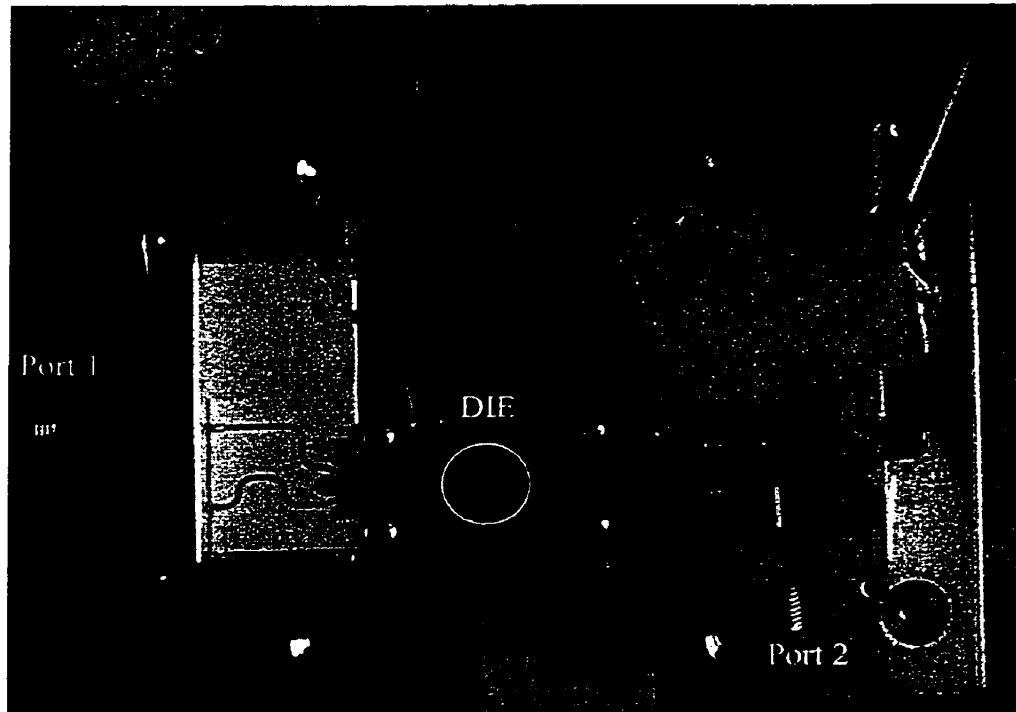


Fig. 6.14: Wideband amplifier scattering parameters [provided by Nortel]

The amplifier has a low frequency gain of 23 dB over an approximate 4 GHz bandwidth. Measurements were made at 10 GHz where amplifier performance has degraded considerably. A photograph of the die and packaging is shown in Fig. 6.15.



**Fig. 6.15:** Nortel amplifier packaging

The measurement setup involved injecting -8.6 dBm of input power into the terminal port 1. The device was characterized using a network analyzer which yielded the following S-Parameters at 10 GHz. The values below compare well with those in Fig. 6.14, except for  $S_{22}$ .

**Network Analyzer**

$$S_{11} = -2.9 \text{ dB}$$

$$S_{21} = 8.1 \text{ dB}$$

$$S_{12} = -49 \text{ dB}$$

$$S_{22} = -3.0 \text{ dB}$$

**Power Meter**

$$S_{21} = 8.3 \text{ dB}$$

The insertion gain was also measured using a power meter and compares well with the network analyzer measurement. To provide some insight on the amount of gain degrada-

tion, the measured  $S_{21}$  at 1 GHz was roughly 23 dB. At 10 GHz the gain has dropped by roughly 15 dB. The input and output matching is also very poor at this frequency. A microphotograph of the circuit layout is shown in Fig. 6.16.

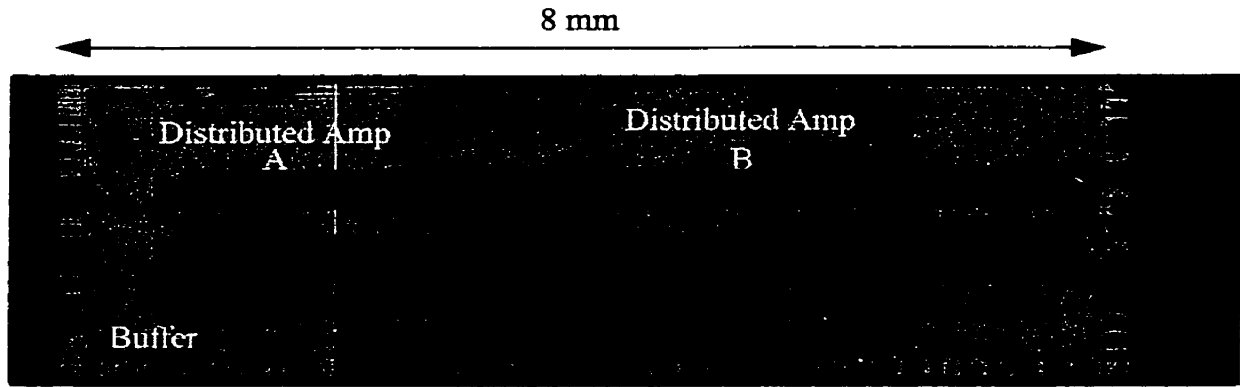


**Fig. 6.16:** Microphotograph of amplifier layout

The circuit contains an input buffer followed by two distributed amplifiers. Several measurements were made on this circuit including a VSWR measurement of the input transmission line, amplitude and phase measurements on the  $V_{EE}$  power rail, loss measurement of the output transmission line and internal node measurements at the terminal ports of both distributed amplifiers.

### **6.7.1 VSWR Measurement**

As mentioned in the previous section, the input return loss is very poor at roughly -3 dB( $S_{11}$ ). Using the EFM instrument it is possible to measure the VSWR by observing the standing wave distribution along the feed line inside the fixture as shown in Fig. 6.17. This type of measurement becomes quite feasible at this frequency since the wavelength is only about 3 cm. A half wavelength section is suitable to find at least one maximum and minimum.

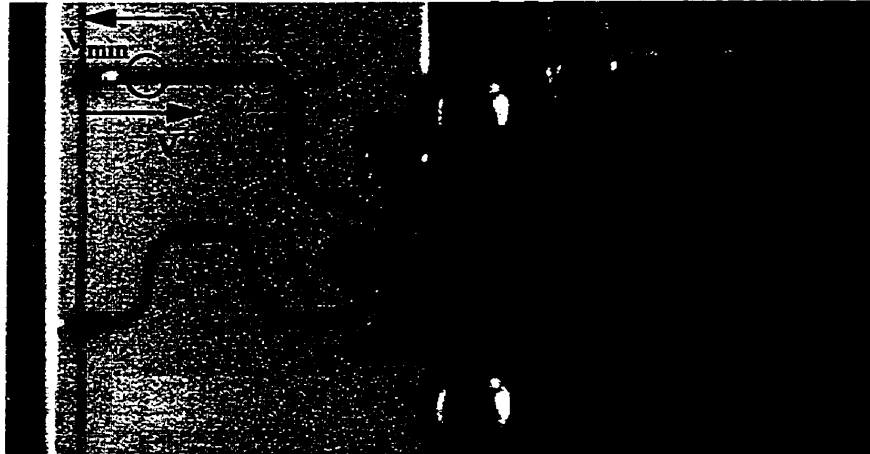


**Fig. 6.17:** Input 50 Ohm transmission line feeding amplifier input pad

The EFM probe was scanned along the line while measuring the amplitude of the signal. A local maximum and minimum were determined at the locations shown Fig. 6.17. Taking the ratio of the amplitude null points(A) and assuming proportional to voltage, the estimated VSWR is

$$VSWR = \frac{V_{max}}{V_{min}} \approx \frac{A_{max}}{A_{min}} = \frac{0.22}{0.04} = 5.5 \quad (6.3)$$

Using this result, the estimated magnitude of the input reflection coefficient( $S_{11}$ ) is

$$|S_{11}| \approx \frac{VSWR - 1}{VSWR + 1} \approx -3.2dB \quad (6.4)$$

The estimated return loss is within 0.3 dB from the one measured using the network analyzer.

These results can also be used to estimate the magnitude of the input power wave into the amplifier neglecting transmission line loss.

$$A^{incident} = \frac{A_{max}}{1 + |S_{11}|} \quad (6.5)$$

$$A^{incident} = 0.130 \Rightarrow 270 \text{ mV}_{pp} \text{ (from calibration curve)} = -7.4 \text{ dBm}$$

$$\text{Estimated incident power (EFM)} = -7.4 \text{ dBm}$$

$$\text{Measured incident power (Power Meter)} = -8.6 \text{ dBm}$$

The estimated power deviates by 1.2 dB from the measured incident power. This may be explained by the fact that losses have not been included during the VSWR calculation and all calculations were assuming the line was 50 Ohms which may not be completely true at this frequency.

### ***6.7.2 Transmission Line Effects on Power/Ground Metal***

In integrated circuits, ground and power rail signals can severely degrade the performance of the device. In dense CMOS digital circuits, most power and ground rails are considered capacitive or low impedance due to close proximity to the lossy grounding substrate (image effect). In microwave circuits, ground and power lines can appear more inductive since they are often spaced farther away from the package ground especially in GaAs where the substrate is insulating. Grounding to the package ground plane is usually done through wirebonds on specified ground pads. A major problem arises when these conductor sizes become comparable to a wavelength where transmission line effects dominate as shown in Fig. 6.18.

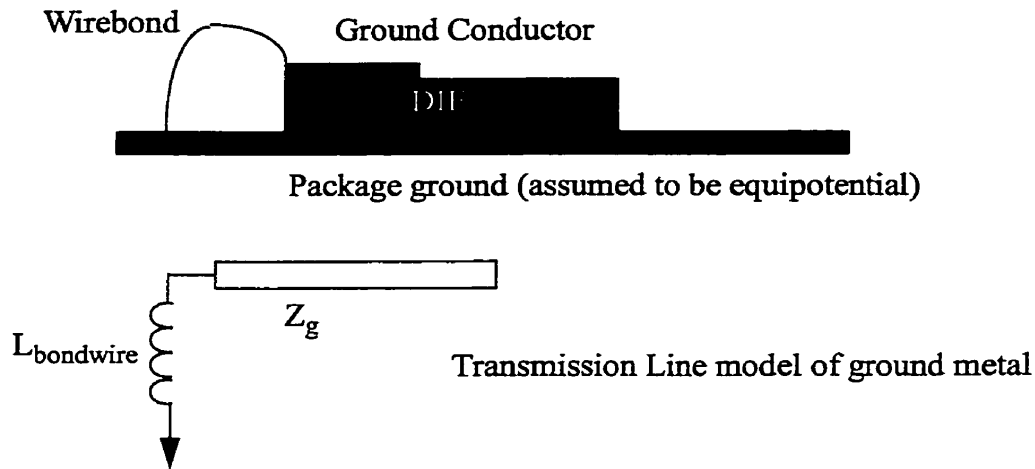


**Fig. 6.18:** *Ground conductor models at high frequency*

The termination of the line is typically modelled using an inductance representing the grounding bond wire. In most designs the ground metal is made as wide as possible to minimize series inductance so that the line looks like a low impedance transmission line. This is adequate for low frequencies, but even a low impedance short circuited line will resonate at a quarter wavelength giving a very high input impedance as suggested using eqn. 6.6 assuming a perfect short circuit at the wirebond location.

$$Z_{ground} = jZ_g \tan(\phi) \quad (6.6)$$

At  $\phi = 90^\circ$  (quarter wavelength)

$$Z_{ground} = \infty \text{ (open circuit)}$$

Unfortunately these effects are only dominant at high frequencies when it is extremely difficult to probe. The EFM instrument provides a feasible solution for probing power and ground conductors and observing distributed effects without excessive loading.

The internal node measurements included profiling the signal on the power( $V_{EE}$ ) line as shown in Fig. 6.19.

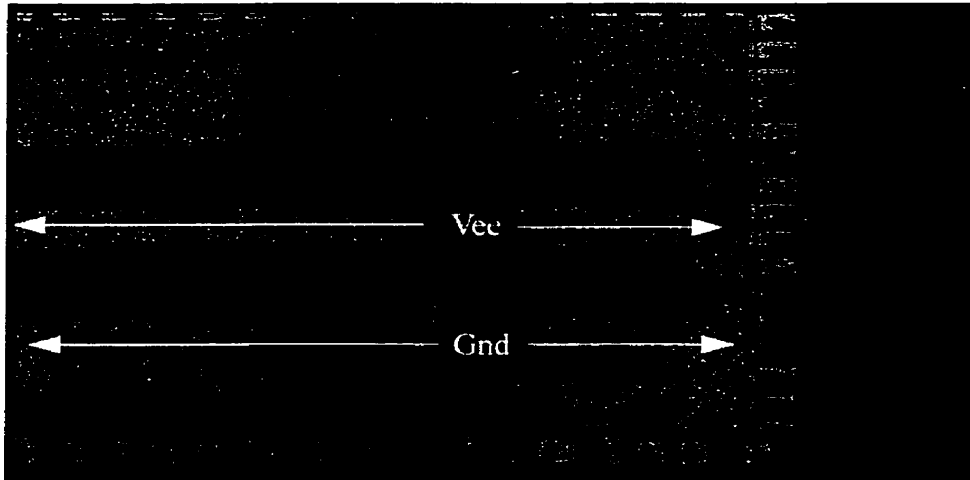


**Fig. 6.19:** Power and ground rails on die

Measurements were made along the  $V_{EE}$  line starting from the 5th cell from the end of the line. The probe was moved four cells for each measurement corresponding to roughly  $600\ \mu\text{m}$  per movement over a total distance of 6 mm. The first three measurement points are shown in Fig. 6.20.

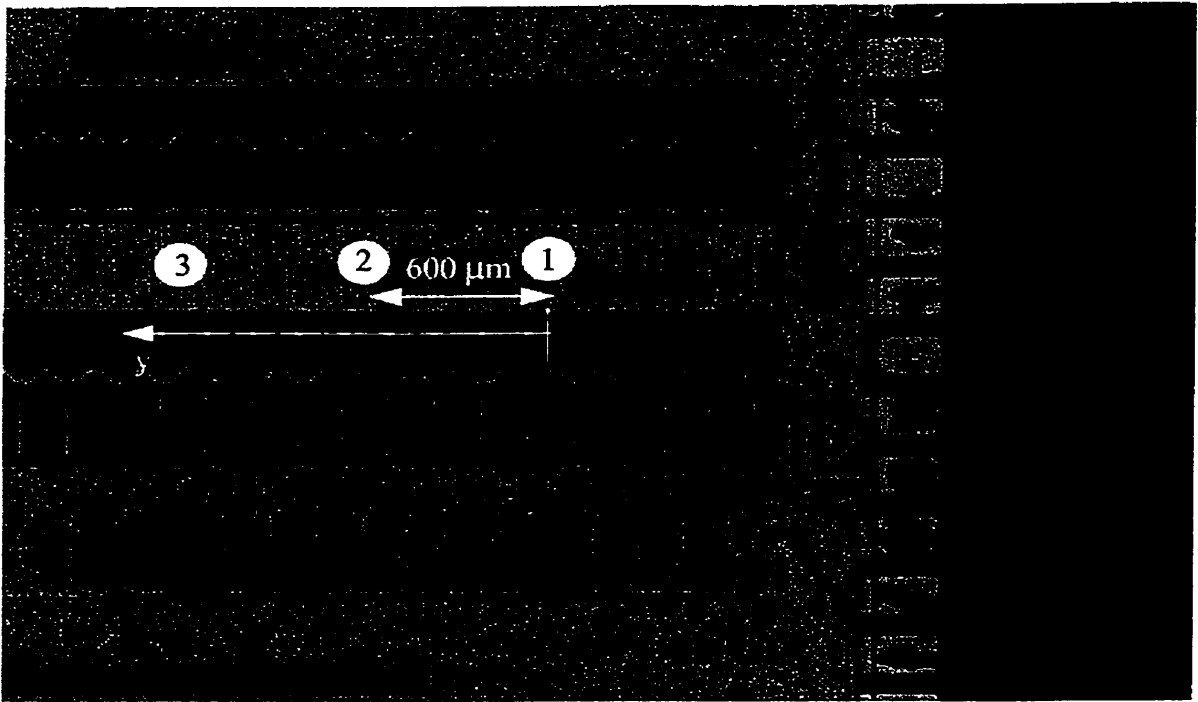


**Fig. 6.20:**  $V_{EE}$  rail along with first three measurement points

The conductors were quite large and covered the entire cantilever during the measurement. This suggests that coupling to other conductors could be minimized therefore adequate spatial resolution is achieved. The  $V_{EE}$  line is connected to the power supply via eight pads on the left side of the die (Fig. 6.16). It runs directly down the center providing the necessary biasing for each amplifier block along the distributed amplifier. It is grounded at the right side via a MIM capacitor to the ground plane. Assuming the  $V_{EE}$  line width is roughly  $300\ \mu\text{m}$  with a GaAs substrate thickness of  $200\ \mu\text{m}$ , we can estimate the characteristic impedance of the line which yields roughly  $33\ \Omega$ . On a GaAs substrate at 10 GHz, a full wavelength would be roughly 10 mm, meaning that the  $V_{EE}$  line is slightly larger than a half wavelength.

Fig. 6.21 demonstrates the measured amplitude and phase along the  $V_{EE}$  line with a phase reference at the first measurement point.

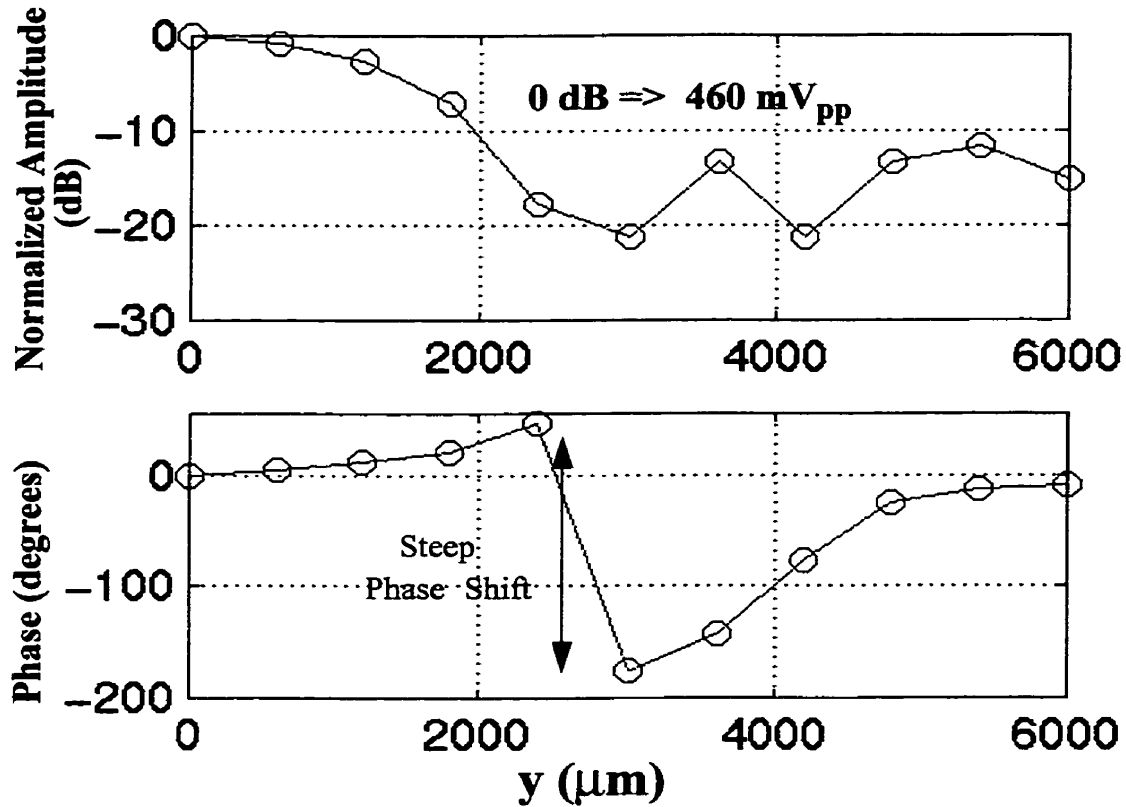


Fig. 6.21: Amplitude and phase distribution along  $V_{EE}$  line

The characteristic does seem to have a standing wave characteristic. Notice at the midpoint (3 mm), the voltage reaches a null ( $< -20$  dB) and the phase does a radical phase shift of  $230^\circ$ . It is unlikely the observed behavior is due to signals coupling through the active circuitry since there is very high isolation on the biasing transistors. A more plausible explanation would be to consider the  $V_{EE}$  and signal lines as coupled line structures. This is possible since the coupled lines are in fact larger than half a wavelength meaning that coupled line resonances may occur which seems to be the case in Fig. 6.16. At a sim-

ulation standpoint, the last few amplifier stages are seeing a  $460 \text{ mV}_{\text{pp}}$  signal on the  $V_{\text{EE}}$  line which will severely disrupt the biasing control on the amplifier.

### 6.7.3 Insertion Loss Measurement of Output T-Line

In this section, the insertion loss of the output transmission line was measured to obtain a more realistic estimation of the gain of the amplifier at 10 GHz. Fig. 6.22 shows the output transmission line and connector.

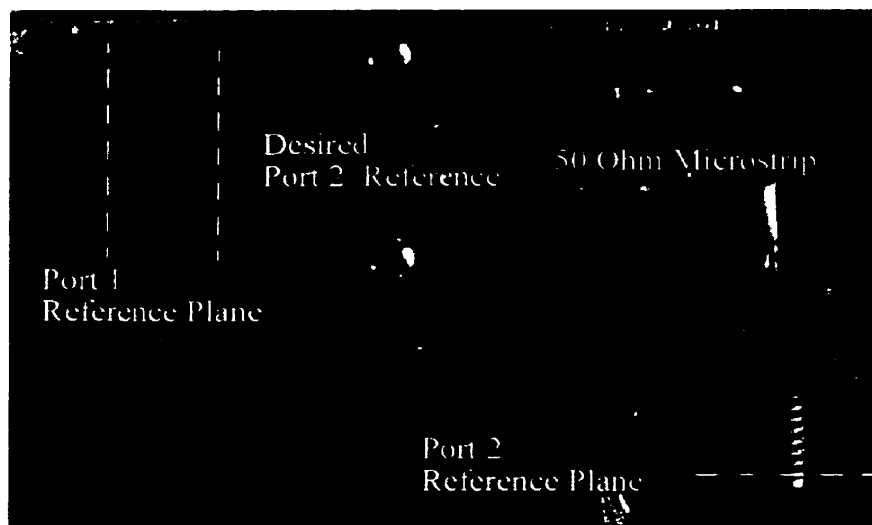


**Fig. 6.22:** Nortel amplifier output transmission line

Measurement of the input T-line loss is very difficult, so we will assume that loss is negligible and reference port 1 in Fig. 6.22 is identical to the input connector reference plane. The output line loss can be extracted by measuring the signal on the output line near the bondwire and measuring the signal after it passes through the output connector. This was achieved by using a small coaxial cable with a small notch cut in the grounding shield. The cable had an approximate loss of  $-0.5 \text{ dB}$  at 10 GHz which was factored out of the measurement. The measurement point on the output T-line is shown in Fig. 6.23.

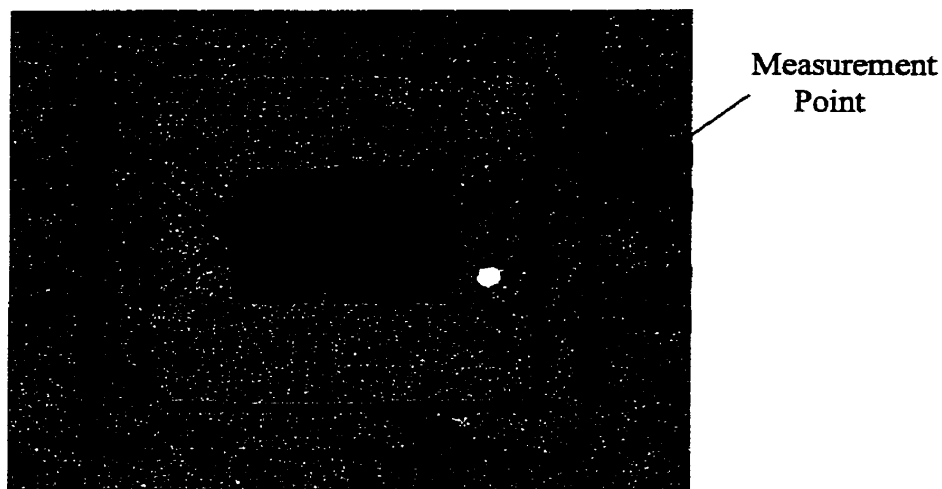


**Fig. 6.23:** Nortel amplifier along with connecting transmission lines

The measurement results yielded the following voltage levels:

$$\begin{aligned} V(\text{T-line}) &= 1.03 V_{pp} \\ V(\text{output connector}) &= 777 \text{ mV}_{pp} \end{aligned}$$

Using the measured values, the loss of the output line can be estimated to be

$$Loss = \frac{V_{output}}{V_{Tline}} = -2.4 \text{ dB} \quad (6.7)$$

Neglecting loss on the input line, the insertion gain of the amplifier at 10 GHz is more realistically 10.5 dB rather than the measured 8.1 dB in Fig. 6.14. Incorporating the losses on the input line as well will mean that the actual  $S_{21}$  will be larger than 10.5 dB.

### 6.7.4 Internal Node Measurements of Distributed Amplifiers

Internal node measurements were made at the terminal ports of both distributed amplifiers as shown in Fig. 6.24. The input signal to the buffer was -8.6 dBm as mentioned before.

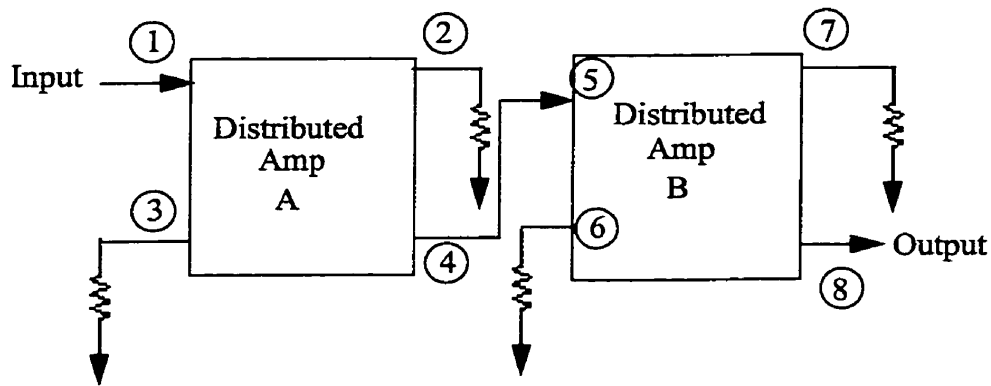


**Fig. 6.24:** Cascaded distributed amplifiers and probe locations

The measurement results are tabulated below in Table 6.1.

Node	V(mV <sub>pp</sub> )
1	232∠0°
2	308∠-47°
3	138∠-75°
4	270∠-115°
5	326∠-178°
6	534∠32°
7	685∠-23°
8	1040∠-119°

**Table 6.1:** Internal node measurements at 10 GHz

Using this data we can estimate the gain of the cascaded distributed amplifier to be roughly 13 dB. The measured gain ( $S_{21}$ ) of the amplifier accounting for the output transmission line loss is about 10.5 dB. The 2.5 dB discrepancy may be the result of attenuation in the input buffer circuitry, losses on the input transmission line and mismatch on the input port. Voltage levels on the input of the buffer could not be probed due to close proximity to the input bondwires.

The on-die output voltage measurement of  $1.04 V_{pp}$  (node 8 in Table 6.1) is very close to the  $1.03 V_{pp}$  measured on the output transmission line in section 6.7.3. The discrepancy may be the result of the bondwire inductance and coupling effects (spatial resolution) of the probe inside the circuit.

The effects of signals on the  $V_{EE}$  line may be used to explain the unusual signal variations along the distributed amplifiers. Anomalies occur between node pairs (1,2) and (5,7) where the signal levels are being amplified. This seems initially strange since it occurs on the input transmission lines where amplification should not occur. You would expect a lossy travelling wave behavior along the input line. This odd behavior was later confirmed by Nortel Networks.

## **6.8 Summary**

The I/Q modulation technique appears to be successful. The standing and travelling wave measurements are in close agreement to the theoretical mathematical equations which proves the accuracy of the phase and amplitude measurements. Non-invasive internal node measurements at 10 GHz were performed on the Nortel phase shifter and amplifier. The non-contact nature of the instrument allows for observing transmission line effects on ground and power supply metal which is often the cause of failure in many high

frequency designs. In the next chapter, we will investigate the invasiveness of the instrument.

## Chapter 7: Invasiveness

### 7.1 Invasiveness Model

Invasiveness is very important in assessing the performance of any probing instrument. Invasiveness is defined through the amount of circuit loading. Often a probing instrument may have high bandwidth but may be too invasive for internal node probing. A typical parasitic model for a probe is shown in Fig. 7.1.

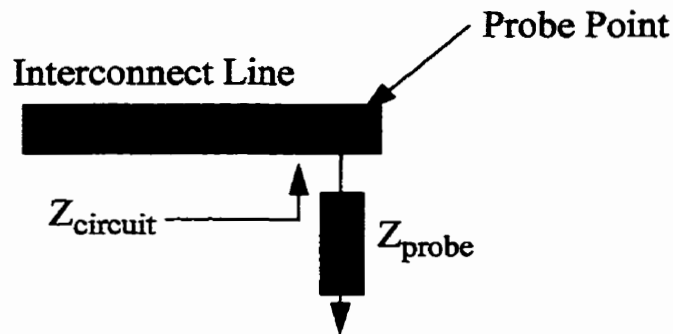


Fig. 7.1: Invasiveness model

The loading effect can be quantified by the amount of deviation between the measured signal and the unloaded signal. Using linear circuit theory we can estimate this in terms of probe and circuit impedances using

$$\frac{V_{measured}}{V_{unloaded}} = \frac{Z_{probe}}{Z_{circuit} + Z_{probe}} \quad (7.1)$$

For probing input and output ports of microwave circuits, the invasiveness is usually quite small for most probes. This is mainly because of the low input impedance of 50 or 25 Ohms. Unfortunately internal nodes often do not operate at low base impedance since

from node to node, the input impedance can vary substantially. The internal nodes of high gain amplifiers will often have much larger input impedances between stages therefore more susceptible to loading. The problem becomes worse at higher frequency due to a decrease in loading impedance. A probing instrument must have a very high loading impedance to be useful for probing internal nodes of microwave integrated circuits. In typical contact probes, the loading impedance may vary from small in matched impedance probes to quite high in active probes. In active probes the loading is dominated by the gate capacitance of the input transistor.

## 7.2 Invasiveness in EFM

Due to the non-contact nature of the instrument, the probe loading impedance is dominantly capacitive limited by the coupling capacitance,  $C_p(x,y,z)$ , between the probe and measurement conductor. A low frequency equivalent circuit model is demonstrated in Fig. 7.2. The appropriate model and values can vary depending on the probe-circuit geometries.

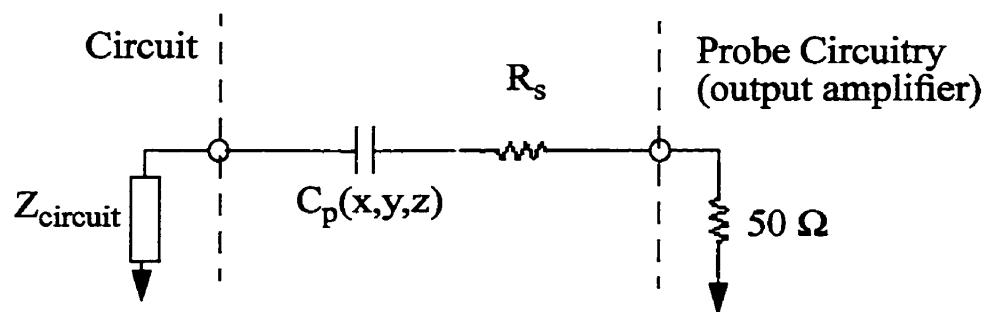


Fig. 7.2: Equivalent circuit model

A series resistance has been added to model the resistance between the silicon block and the mounting 50 Ohm transmission line. This resistance will be neglected in this chap-

ter. In the subsequent sections we will attempt to estimate the coupling capacitance as compared to simulation.

### 7.3 Simulation of Loading Capacitance

The non-contact nature EFM makes the coupling capacitance a very important component in assessing the overall invasiveness. Simulation have been done which model only the capacitive coupling to the probe tip. The plot in Fig. 7.3 demonstrates the loading capacitance between a typical EFM probe tip and a 1  $\mu\text{m}$  wide conductor as a function of lateral position for a 200 nm probe to circuit spacing. This demonstrates less than 1 fF of loading capacitance.

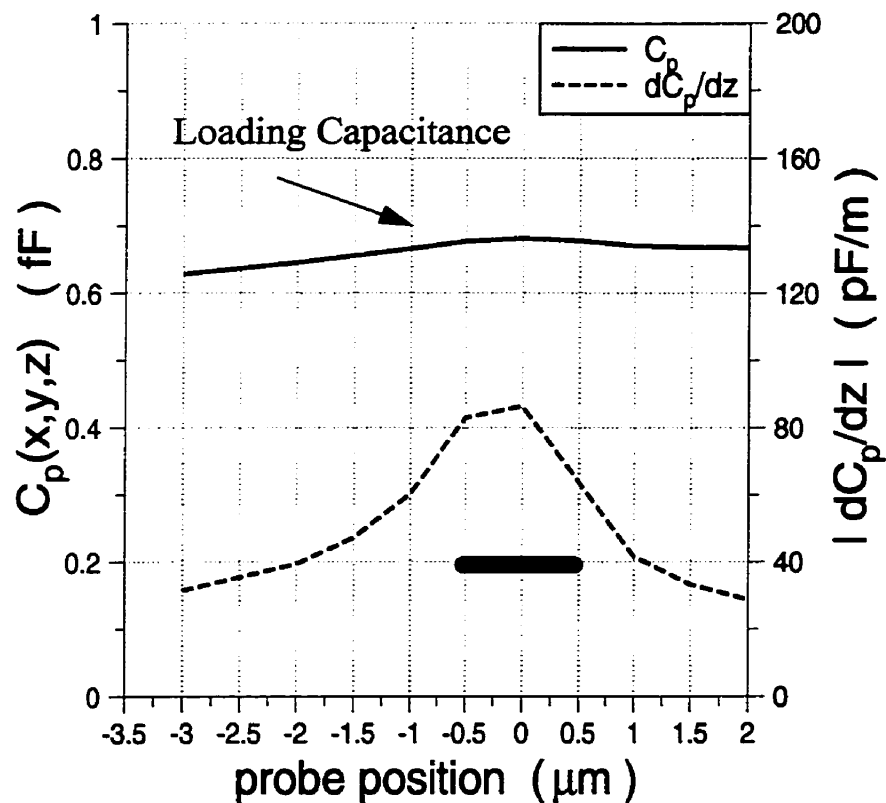


Fig. 7.3: Loading capacitance simulation results

Notice that there is less than 1 fF of loading capacitance even when the probe is position directly ovetop of the conductor (0.7 fF). Of course this number is very idealized because it only includes the parasitic effect of the probe tip. In reality, the tip is mounted on a large conductive beam which could add to the total capacitance depending on the circuit geometry and will be the focus of the next section.

#### 7.4 Probe Parasitic Capacitance

In the previous section, a 0.7 fF loading capacitance was simulated but in reality it could be many orders of magnitude worse due to other parasitics. There are three major sources of capacitance which include the tip, cantilever beam and mounting block as shown in Fig. 7.4.

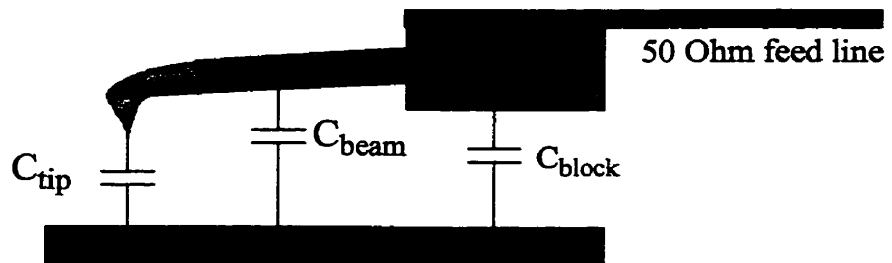


Fig. 7.4: Different sources of loading capacitance

The total capacitance will be given by the sum of all three and the dominance of any particular capacitance will vary with probing geometry. In probing MHIC (Microwave hybrid integrated circuit) where transmission lines are large in width (10's of  $\mu\text{m}$  to mm), the block capacitance will dominate. In RFIC probing where interconnects are smaller ( $\mu\text{m}$  to 10's of  $\mu\text{m}$ ) the effects of block capacitance are substantially smaller and the tip and beam capacitance will dominate. In the next few sections, we will attempt to measure

the equivalent capacitance on a large MHIC 50 Ohm microstrip and a small RFIC scale CPW.

### 7.5 Capacitance Estimation on a MHIC 50 Ohm Microstrip

An attempt was made to isolate all three sources of capacitance through measurement at three positions along the cross section of a 5 mm wide 50 Ohm microstrip as shown in Fig. 7.5. The measurement locations included: (1) entire block, cantilever beam and tip overtop the conductor, (2) probe tip and cantilever beam overtop the conductor and (3) only the probe tip overtop the conductor. In this measurement a NT-MDT CSCS12/W2C - type E tip was used[15].

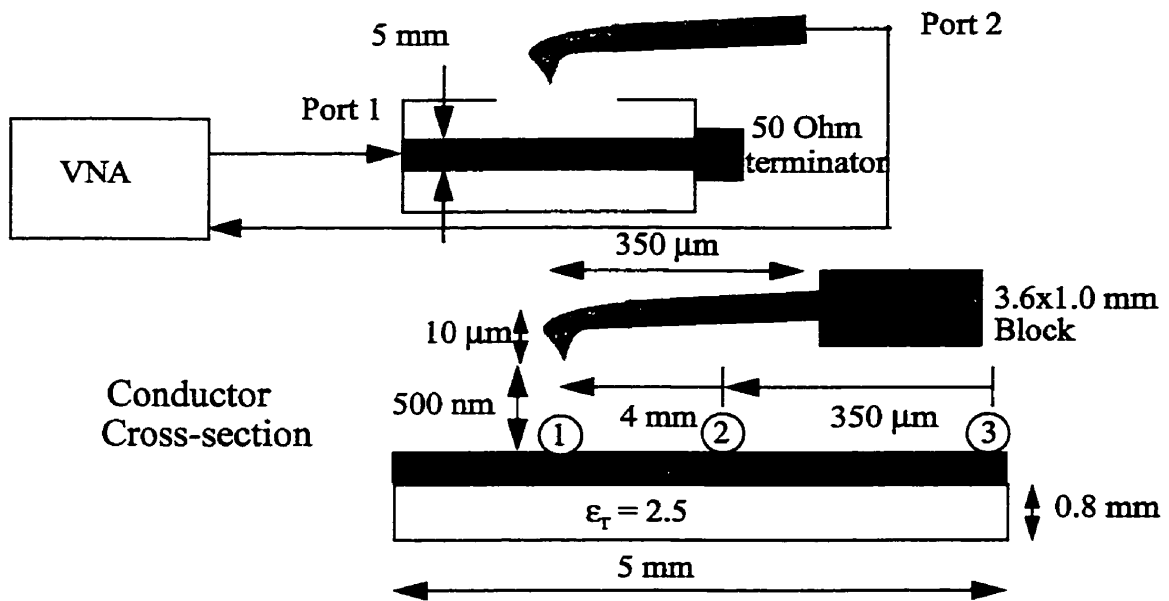


**Fig. 7.5: Coupling capacitance measurement setup**

The measurement was performed using a vector network analyzer defining the microstrip transmission line as port 1 and port 2 as the output of the probe. The insertion loss ( $S_{21}$ ) was measured to estimate the degree of coupling. A probe to circuit spacing of 500

nm was maintained using a z-axis positioning piezo. The first order high pass filter model shown previously in Fig. 7.2 will be used for comparison.

The insertion loss over a 6 GHz bandwidth in position #1 is shown in Fig. 7.6.

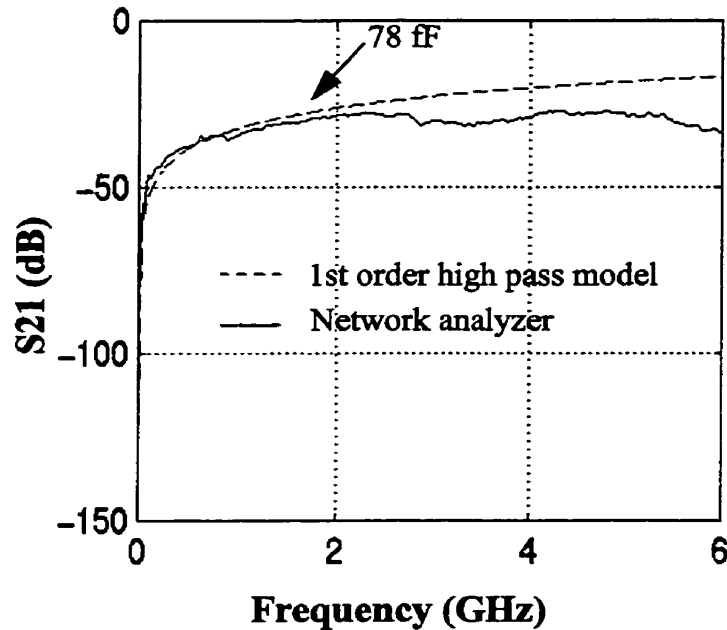
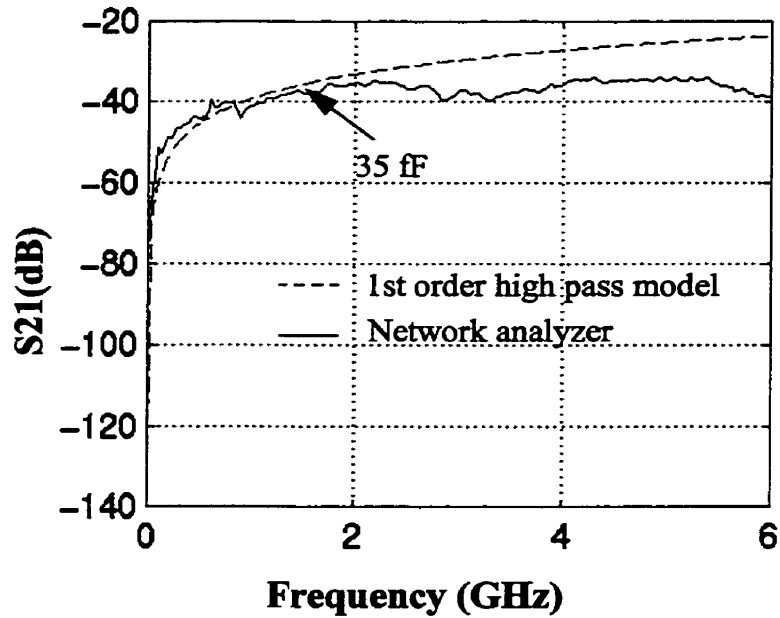


Fig. 7.6: Coupling characteristic at position #1

Notice that the high pass filter model presented in Fig. 7.6 is in agreement with the measured over the first 2 GHz. The deviation after 2 GHz may be the result of poor matching on the microstrip and mismatch on the probe PCB. From Fig. 7.6, the extracted low frequency capacitance is roughly 78 fF which is much larger than the original simulated 0.7 fF. The dominant source of coupling is the large cantilever block(3.6 x 1 mm) which is used for mounting the probe.

The next figure(Fig. 7.7) demonstrates the measurement at the second position including only the probe tip and cantilever beam overtop of the conductor.



**Fig. 7.7:** *Coupling characteristic at position #2*

The loading capacitance has dropped by more than 50% to 35 fF. There is still substantial coupling to the sidewall of the block in this position.

The last measurement was taken with only the tip of the probe overtop of the measurement conductor. The results are shown in Fig. 7.8, indicating a coupling capacitance of 20 fF. The measurement still includes a substantial contribution from the block sidewall capacitance.

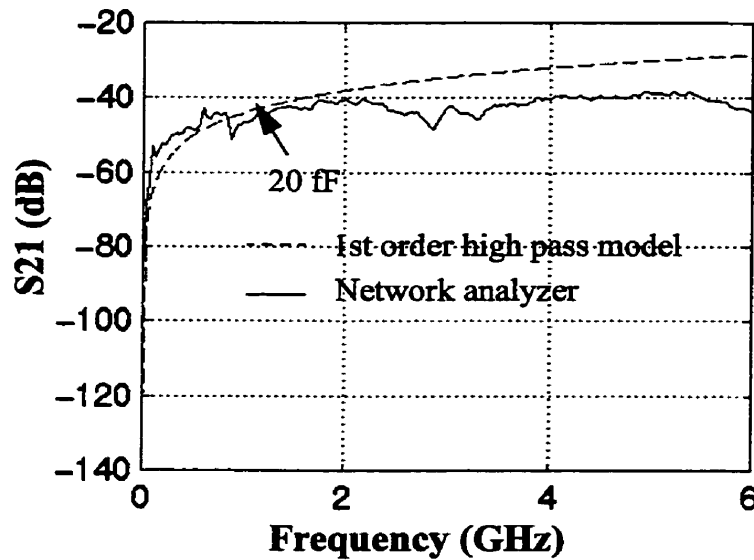


Fig. 7.8: Coupling characteristic at position #3

This measurement obviously does not consist of only the tip capacitance of 0.7 fF since there is still substantial coupling to the cantilever beam and block. It is quite easy to identify that the block capacitance is dominating by simply adjusting the probe to circuit spacing and monitoring the change in coupling. In position #3, the probe was moved from the initial 500 nm to 6  $\mu\text{m}$ , with negligible change in coupling. If the tip capacitance was dominating, a significant coupling change would have been observed.

A loading capacitance of 78 fF is still adequate for 1-10 GHz measurements on microwave hybrid transmission lines but will start to exhibit loading effects above 10 GHz. At 16 GHz, the capacitive reactance is 128 Ohms which is not too far from the 50 Ohm system impedance. Measurement of the tip capacitance must be done through the use of smaller conductor geometries that suppress the block coupling.

## 7.6 Capacitance Estimation using Small CPW Structures

In this section, a more accurate estimation of the tip capacitance will be made by using the calibration CPW structure seen in the previous chapter. Similar to section 7.5, three measurements were made as shown in Fig. 7.9.

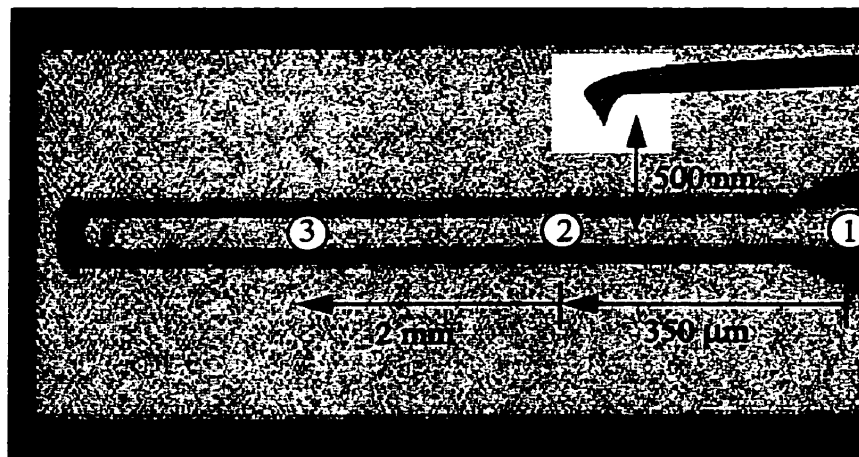


**Fig. 7.9:** Loading capacitance measurement using a CPW structure

The measurement was performed at 6 GHz to enhance the amount of coupled signal above the noise floor of the instrumentation. A 6 GHz signal was injected onto the line using a matched impedance on-wafer probe and the output of the EFM probe was connected to a repetitive sampling oscilloscope. The probe was placed 500 nm above the unpassivated line. Using the first order high pass model, the loading capacitance can be estimated by the coupled signal amplitude as indicated in Table 7.1.

Position	Coupling (%)	$C_p$
1	0.41	2.1 fF
2	0.60	3.07 fF
3	0.78	4.1 fF

**Table 7.1:** Capacitance measurements on a CPW structure

In this case, the loading capacitance has decreased significantly to a few femtoferads. This is much smaller than for most contact probes which can add around 40-100 fF of loading capacitance. In this case, the equivalent capacitance is dominated by the tip and cantilever beam and is much closer to the simulated 0.7 fF. It is important to note that the measurement was made very close to the noise floor of the oscilloscope which could incur a possible 50% error in the results.

### 7.7 Capacitance Estimation using Coupled Line Resonator

The measurement of capacitance in the femtoferad range is often very difficult using conventional network analyzers or oscilloscopes. In this section, a coupled line resonator will be used as a capacitance sensor to measure the loading capacitance. The coupled line resonator is indicated below in Fig. 7.10.

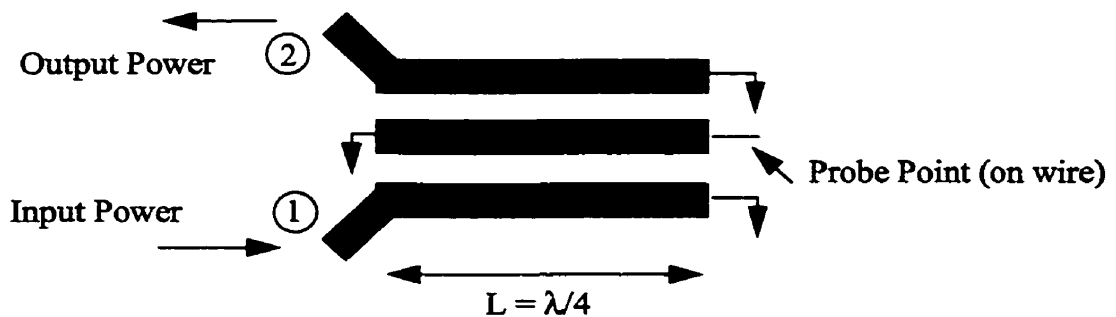


**Fig. 7.10:** Coupled line resonator

A small diameter wire was added to the end to minimize the capacitance contribution of the mounting silicon block. In this resonator, a capacitive load will change the phase of the reflected wave which results in a change in the resonant frequency. The shift in resonance can be measured using a network analyzer. The measurement yielded a loading capacitance of approximately 14 fF for a 200 nm probe to circuit spacing. Unfortunately there is still coupling to the cantilever beam and block making it difficult to measure the tip capacitance in this manner.

### ***7.8 Summary***

In this chapter we have attempted to measure the loading capacitance of the EFM probe. In probing transmission lines on hybrid microwave circuits, the loading capacitance can be as large as 80 fF due to the large conductive probe block. At 10 GHz this corresponds to roughly 200 Ohms which is still quite high for probing most 50 Ohm systems. For measurements above 20 GHz, the loading effect would become too large. Fortunately while probing inside RFICs where geometries are reduced, the amount of loading capacitance may be several femtoferads which will allow for non-invasive internal node measurements well into the millimeter wave region.

## Chapter 8: Spatial Resolution

### 8.1 Definition of Spatial Resolution in EFM

In the previous sections we have discussed invasiveness in the context of EFM. This concept deals primarily with the coupling capacitance of the probe to the measurement conductor. In assessing spatial resolution, the operative parameter is the coupling capacitance gradient[34] as given by the probe deflection

$$\Delta z|_{fr} = \frac{1}{2} \frac{Q}{k} K(A - V_c \cos(\phi_p - \phi_c)) \frac{\partial C_p}{\partial z} \quad (8.1)$$

Since the deflection is proportional to capacitance gradient, then the spatial resolution will be defined by the steepness of the gradient profile as a function of lateral movement. A numerical simulation of the gradient profile of a probe tip located 200 nm above a 1  $\mu\text{m}$  wide conductor is shown in Fig. 8.1.

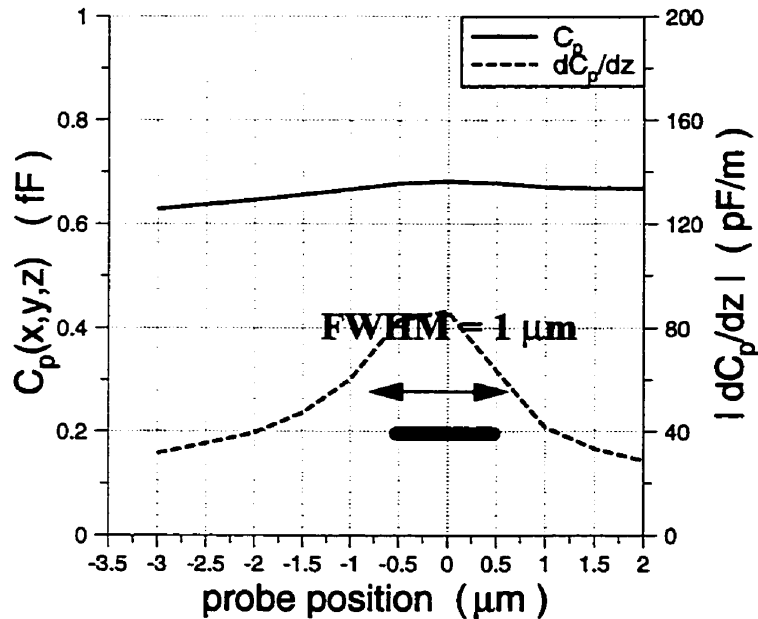


**Fig. 8.1:** Capacitance gradient simulation overtop a 1  $\mu\text{m}$  wide conductor

From the above graph, the capacitance derivative rolls off much steeper than the capacitance does. We can estimate the spatial resolution by measuring the FWHM (Full Width Half Max) of the derivative profile which is about 1  $\mu\text{m}$ . Keep in mind that this simulation only includes the probe tip and not the whole cantilever which will degrade the resolution. This will be studied in the next section.

In probing RFICs, mechanical crosstalk from other conductors will manifest itself in terms of parasitic capacitance derivatives not parasitic capacitance as in circuit level crosstalk. Let us consider the following model of a typical probe point shown in Fig. 8.2.

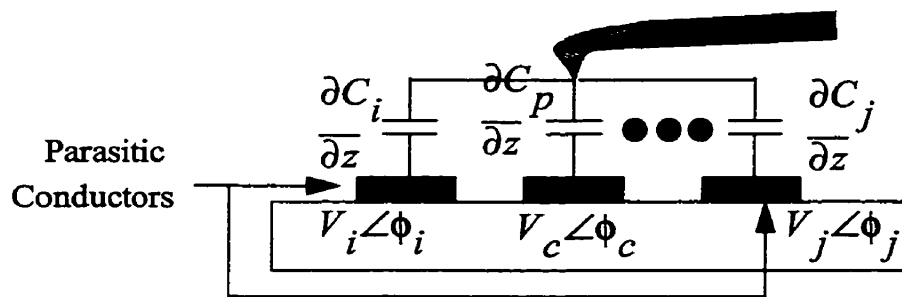


Fig. 8.2: Typical parasitic probing environment

If we neglect the conductor interaction with the beam, we can express the measured deflection using

$$\Delta z|_{f_r} \propto \frac{\partial C}{\partial z}^P (A - V_c \cos(\phi_p - \phi_c)) + \sum_{k=1}^N \frac{\partial C}{\partial z}^k (A - V_k \cos(\phi_p - \phi_k)) \quad (8.2)$$

↑
↑
↑
↑

Desired Signal
Crosstalk Signal  

(N = # of parasitic conductors)

If the effects of crosstalk are significant, both the phase and amplitude nulling will be affected. The measured phase will be determined by averaging the null points satisfying

$$F = \frac{\partial C}{\partial z}^P V_c \cos(\phi_p - \phi_c) + \sum_{k=1}^N \frac{\partial C}{\partial z}^k V_k \cos(\phi_p - \phi_k) = 0 \quad (8.3)$$

The corresponding amplitude null will be solved using

$$A = \frac{\max(F)}{\frac{\partial C}{\partial z}^P + \sum_{k=1}^N \frac{\partial C}{\partial z}^k} \quad (8.4)$$

## 8.2 Generalized Spatial Resolution in EFM

In the previous section, we have shown that the spatial resolution is approximately 1  $\mu\text{m}$  which included only the probe tip. In reality there are other parasitics which makes the actual spatial resolution of the instrument much worse than 1  $\mu\text{m}$ . In the analysis in the last section, it was assumed the only source of coupling was the tip of the probe. This is not completely true, due to the presence of the large cantilever beam shown in Fig. 8.3, conductors can easily couple to this structure causing the beam to deflect.

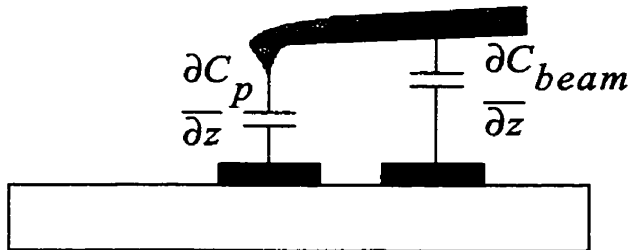


Fig. 8.3 : Electrostatic interaction with the cantilever beam

The whole beam is not susceptible to forces due to increasing mechanical isolation as one moves towards the pivot point. The most sensitive region is near the tip, within the

first quarter length of the beam. We can refine the mathematics to include the effects of the beam which is a very difficult problem since the beam itself is distributive, with an effective spring constant that varies with position. We can express the net deflection using the following general form similar to eqn. 8.2 as

$$\Delta z|_{f_r} \propto F_P (A - V_c \cos(\phi_P - \phi_c)) + \sum_{k=1}^N F_k (A - V_k \cos(\phi_P - \phi_k)) \quad (8.5)$$

Each deflection term is given a specific positive weight ( $F_k$ ) which is a complex function of spring constant, capacitance derivative and location of parasitic conductor in respect to the cantilever beam. Analytical computation of these weights are quite difficult and beyond the scope of this research. Fortunately the relative sizes of these weights can be estimated experimentally. In microwave circuits, signal lines are not as densely packed like in most digital circuits with a common conductor configuration that would include a signal line surrounded by ground and power supply metal as in CPW structures. We will assume the dominant form of parasitic coupling will be from DC potential carrying conductors, as shown in Fig. 8.4.

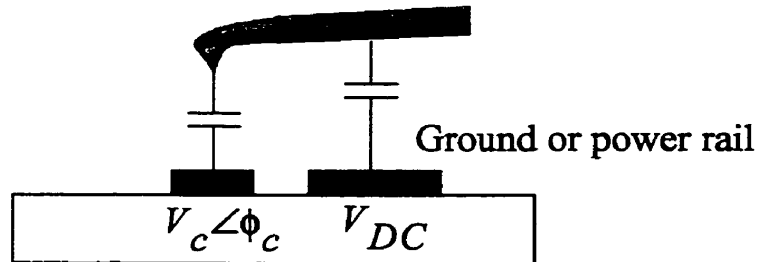


**Fig. 8.4:** Parasitic interaction with DC potential carrying conductors

We can relate our generalized deflection formula to accomodate parasitic conductors with dc potential using eqn. 8.5 with  $V_k = 0$  which yields

$$\Delta z|_{f_r} \propto F_p (A - V_c \cos(\phi_p - \phi_c)) + A \sum_{k=1}^N F_k \quad (8.6)$$

The above equation simplifies dramatically, with all parasitic deflection terms induced by the presence of modulation offset(A). This is very interesting because if we attempt to perform phase nulling, the equation simplifies to the following:

$$\begin{aligned} -F_p V_c \cos(\phi_p - \phi_c) &= 0 \\ \text{Measured Phase: } \phi_p &= \phi_c \end{aligned} \quad (8.7)$$

The interesting thing to note here is that in the presence of cross talk due to DC potentials, the measured phase is still correct. Unfortunately, the error will manifest itself in the measured amplitude as given by eqn. 8.6 with  $\phi_p = \phi_c$  as

$$\Delta z|_{f_r} = \left( F_p + \sum_{k=1}^N F_k \right) A - F_p V_c = 0 \quad (8.8)$$

Solving for A yields the amplitude null point

$$A = \frac{F_p V_c}{F_p + \sum_{k=1}^N F_k} \quad (8.9)$$

The parasitic DC conductors will decrease the effective measured amplitude between the range

$$0 \leq A \leq V_c \quad (8.10)$$

In the ideal case  $F_p \gg F_k$  we can use the limit

$$\lim_{F_k \rightarrow 0} \frac{F_p V_c}{F_p + \sum_{k=1}^N F_k} = V_c \quad (8.11)$$

The limiting case results in the null point converging to the amplitude of the desired RF signal. In the next section, we will attempt to look at a three conductor system and attempt to assess the relative magnitude of the weights in eqn. 8.6.

### 8.3 Amplitude and Phase Profile along Cross-Section of a CPW

In this section, a three conductor system of a CPW was used to investigate the relative sizes of the weights  $F_k$  in eqn. 8.6 as a function of probe position. Let us consider a three conductor system as shown in Fig. 8.5.

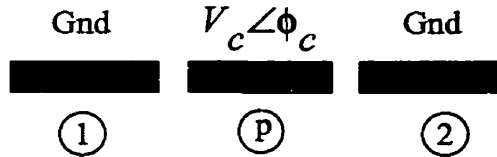


**Fig. 8.5:** CPW three conductor system

The necessary equations for a three conductor system are given using eqn. 8.7 and 8.9 as

$$\begin{aligned} \phi_m &= \phi_c \quad \text{For any probe position} \\ A_m &= \frac{F_p V_c}{F_p + F_1 + F_2} \end{aligned} \quad (8.12)$$

If the instrument has ideal spatial resolution, the amplitude and phase profile indicated in Fig. 8.6 should be measured, neglecting dielectric spacing between conductors.

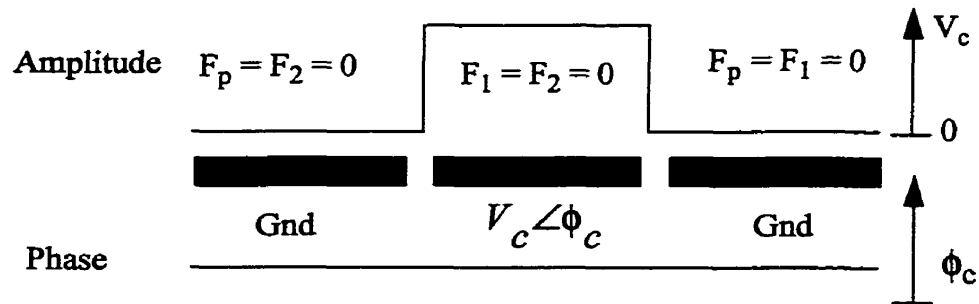


**Fig. 8.6:** Amplitude and phase profile for ideal spatial resolution

In practice, the measured amplitude and phase will not be so ideal since overtop each conductor, the other weights do not go to zero. An amplitude and phase scan was performed overtop a 50 Ohm CPW structure on a GaAs substrate. The structure has a  $10 \mu\text{m}$  wide center conductor and a  $9 \mu\text{m}$  ground spacing. The scan was performed at a  $25^\circ$  angle to facilitate the use of on-wafer probes to energize the center conductor as shown in Fig 8.7. All dimensions have been adjusted to account for the  $25^\circ$  angle.

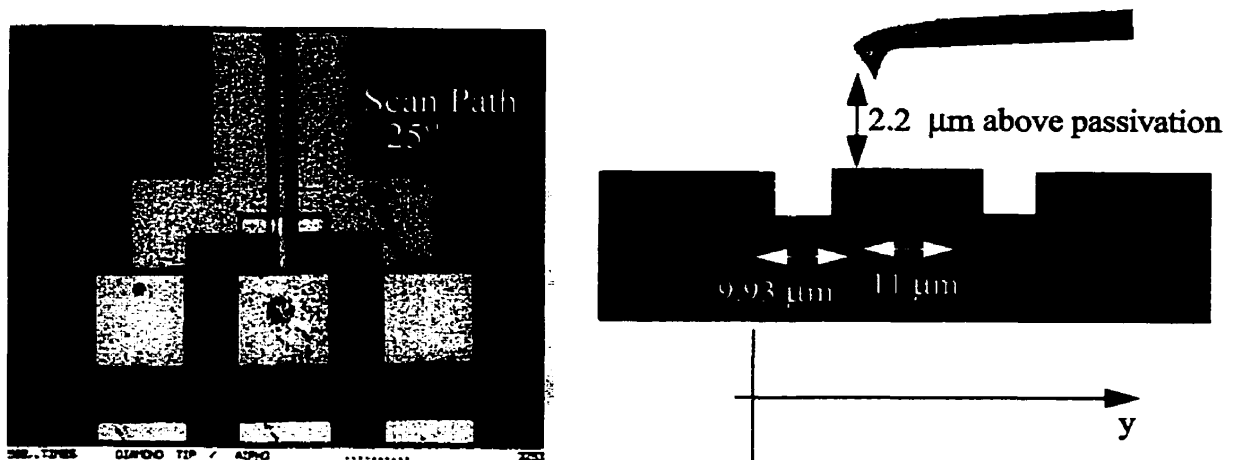


**Fig. 8.7:** GaAs CPW structure and cross-sectional view at a  $25^\circ$  angle

In the previous figure, all dimensions have been scaled to account for the  $25^\circ$  scan path. The scan started at the end of the first ground conductor and moved  $40\ \mu\text{m}$ , measuring the amplitude and phase at each point. The scanning was performed using piezo positioners which can perform  $1\ \mu\text{m}$  movements quite easily. During the measurement, a  $2.2\ \mu\text{m}$  probe to passivation spacing was maintained. The probe height was maintained by manually moving the z-axis piezo until the probe touches. At this point, the z-axis piezo is moved up  $2.2\ \mu\text{m}$ . The measurement results are shown next in Fig. 8.8.

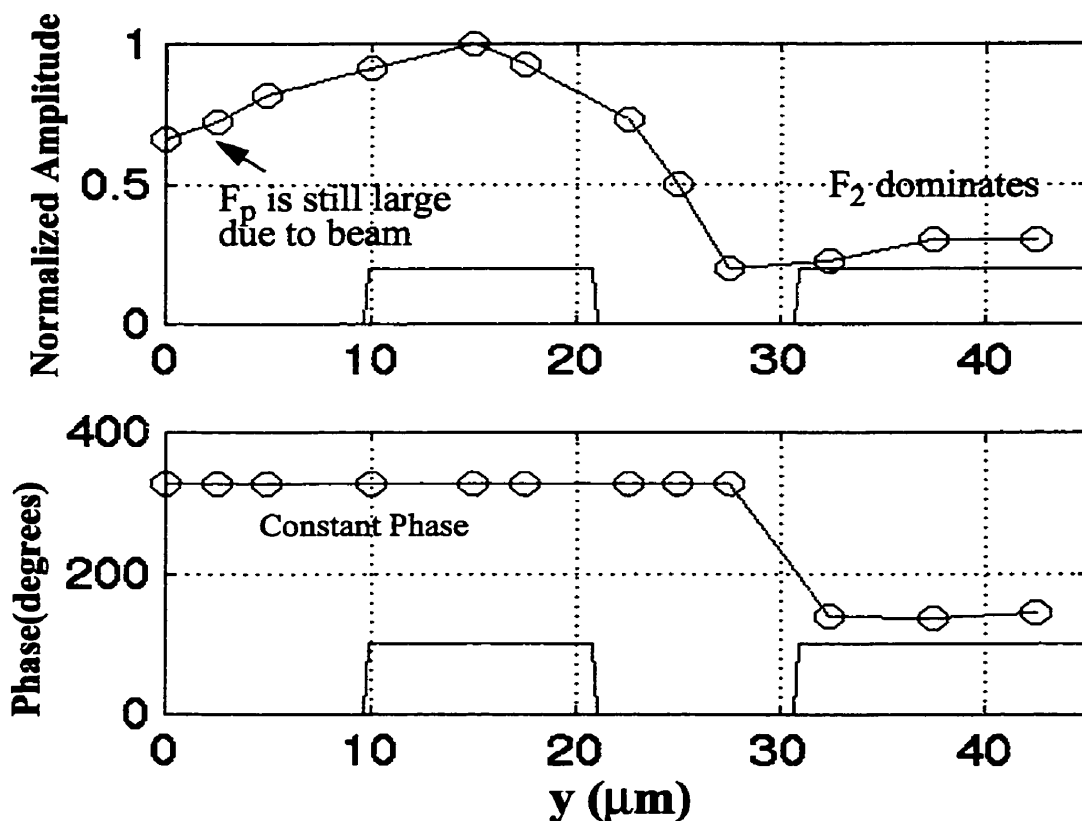


Fig. 8.8: Measured amplitude and phase profile versus probe position

From this plot, we can see the relative magnitudes of all three weights  $F_p$ ,  $F_1$ ,  $F_2$  as a function of position. As expected from eqn. 8.12, the measured phase remains constant even

while the amplitude varies. After  $30\ \mu\text{m}$ , a phase shift of  $180^\circ$  is encountered due to a small ground bounce signal. The measured amplitude varies significantly with position as expected from eqn. 8.12 where the lack of symmetry is explained by the large cantilever beam. At the beginning of the scan, the large beam is overtop the center conductor which enhances the  $F_p$  weight and increases the null point. On the other side of the center conductor, the measured amplitude drops off quite quickly as expected. Overtop the last ground plane results in a small signal corresponding to small ground bounce in the measurement circuit.

Attempting to quantify spatial resolution is quite difficult since it depends on conductor geometry and probe to circuit spacing. In the case of the small CPW structure with  $2.2\ \mu\text{m}$  spacing, the spatial resolution is probably between  $20\text{-}30\ \mu\text{m}$ . Probing an unpassivated version would produce a scan closer to the ideal demonstrated in Fig. 8.6.

#### ***8.4 Measured Amplitude Variation with Probe to Circuit Spacing***

Another way to assess the degree of parasitic coupling is to measure amplitude null point versus probe to circuit spacing. Using the same three conductor system and placing the probe tip overtop the middle of the center conductor, the probe height could be varied using the z-axis piezo as shown in Fig. 8.9.

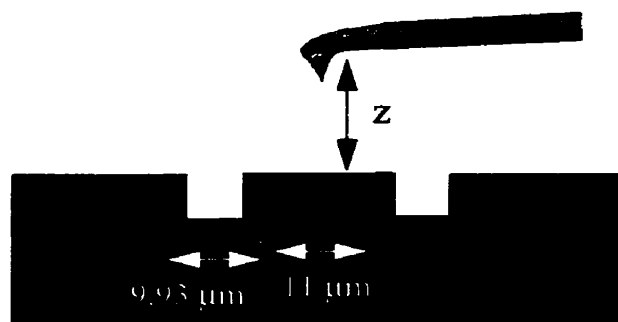


**Fig. 8.9: Variable height measurement on the CPW structure**

This experiment allows us to investigate the dominance of the center conductor signal relative to the parasitic ground conductor signals. Re-arranging eqn. 8.12 derived in the previous section yields

$$A_m(z) = \frac{1}{1 + G(z)} V_c \frac{(F_1(z) + F_2(z))}{F_p(z)} = G(z) \quad (8.13)$$

Using the sensitivity of the null point on probe to circuit spacing,  $z$ , we can obtain a good approximation to the relative size of the  $(F_1 + F_2)/F_p$  ratio.

In Fig. 8.10, the normalized null point vs height is plotted for the CPW. The same experiment was performed over a  $100 \times 100 \mu\text{m}$  pad for comparison.

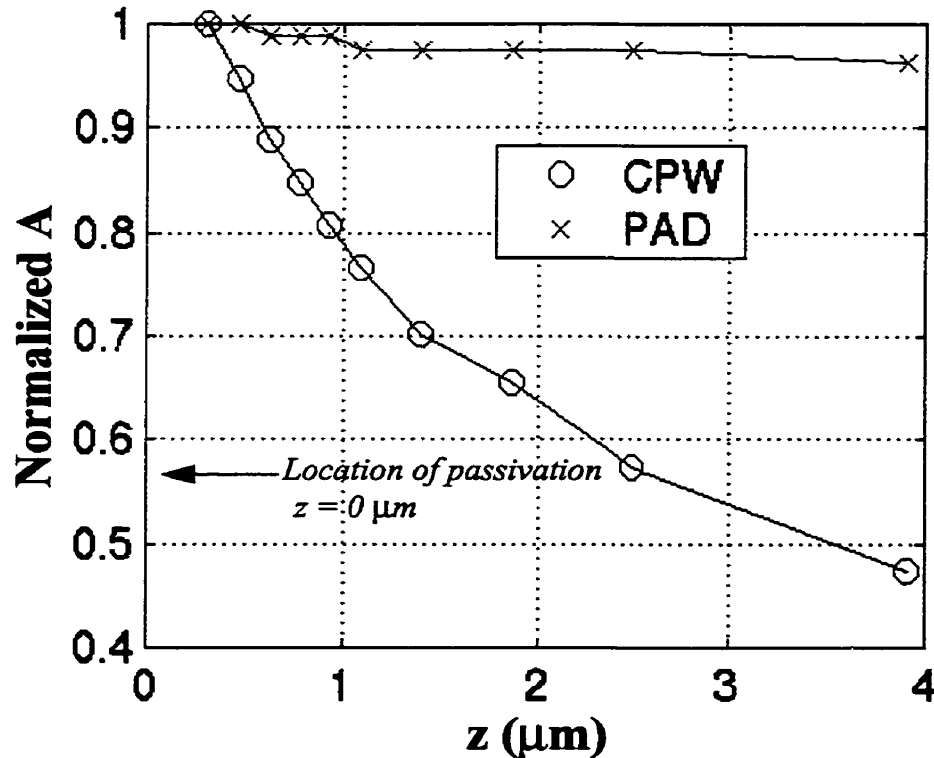


Fig. 8.10: Amplitude null point versus probe to circuit spacing

It is apparent in the case of the CPW structure, the ratio  $(F_1+F_2)/F_p$  is quite significant do to the large variation in null point with probe position. In the case of the 100x100  $\mu\text{m}$  PAD, the entire cantilever probe was overtop the RF conductor where  $F_p$  dominates over any other parasitic weight resulting in very little amplitude sensitivity with position. In the case of the CPW, the parasitic ground planes are much closer and contribute greatly to the measured effective amplitude.

Notice that the null point profile for the CPW in Fig. 8.10 resembles a typical capacitance derivative distribution. This makes sense mathematically if we consider the variation of the weights  $F_k$  with respect to position. In our case, let us assume that the weights can be expressed as

$$A_m(z) = \frac{1}{1 + G(z)} V_c \quad \frac{(F_1(z) + F_2(z))}{F_p(z)} = G(z) \quad (8.14)$$

We will assume that the  $F_p$  characteristic is similar to a parallel plate capacitor as given by

$$F_p = \frac{K}{z^2} \quad (8.15)$$

where  $K$  is some constant. It is reasonable to assume that the parasitic weights of the ground planes are constant in respect to  $z$  relative to  $F_p$  since they are more than 10  $\mu\text{m}$  away.

$$F_1 + F_2 = \text{constant} = B \quad (8.16)$$

A rough sketch of these weights for small probe displacements are shown in Fig. 8.11.

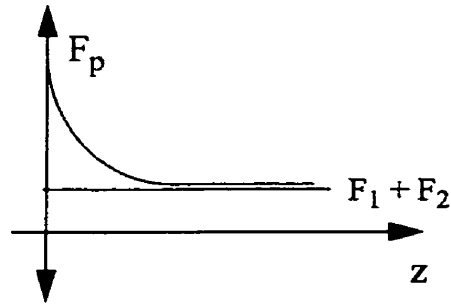


**Fig. 8.11:** Approximate functions for  $F_k$  weights with probe to circuit spacing

If we substitute for  $F_p$  and  $F_1+F_2$  into eqn. 8.14, we can form the amplitude null equation

$$A_m(z) = \frac{1}{1 + \frac{B}{K}z^2} V_c \quad (8.17)$$

This produces a family of curves, as shown in Fig. 8.12, where the slope depends on the relative coupling (ratio  $B/K$ ) between parasitic and measurement conductor.

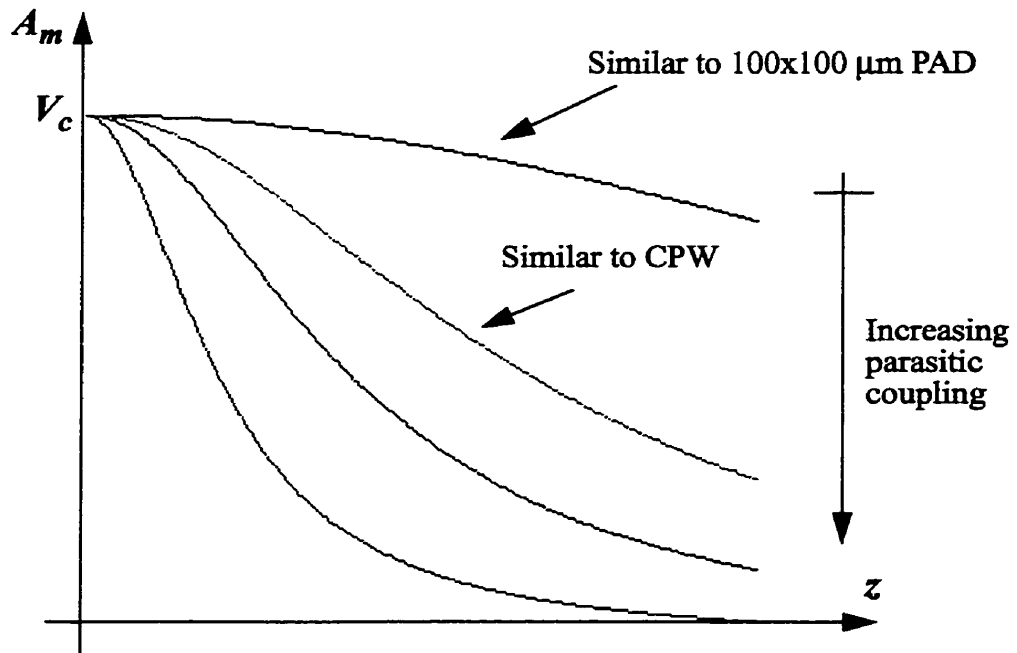


**Fig. 8.12:** Typical nulling trends with variable probe to circuit spacing

The top curve represents a situation similar to probing the 100x100  $\mu\text{m}$  PAD while the second may be more indicative of the small CPW structure.

It is interesting to note the shape of the curve, which can present problems for probing passivated circuits. In the first few chapters, it was mentioned that a positive merit of the nulling technique is that it eliminates the need for accurate probe placement. This was assuming that parasitic conductors were not present during the measurement. In the case of the CPW structure, we can plot the approximate shape of the nulling point gradient of eqn. 8.17 as shown in Fig. 8.13.

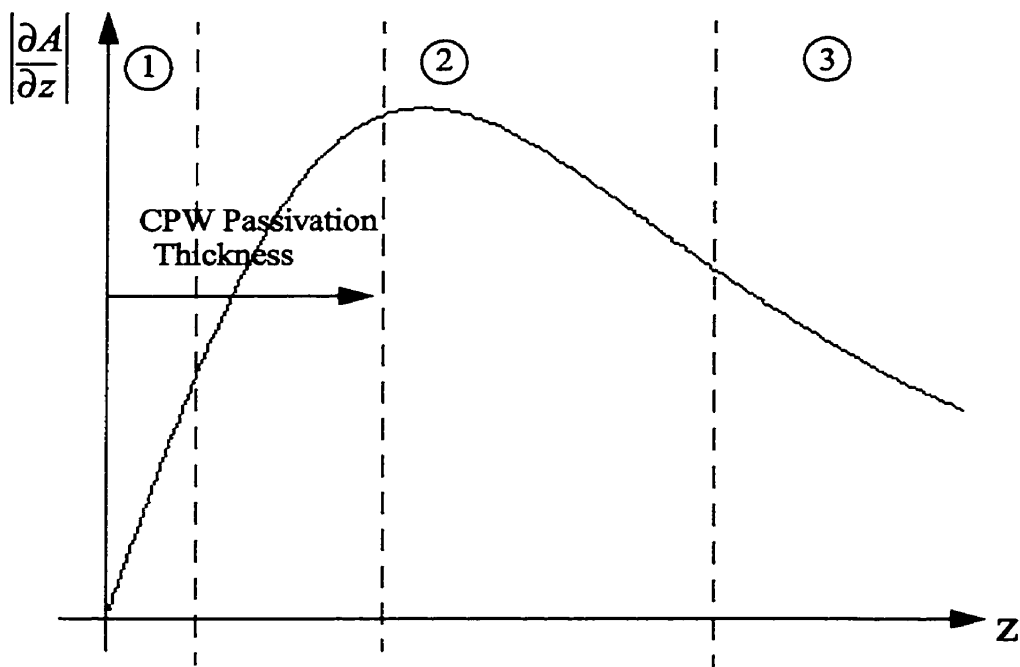


**Fig. 8.13:** Nulling point gradient versus probe to circuit spacing

The curve has been divided into three regions. The first region is when the probe is very close to the circuit where coupling to the target conductor dominates ( $F_p \gg F_k$ ) and therefore the sensitivity is quite small. As we move farther away, we enter region #2 where the sensitivity becomes quite large which is not the desired region of operation.

Lastly in the third region, the slope decreases again but this is a region of poor SNR since the  $F_p$  weight has become too small for good noise performance. Also, the measured amplitude will be an averaged version of the signal on the target and parasitic conductors. In the case of the CPW structure used in this chapter, we are definitely operating in region #2 due to the large slope seen earlier in Fig. 8.10. The passivation point is probably located near the peak of the nulling point derivative profile as shown in Fig. 8.13. Clearly in this case the passivation layer prevents measurements in the desired region #1. In the case of the 100x100  $\mu\text{m}$  PAD measurement, the parasitic effect of other conductors was much smaller therefore we were probably operating in the desired region #1.

It is apparent that the instrument does not have enough spatial resolution to probe a passivated signal line when ground or power conductors are 10  $\mu\text{m}$  away. To achieve better spatial resolution, it may be necessary to probe unpassivated circuits to ensure operation in region #1 of Fig. 8.13.

### **8.5 Summary**

Due to the non-contact nature of the instrument there is always a compromise between invasiveness and spatial resolution. In the case of the passivated CPW structure considered in this chapter, there is not ample spatial resolution. This may require the probing of unpassivated circuits when other parasitic conductors are in close proximity. To ensure ample spatial resolution, it is necessary to place most of the cantilever beam overtop of the measurement conductor as in the case for the 100x100  $\mu\text{m}$  pad seen in this chapter. In digital circuits, interconnect sizes can be several microns in width making this impossible when doing pulse sampling. Fortunately in RFICs, conductor sizes are larger mainly to

accommodate higher current density (bias currents) and power levels which greatly reduces error due to parasitic interaction.

## Chapter 9: Vector Voltage Measurements at 16 GHz

### 9.1 High Frequency Considerations

In this section, we will attempt to perform vector measurements at 16 GHz. There are several considerations to be made before continuing. The first consideration is that the measurement wavelength is becoming increasingly smaller ( $\lambda < 1.9$  cm) which means that any movement of cables and connectors may result in large error in the phase.

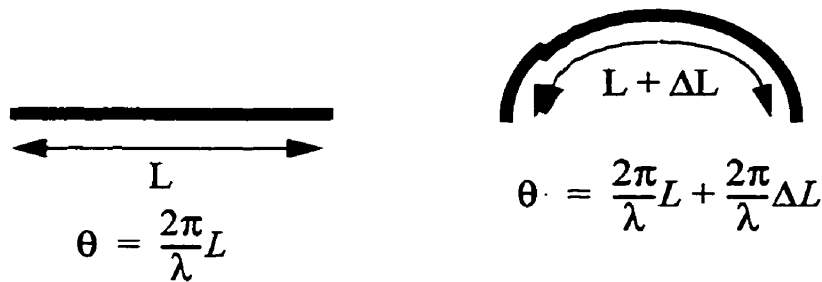


Fig. 9.1: Bending of cables result in changes in electrical length

Whenever a cable is bent, the physical length changes which results in a change in electrical length. At low frequencies when  $\Delta L \ll \lambda$ , the resulting phase shift will be negligible. Unfortunately at higher frequencies like 16 GHz there can be 3 to 4° phase differences by cable bending. Another problem occurs when applying different levels of torque to connectors. Using a network analyzer, the amount of applied torque was varied which results in 10° differences in the measured phase at 16 GHz. These are the kinds of errors which will affect the accuracy of phase measurements during calibration. Fortunately amplitude is not nearly as sensitive which should allow for accurate amplitude measurements.

The second consideration is the increased coupling which should not be a serious problem if small transmission line structures are probed. In chapter 7, probing over the small calibration 50 Ohm CPW results in loading capacitances of a few femptofarads which does not have a significant loading effect at 16 GHz. The loading impedance would be approximately 5 K $\Omega$ , which relative to a 50  $\Omega$  system is still very small. In this chapter the measurement sample will be the calibration 50  $\Omega$  CPW which was used for the 10 GHz measurements. We can estimate the loading impedance using a typical RFIC coupling capacitance value obtained in chapter 7 as indicated in Fig. 9.2.

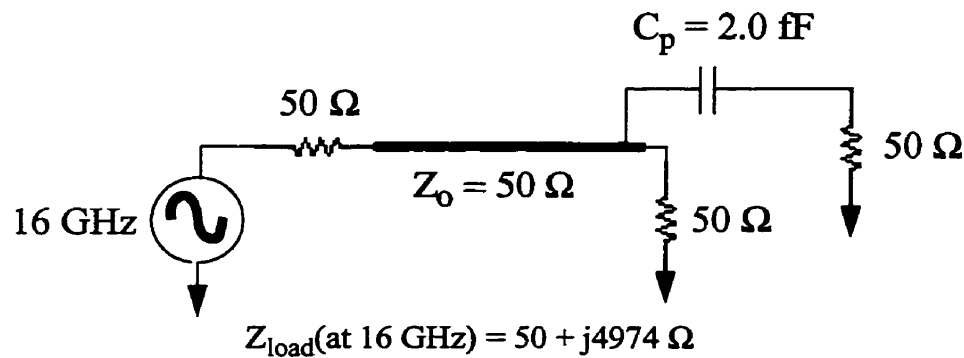
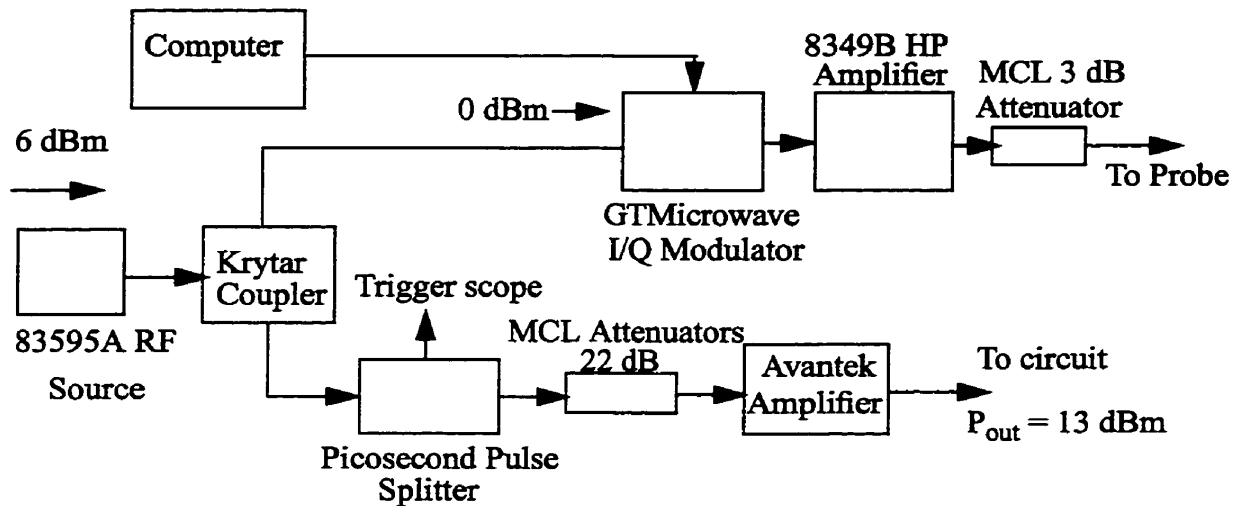


Fig. 9.2: Equivalent circuit at 16 GHz

## 9.2 Hardware Description

Moderate changes have been made to the original 10 GHz measurement hardware to accommodate 16 GHz. The hardware still makes use of the GTMicrowave IQ modulator, HP amplifier and Avantek amplifier. The only changes were the addition of higher frequency power splitters and couplers as indicated in Fig. 9.3.



**Fig. 9.3:** 16 GHz measurement block diagram

In this setup the isolator was no longer needed since a  $180^\circ$  -3 dB hybrid coupler was used as the initial power divider. This component has a -22 dB isolation at 16 GHz which effectively decouples the probe and stimulus circuitry. The source was producing 6 dBm and with the connecting cable loss and the insertion loss of the coupler, there was approximately 0 dBm of input power into the IQ modulator. This was verified using a power meter at the input port. The remaining portion of the probe circuitry is identical to the 10 GHz measurement setup. The circuit stimulus section uses a picosecond pulse power splitter to provide a potential trigger signal to a repetitive sampling oscilloscope. A combination of 22 dB attenuators and output amplifier provides a maximum circuit output power of 13 dBm.

### 9.3 I/Q Modulator Calibration at 16 GHz

For accurate measurements it is required to fully characterize the GTMicrowave I/Q modulator at 16 GHz. The characterization was done using a repetitive sampling oscilloscope as shown in Fig. 9.4.

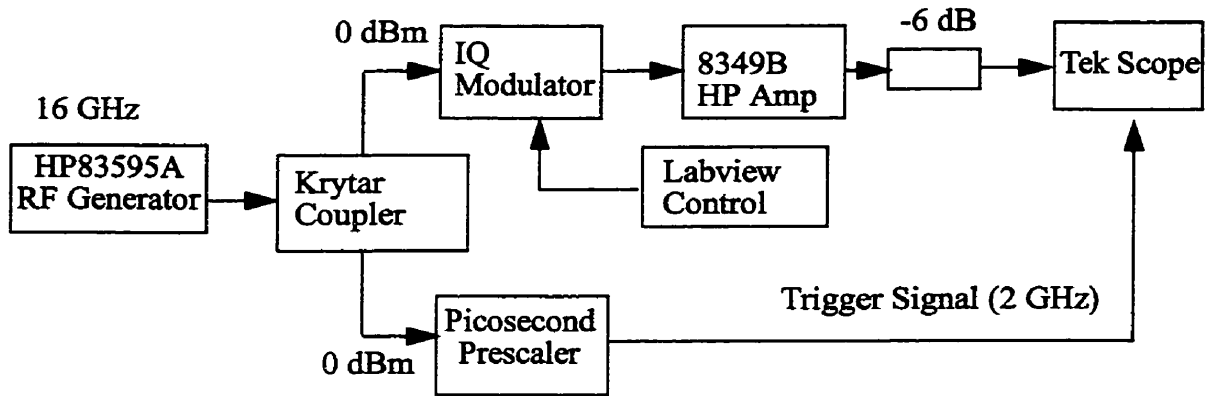


**Fig. 9.4:** *I/Q Modulator characterization setup*

To facilitate measurement of a 16 GHz signal, a divide by 8 prescaler was employed to synthesize a 2 GHz trigger signal. Similar to the 10 GHz measurements, the amplitude and phase was measured along the I and Q axis. The phase measurement was done by capturing a reference waveform at the first measurement instance. The system jitter was measured to be about  $10^0$  at 16 GHz, making accurate phase measurements difficult. The phase is not too important, at least from the oscilloscope it is possible to verify that the phase on the I and Q axis remains constant within  $10^0$ . The measured amplitude characteristic for both the I and Q axis is shown in Fig. 9.5.

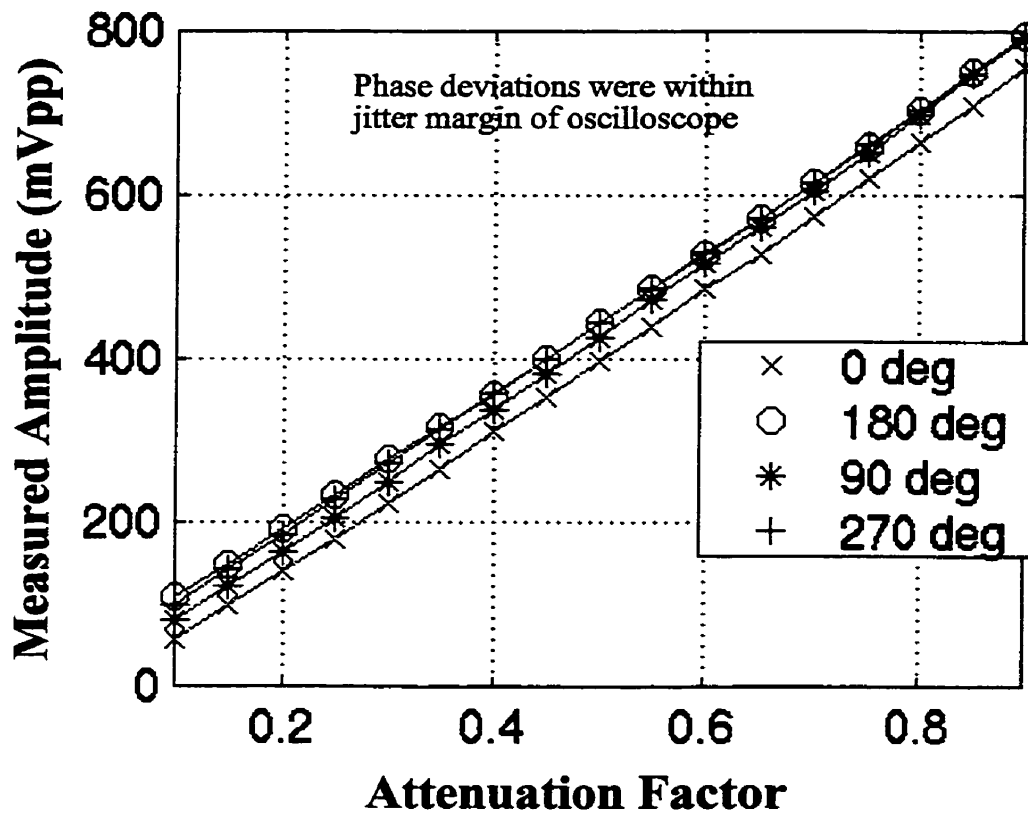
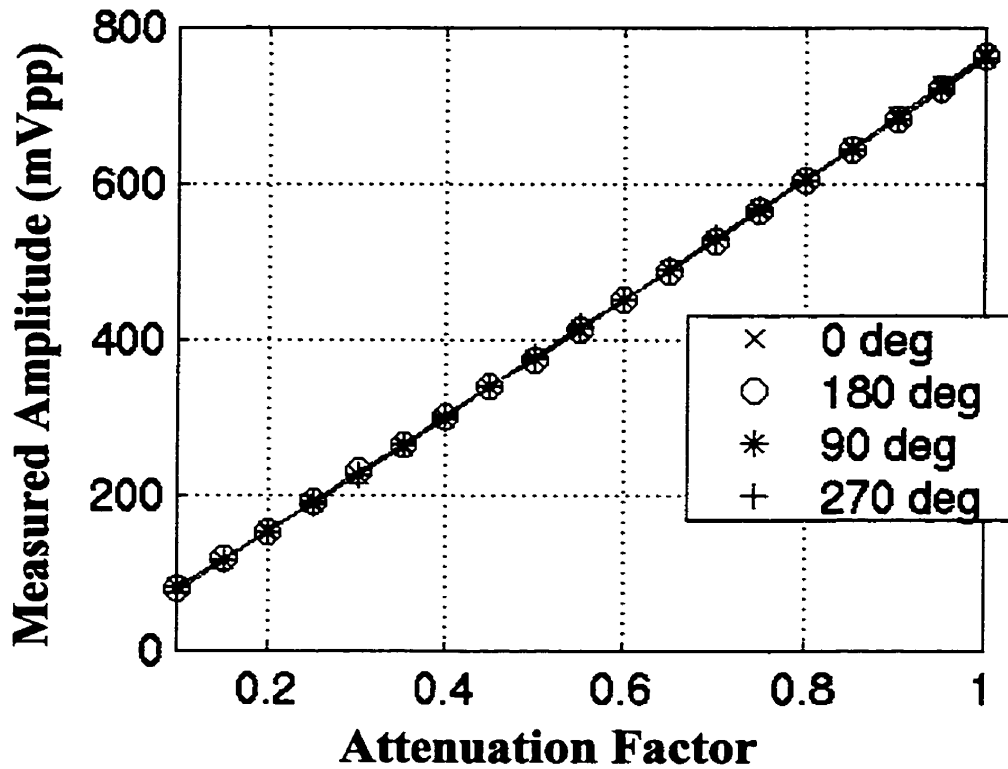


Fig. 9.5: Measured I/Q modulator characteristic at 16 GHz

The phase measurements did not deviate from the jitter margin of the oscilloscope so we will assume that the I and Q axis are phase invariant to attenuation.

Using the same software compensation technique, we can solve for the necessary transformation equations to achieve identical characteristics along both I and Q axis for a given attenuation setting. The resulting plot in Fig. 9.6 demonstrates the software compensated characteristic.



**Fig. 9.6:** *Software compensated I/Q modulator characteristic at 16 GHz*

As before, the software compensation was successful in achieving identical characteristics along each modulator axis.

#### **9.4 Vector Measurements on a CPW Structure**

Vector measurements were attempted at 16 GHz on a small 50 Ohm calibration CPW structure. This structure is identical to the one used in the 10 GHz measurements, having a 70  $\mu\text{m}$  wide center conductor with 30  $\mu\text{m}$  ground spacing on top of a sapphire substrate. Initially, a 4.2 dBm signal was placed onto the transmission line via a matched impedance on-wafer probe. Different attenuators were inserted to vary both amplitude and phase of the signal on the transmission line as shown in Fig. 9.7.

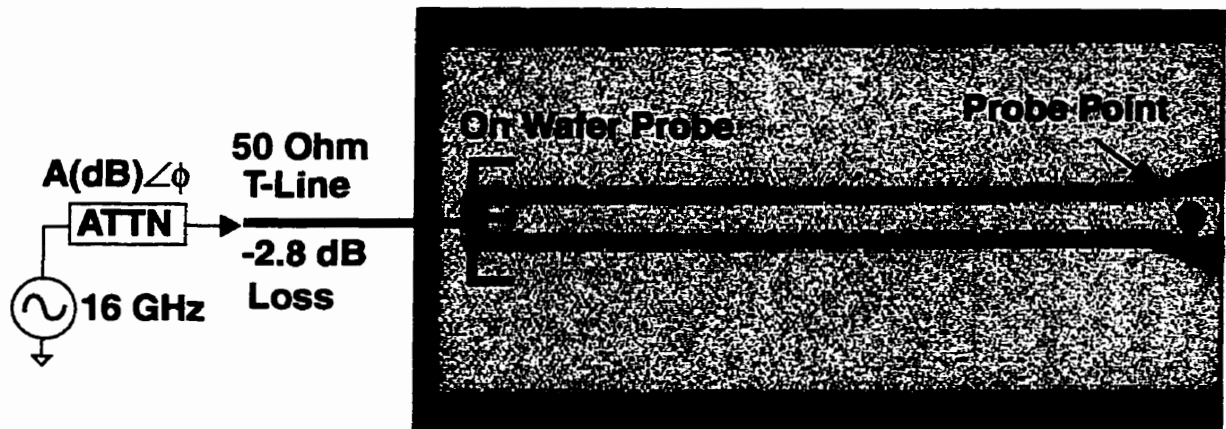


**Fig. 9.7:** 16 GHz measurements on a CPW structure

The 50 Ohm coaxial cable feeding the on-wafer probe has a loss of -2.8 dB at 16 GHz which was verified using a network analyzer. The attenuators were also classified in both amplitude and phase using the same network analyzer as shown in table 9.1.

Attenuator	$A \angle \phi$
-3 dB	-3.5 dB $\angle$ -7°
-6 dB	-6.2 dB $\angle$ -3°
-10 dB	-10.5 dB $\angle$ 5°
-13 dB	-13.4 dB $\angle$ 4°
-16 dB	-16.1 dB $\angle$ 7°
-20 dB	-20.7 dB $\angle$ 48°

**Table 9.1:** Network Analyzer measured attenuator characteristic at 16 GHz

The EFM and network analyzer measurements are shown in Fig. 9.8.

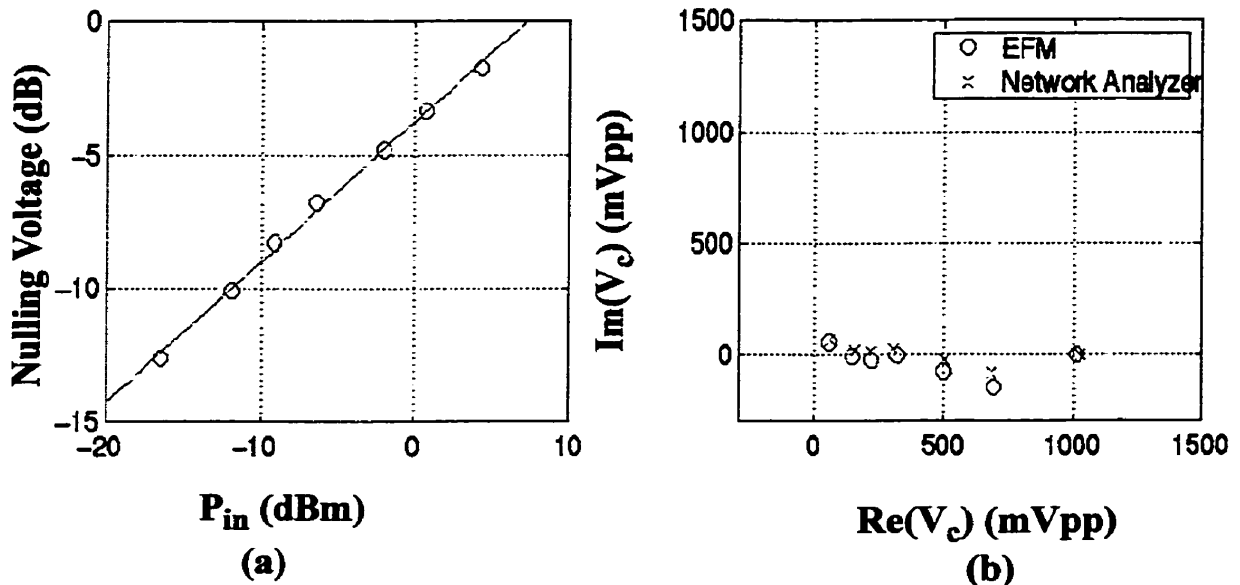


**Fig. 9.8:** EFM versus Network analyzer measurements at 16 GHz

Fig. 9.8(a) demonstrates the normalized nulling voltage(A) vs input power level. As expected the curve is linear over a 20 dB dynamic range. The curve suggests a maximum measurable signal of 8 dBm( $A = 0$  dB) and a minimum lower than -15 dBm. Again the minimum signal depends very much on the proximity of the probe to the circuit and the conductor geometry.

Fig. 9.8(b), demonstrates the measured amplitude and phase in vector space. Notice that the EFM and network analyzer results are in close agreement. The EFM measured phases were within  $8^\circ$  from the network analyzer measurement for each attenuator combination. As mentioned before, we can expect up to  $10^\circ$  of phase variation with combinations of bending cables and torqing connectors.

### 9.5 Measurement of a Wideband Amplifier at 16 GHz

Vector voltage measurements were made on the same distributed amplifier seen earlier in chapter 6. The insertion gain of the amplifier was measured using an HP power meter as shown in Fig. 9.9.

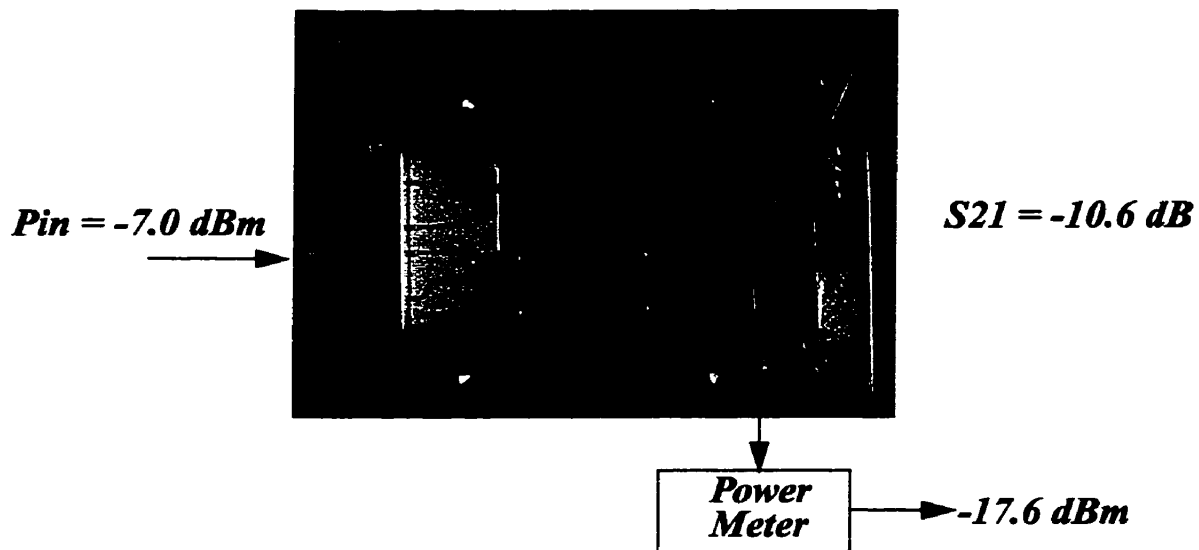
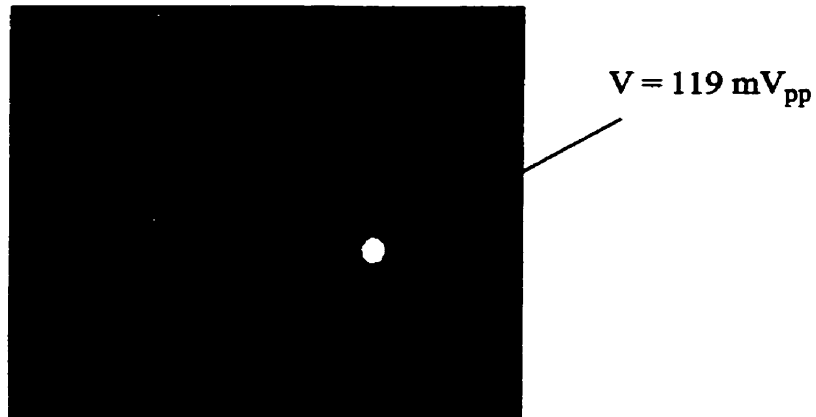


Fig. 9.9: Insertion loss measurement at 16 GHz

The amplifier's performance is very poor at this frequency since it is actually attenuating the input signal by 10.6 dB. The measured insertion loss is within 2 dB of the Nortel measurement of -12 dB from Fig.6.14. Measurements were made on the output transmission line to estimate the insertion loss of the output transmission line. Internal node measurements on the first distributed amplifier stage were also made at 16 GHz.

#### 9.5.1 Insertion Loss Measurement of the Output Transmission Line

The loss of the output line can be estimated by performing an internal node measurement of the output transmission line directly after the output pad and bondwire. The measurement point is indicated in Fig. 9.10.



**Fig 9.10:** Output transmission line measurement at 16 GHz

Using the measured voltage, the output power can be estimated assuming a 50  $\Omega$  system as

$$P_{out} = -14.5 \text{ dBm}$$

Assuming that the output power of the amplifier at the connector is -17.6 dBm as measured using the power meter, the corresponding transmission line loss at 16 GHz is -3.1 dB. Correspondingly, this loss can be factored out of the measured insertion loss to estimate a more realistic  $S_{21}$  to be

$$S_{21} = -10.6 + 3.1 = -7.5 \text{ dB}$$

with port 2 referenced from the output wirebond location. The actual insertion loss is probably smaller since loss on the input transmission line has not been accounted for.

### 9.5.2 Amplitude and Phase Profile of a Distributed Amplifier

Vector voltage measurements of a single 8 stage distributed amplifier were performed as shown in Fig. 9.11. Measurements included amplitude and phase characterization at each stage on both the input and output line as denoted in Fig. 9.11.

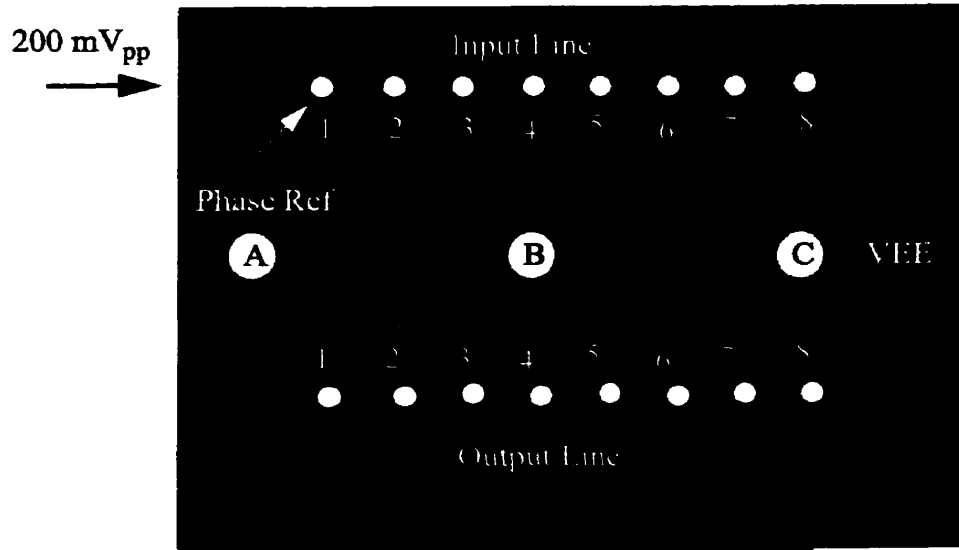


**Fig. 9.11:** Distributed amplifier with sample probing locations

The signal was measured at the input of this amplifier stage which yielded approximately 200 mV<sub>pp</sub> at 16 GHz. Several measurements were performed at various locations along the V<sub>EE</sub> line to investigate power bounce effects at 16 GHz. These are denoted as nodes A,B and C. The amplitude and phase measurements on the input and output line are demonstrated in Fig. 9.12.

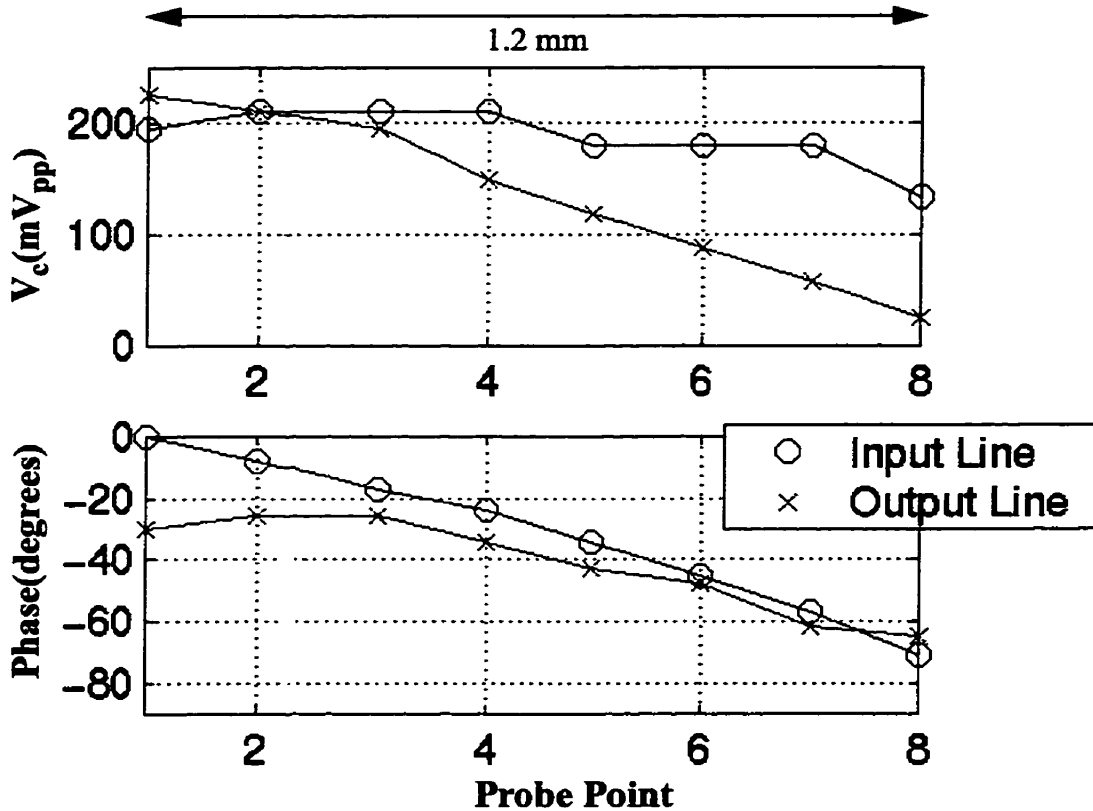


Fig. 9.12: Amplitude and phase measurement of a distributed amplifier

The signal on the input line resembles a travelling wave line since the measured amplitude stays relatively constant around 200 mV<sub>pp</sub> and the phase follows an almost linear characteristic. It appears that the line has an electrical length of 70° at 16 GHz. This is conceivable since the input line is matched terminated to 50 Ohms. The output line has a much different characteristic where the amplitude degrades very rapidly over the entire 8 cells starting from about 200 mV<sub>pp</sub> and dropping by -17 dB. It appears very similar to a standing wave type profile.

Measurements were made at three nodes along the  $V_{EE}$  line as indicated in Fig. 9.11 and Table 9.2.

Node	$V_c(\text{mV}_{pp})$
A	$165\angle-17^\circ$
B	$180\angle-26^\circ$
C	$57\angle-70^\circ$

**Table 9.2:**  $V_{EE}$  line measurements at 16 GHz

It is apparent that there are still large signals on the  $V_{EE}$  line which decay very quickly as we move through the distributed amplifier stage.

### 9.6 Summary

In this chapter, we have demonstrated 16 GHz measurement capability on transmission lines using I/Q modulation. Internal node measurements of a distributed amplifier were also demonstrated indicating a travelling wave distribution on the input line with an electrical length of  $70^\circ$  at 16 GHz. This measurement would be very difficult if not impossible using a contact probe due to excessive loading. Unfortunately, there was no functional circuit available at this frequency with known specifications for comparison.

## Chapter 10: Vector Voltage Measurements using Frequency Upconversion

### 10.1 High Frequency Sinusoidal Measurement

Sinusoidal sampling has the advantage of having a SNR(Signal to Noise Ratio) which is independent of frequency therefore it is suitable for millimeter wave measurements. Assuming the same voltage level, measurements at 1 and 30 GHz will yield the same SNR which is not true in a pulse sampling technique. The question is what are the limitations of this kind of sampling? There are two major limitations, the first being the effects of coupling and second, the availability of high frequency components required to implement the required modulation and phase shifting. It was seen earlier on that the effects of coupling are still negligible for a 50 Ohm system well into the millimeter wave range, therefore loading capacitance is not an immediate problem. The problem of implementing the modulation and phase shifting effectively can present a more urgent problem.

### 10.2 Extending EFM for Higher Frequency Probing

Fortunately, it is possible to utilize all of the same low frequency hardware and software used for the 1 and 2 GHz measurements presented in this research. This can be best explained considering a simple upconversion scheme as shown in Fig. 10.1.

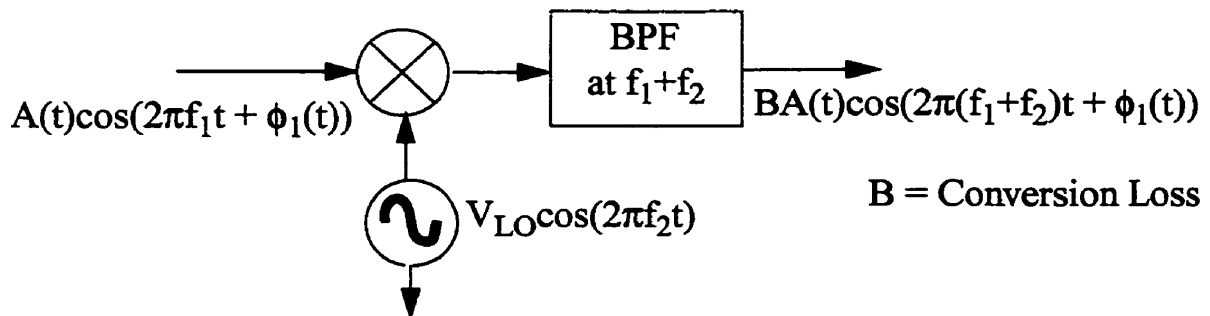
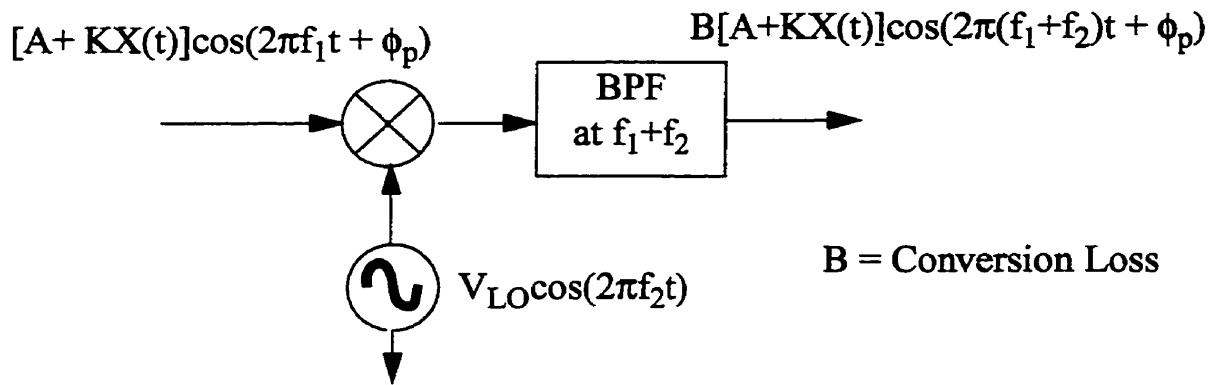


Fig. 10.1: Frequency upconversion scheme

In this figure a sinusoidal signal with both amplitude and phase information is passed through a mixer with a local oscillator. The output is passed through a bandpass filter to pass the upper sideband ( $f_1 + f_2$ ). It is interesting to note that the resulting signal has retained the same amplitude and phase information but has been translated to a higher frequency. This can be applied to the EFM circuitry to up-convert the modulated sampling signal as shown in Fig. 10.2.



**Fig. 10.2:** Upconversion of EFM modulated sampling signal

This technique allows for the use of a lower frequency modulator and phase shifter and up-converts the signal to the desired carrier frequency using an upconversion mixer and bandpass filter. The appeal of this technique is that the same low frequency components can be used for any measurement frequency.

### 10.3 High Frequency EFM Hardware Description

The hardware required is very similar to the version used in earlier chapters except for the addition of the upconversion mixers, filters and amplifiers. A typical high frequency measurement scheme is shown in Fig. 10.3.

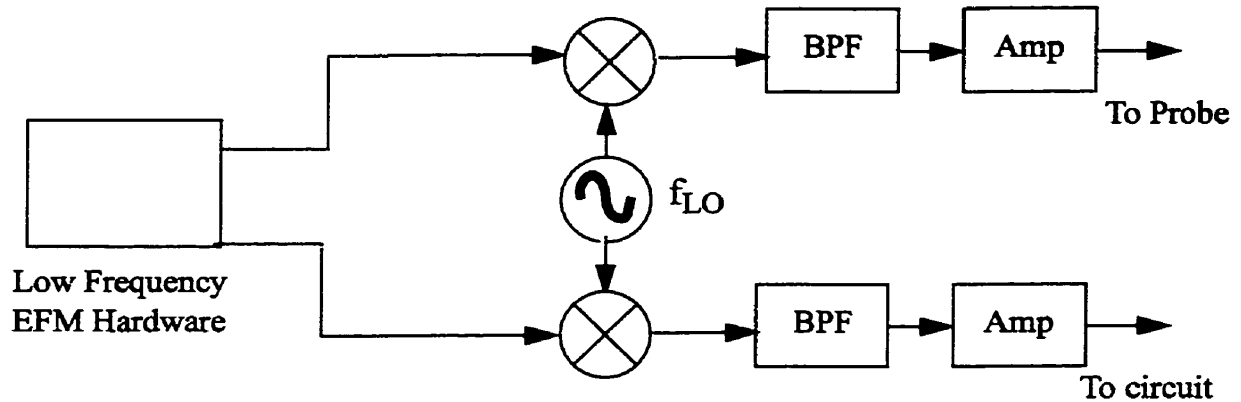
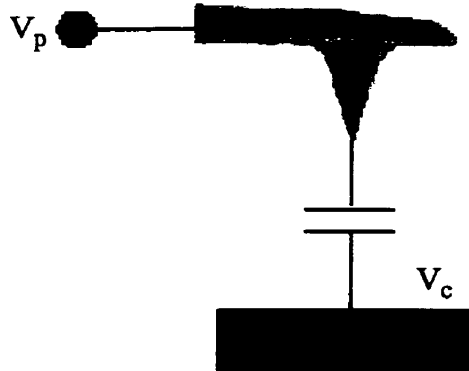


**Fig. 10.3:** High frequency EFM hardware configuration

To overcome conversion loss of the mixers and modulators it will be necessary to use amplifiers at the output stage of both the probe and circuit stimulus sections. This method may reduce dynamic range depending on the linearity of the upconversion mixers. Also the cost of high frequency mixers can approach several thousands of dollars which is a definite disadvantage. Fig. 10.4 demonstrates the expected signals on both the probe and circuit. The probe signal would be comprised of two sampling signals at the two sideband frequencies. The  $\beta$  factor is a measure of the  $f_2-f_1$  sideband rejection of the bandpass filter. It is important to note that the  $f_2-f_1$  frequency results in an reversed phase response due to frequency subtraction. The circuit side would also consist of the two sidebands and if we assume that the circuit under test has the same amplitude response at both sideband frequencies, the lower sideband would also be scaled by  $\beta$ .

$$V_p(t) = [A + KX(t)] \cos(2\pi(f_1 + f_2)t + \phi_p) + \beta[A + KX(t)] \cos(2\pi(f_2 - f_1)t - \phi_p)$$



$$V_c(t) = V_c \cos(2\pi(f_1 + f_2)t + \phi_c) + \beta V_c \cos(2\pi(f_1 - f_2)t + \alpha_c)$$

**Fig. 10.4:** Probe and circuits signals along with associated harmonics

If the above probe and circuit voltage is substituted into the non-linear force equation and solved for the  $f_r$  (resonant frequency of probe) component will yield

$$\Delta z|_{f_r} \propto (A - V_c \cos(\phi_p - \phi_c)) + \beta^2 (A - V_c \cos(\phi_p + \alpha_c)) \quad (10.1)$$

The above equation suggests that for a larger lower sideband rejection, the smaller its effect on the mechanical signal. Due to the square in the force equation, if the bandpass filter has a 20 dB rejection at the lower sideband frequency, the resulting mechanical rejection is 40 dB ( $\beta^2$ ). The deflection characteristic was simulated for different values of  $\beta$  which is shown in Fig. 10.5. The simulation has assumed the worst case phase error where  $\alpha_c$  (from Fig. 10.4) is in quadrature to  $-\phi_c$ .

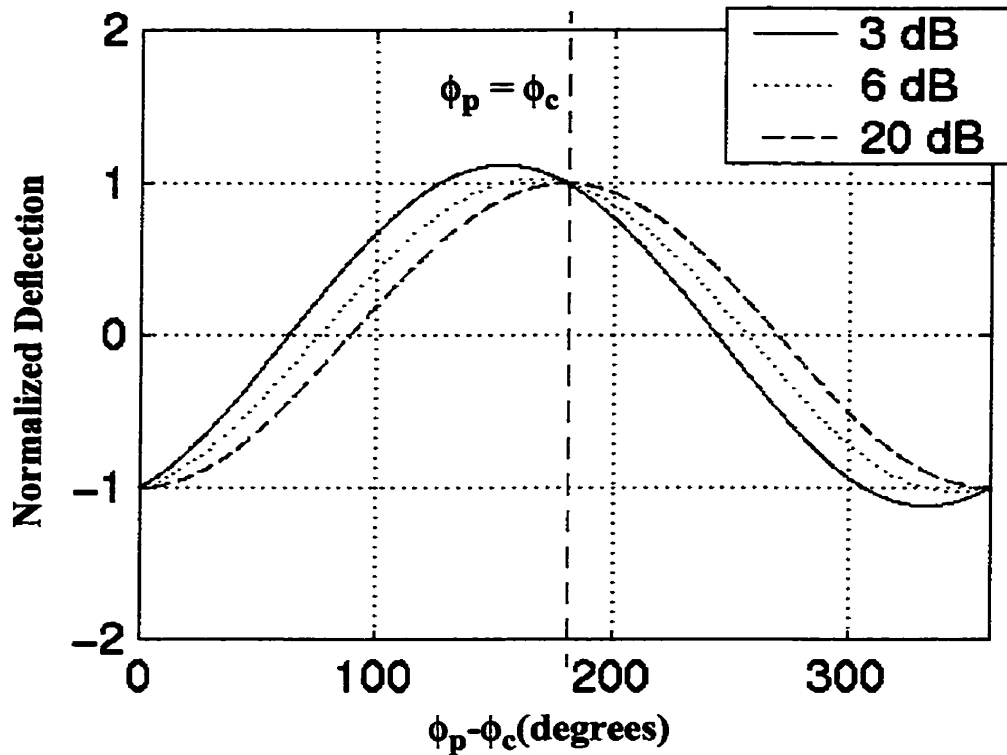


**Fig. 10.5:** Normalized deflection characteristic at different sideband rejections.

For small rejection, the measured sinusoid includes a contribution from both the upper and lower sideband frequencies. As the rejection approaches 20 dB, the contribution of the lower sideband is practically eliminated and the measured phase approaches the desired phase of the upper sideband.

The largest amplitude error will occur when  $-\phi_c - \alpha_c = 180^\circ$  which is tabulated in Table 10.1 along with the maximum phase error from the previous simulation.

$\beta$	$\phi_{\text{error}}$	$A_{\text{null}}$
3 dB	$-30^\circ$	$0.33V_c$
6 dB	$-14^\circ$	$0.59V_c$
10 dB	$-6^\circ$	$0.81V_c$
15 dB	$-2^\circ$	$0.93V_c$
20 dB	$-0.6^\circ$	$0.98V_c$

**Table 10.1:** Simulated phase and amplitude errors under varying sideband rejection

In order to achieve less than  $10^\circ$  error in measured phase, the filter rejection must be larger than 10 dB.

In practice, there are other harmonics present due to LO-RF leakage at integer multiples of the LO frequency. These signals do not possess any modulated components and therefore they are mechanically filtered out by the probe.

#### **10.4 16 GHz Measurements using Frequency Upconversion**

The frequency upconversion technique will be demonstrated by performing vector measurements at 16 GHz. This will be done in comparison to previous measurements made using the I/Q modulation technique (chapter 9). The EFM instrument will be operated at 1.95 GHz and upconverted to 16 GHz using a 14.05 GHz LO source. All amplitude and phase nulling will be performed at 1.95 GHz. The hardware is demonstrated in Fig. 10.6.

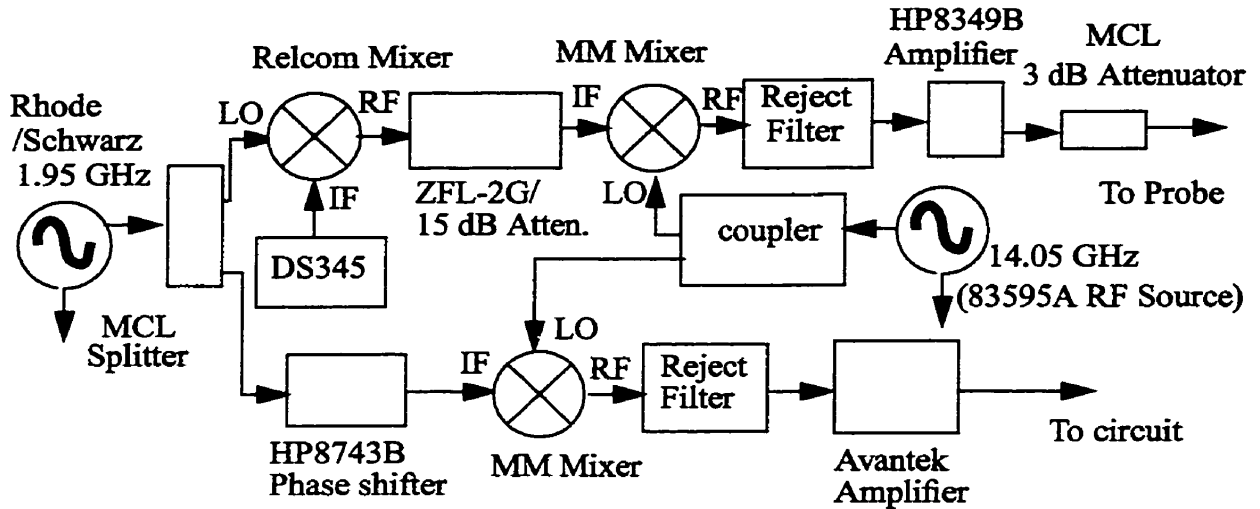


Fig. 10.6: Frequency upconversion hardware block diagram

The selection of LO and IF frequency was done to accommodate the high Q rejection band of the filters for the lower sideband. The low frequency section is driven by the Rhode and Schwarz RF generator which passes through a Minicircuits splitter with one half going to the Relcom mixer and the other through a manual phase shifter. The relcom mixer is used to provide the modulation at the resonant frequency of the probe and implement the amplitude nulling. The modulating signal originates from the DS345 function generator. The output of the relcom mixer is passed through 15 dB attenuation and an amplifier (Minicircuits ZFL-2G) to overcome the conversion loss of the mixer. The 1.95 GHz signals are then upconverted using two Markimicrowave M1R-0920 mixers being driven by a 14.05 GHz LO source. The upconversion results in two sidebands, one being 12.1 GHz that is suppressed using the reject filter and a 16 GHz component which is the measurement frequency of the instrument. The output signals are then amplified and driven onto the probe and circuit.

### 10.4.1 Relcom Mixer Characterization at 1.95 GHz

The relcom mixer was modulated at the IF port using a DS345 function generator which was also used in chapter 4 for the 1 and 2 GHz measurements. The LO port was driven with an input power of 0 dBm at 1.95 GHz. The RF port was connected to a spectrum analyzer as shown in Fig. 10.7.

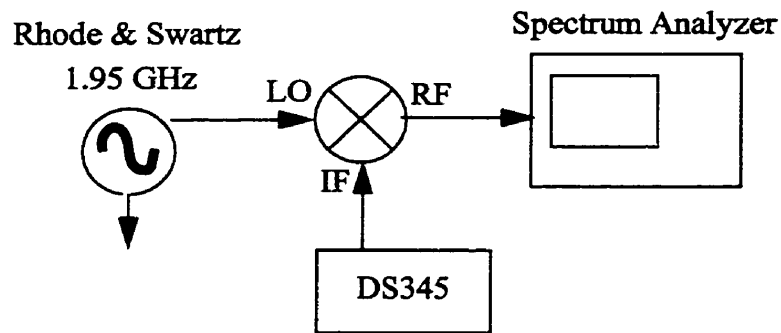


Fig. 10.7: Relcom mixer characterization at 1.95 GHz

A DC IF signal was varied from -120 to 120 mV and the output RMS voltage and power are plotted in Fig. 10.8.

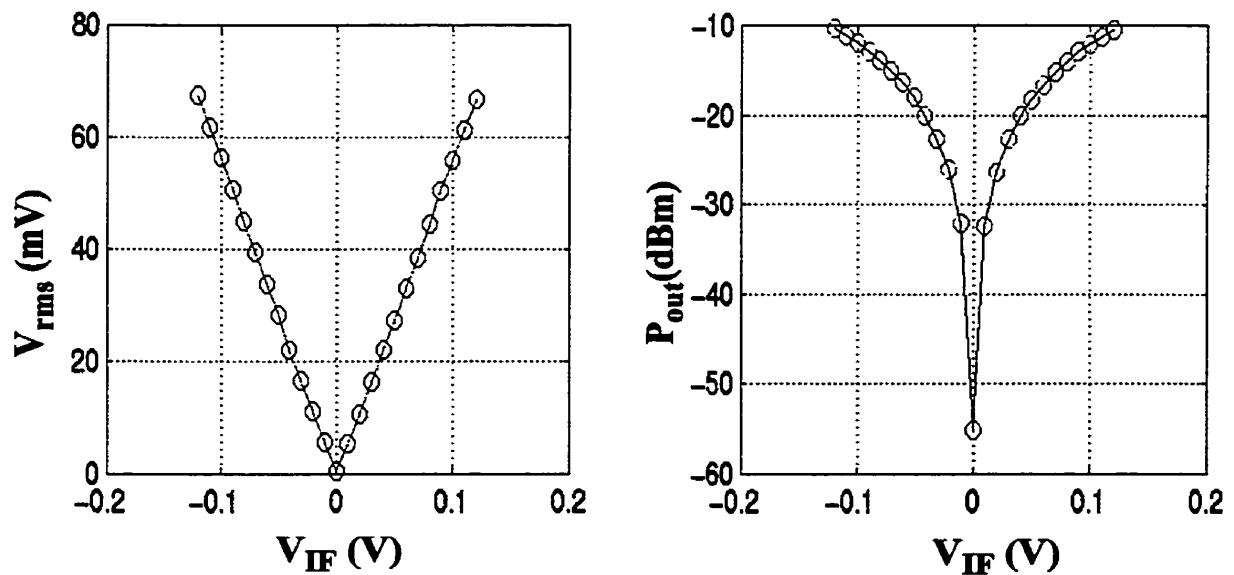


Fig. 10.8: Relcom mixer characteristic at 1.95 GHz

The mixer has a linear characteristic up to and greater than -10 dBm. The leakage power for 0 dBm LO power was measured at -55 dBm which is negligible compared to the -10 dBm of maximum output power.

### 10.4.2 Upconversion mixer characterization

In this experiment, two high frequency mixers provided by MarkiMicrowave were used. The M1R-0920 has a 9-20 GHz bandwidth on the LO and RF and an IF bandwidth ranging from DC to 9 GHz. The mixer has a rated conversion loss of 5 dB with an LO-RF isolation of 35 dB. IF-RF isolation is also a very important consideration in EFM since it will produce a modulated IF signal on the probe. This mixer has a rated IF-RF isolation of 25 dB which should be adequate for this application. This mixer was characterized using an IF of 1.95 GHz and an LO of 14.05 GHz(7 dBm) using a similar setup as shown in Fig. 10.7. A spectrum analyzer was used to measure the output power at the upper sideband (16 GHz) which is plotted along with conversion loss in Fig. 10.9.

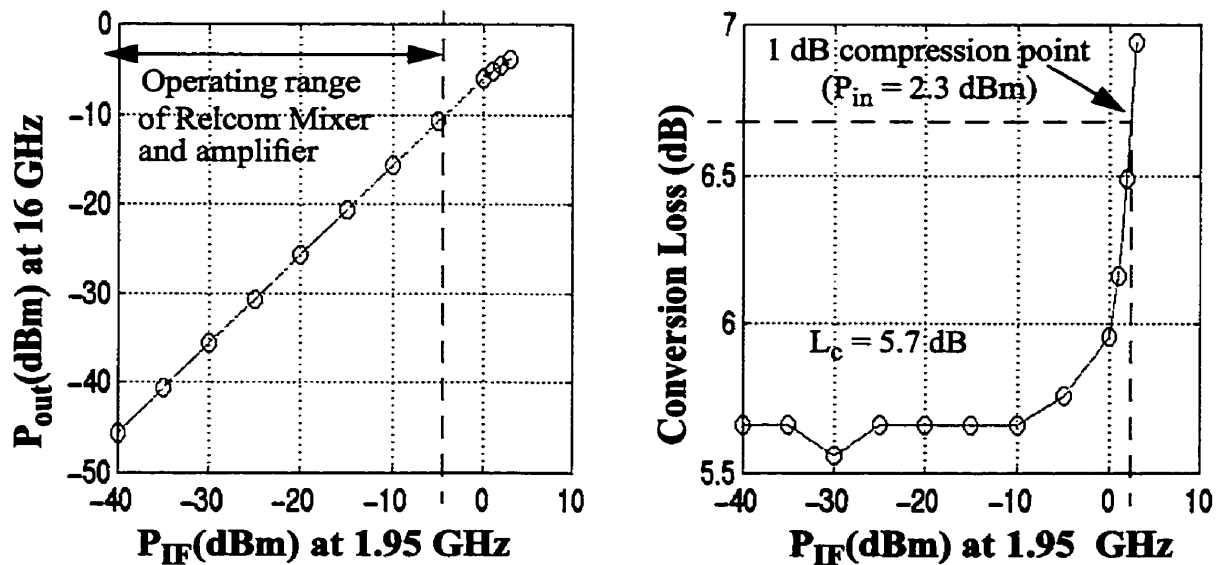
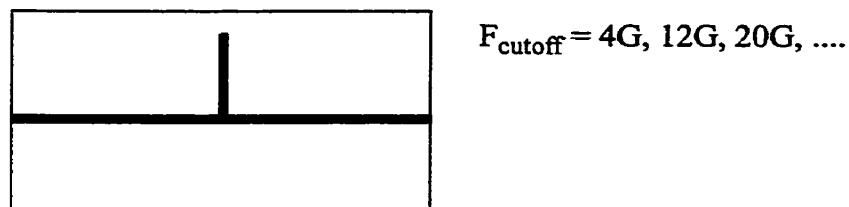


Fig. 10.9: M1R0920 mixer characterization

The measured conversion loss in the linear range was approximately 5.7 dB which is within the tolerance range specified in the data sheet. The input 1 dB compression power was measured to be approximately 2.3 dBm. In the EFM instrument, the maximum input IF power level will be -5 dBm which is well within the linear range of the mixer. The IF to RF isolation was also measured at 1.95 GHz yielding 27 dB isolation relative to the 16 GHz sideband.

### 10.4.3 Sideband Rejection Filters

In section 10.3, the necessity for a lower sideband filter was introduced and in this experiment the 12.1 GHz lower sideband must be suppressed. Since the sidebands are separated by roughly 4 GHz, it is possible to construct a transmission line notch filter which will reject the 12.1 GHz and pass the 16 GHz signal. The filters were implemented using a single open-circuited stub implemented in microstrip as shown in Fig. 10.10.



**Fig. 10.10:** Lower sideband rejection notch filter

The two filters that were constructed had slightly different reject frequencies and the high Q-factor made resonant frequency alignment difficult. Both filters were tuned to a mutual resonant frequency of 12.1 GHz. The insertion loss measurements were performed on both filters at 12.1 and 16 GHz as indicated in Table 10.2.

Filter	Loss (12.1 GHz)	Loss (16 GHz)	Rejection
1	19.36 dB	1.09 dB	18.27 dB
2	18.80 dB	3.40 dB	15.40 dB

**Table 10.2:** Filter insertion loss measurements

It is very difficult to achieve an insertion loss  $< 20$  dB when the frequency exceeds 10 GHz due to losses in the transmission line stub. Recalling section 10.3, eqn. 10.1, we can estimate the amount of rejection on the lower sideband deflection term to be roughly 33.7 dB. The simulated phase error is  $1.4^\circ$  with a worst case measured amplitude of  $0.96V_c$ . It appears that the level of filtering is sufficient for accurate measurements at the upper sideband frequency.

### 10.5 Transmission Line Measurements using Frequency Upconversion

To prove the concept of frequency upconversion, 16 GHz measurements were attempted on the same calibration CPW used in several of the earlier chapters. The CPW along with probe point is demonstrated in Fig. 10.11.

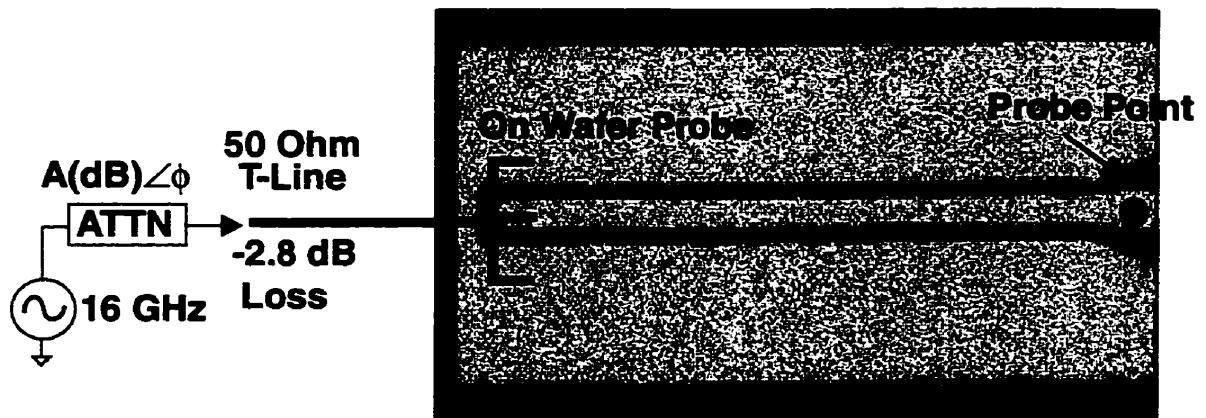


**Fig. 10.11:** Vector measurements of a CPW structure at 16 GHz

The power level and phase was varied using the same calibrated attenuators used in chapter 9 for comparison. Both amplitude and phase was measured and compared to the network analyzer measurements and the results obtained at 16 GHz using the I/Q modulation technique(chapter 9).

### 10.5.1 Phase Measurement

In this technique, the phase shifting was performed by manually adjusting physical length at 1.95 GHz using the HP8743B phase shifter. The phase shift incurred at 1.95 GHz will translate directly to the phase shift of the 16 GHz signal. This was verified by adjusting physical length and measuring the required length for a full period of the 16 GHz signal. The deflection characteristic as a function of added physical length is shown in Fig. 10.12.

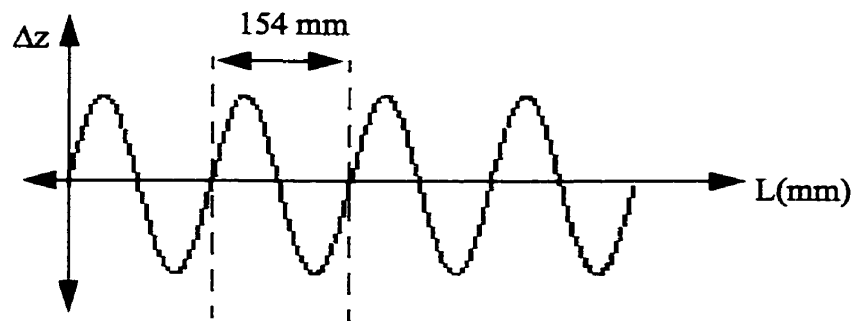


**Fig. 10.12:** Mechanical deflection as a function of physical length

The measured wavelength was approximately 154 mm which corresponds to a full wavelength at 1.95 GHz. This result indicates that a full wavelength shift at 16 GHz can be done by shifting the 1.95 GHz signal by  $360^\circ$ . This proves the concept of phase linearity of the upconversion mixers.

The 16 GHz phase response(relative to 0 dB attenuator phase) of the attenuators was verified and compared to the network analyzer and I/Q modulator measurements in table 10.3.

Attenuator	$\Delta L(\text{mm})$	$\Delta\phi(\text{upconv})$	$\Delta\phi(\text{I/Q})$	$\Delta\phi(\text{VNA})$
3 dB	-2	$-5^\circ$	$-12^\circ$	$-7^\circ$
6 dB	0	$0^\circ$	$-9^\circ$	$-3^\circ$
10 dB	3.5	$8^\circ$	$0^\circ$	$5^\circ$
13 dB	2	$5^\circ$	$-6^\circ$	$4^\circ$
16 dB	3	$7^\circ$	$-4^\circ$	$7^\circ$
20 dB	20	$47^\circ$	$44^\circ$	$48^\circ$

**Table 10.3:** Attenuator phase measurements using EFM and network analyzer

The frequency upconversion technique was successful in characterizing the phase response of all attenuators to within 3 or  $4^\circ$  from the network analyzer measurement. Of course there is about  $10^\circ$  variation in phase due to torquing and moving cables during the measurement.

### 10.5.2 Amplitude Measurement

In this experiment, all amplitude nulling was performed at 1.95 GHz. Using the same attenuators, the input 16 GHz power level was varied over a 20 dB range. Fig. 10.13 demonstrates the normalized nulling voltage(at 1.95 GHz) versus input power level at 16 GHz.

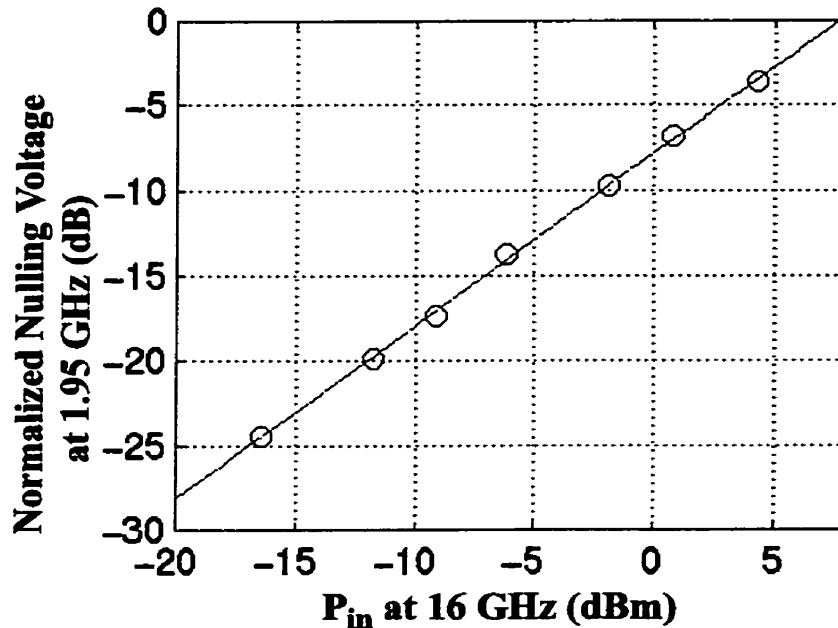


**Fig. 10.13:** 16 GHz power measurements using frequency upconversion

As expected the resulting curve is linear which suggests adequate amplitude linearity in the upconversion mixers. This technique provides a maximum measurable power of 7 dBm and minimum ranging slightly less than -17 dBm. The dynamic range of this instrument is not as high as with the I/Q modulation technique due to more losses in the probe circuitry (mixer conversion loss). A 20 dB dynamic range has been achieved.

### 10.6 Summary

In this chapter, 16 GHz measurements were demonstrated employing frequency upconversion. This technique is desirable since an I/Q modulator can be accurately calibrated (in amplitude and phase) at a fixed low frequency and the LO frequency can be swept to achieve any measurement frequency. The only difficulty will be to provide adequate lower sideband rejection and amplification. The only components which would have to be changed would be the filters and amplifiers to accommodate different frequency

bands. Frequency upconversion would be required to extend the EFM instrument into the millimeter wave arena.

## ***Chapter 11: Conclusions and Future Considerations***

### ***11.1 Concluding Remarks***

In this research we have demonstrated internal node measurement capability from 1 to 16 GHz using both I/Q modulation and frequency upconversion. The nulling technique employed in this research involved modifying parameters of an amplitude modulated single tone signal. This method is similar to repetitive sampling technique #1 mentioned earlier in chapter 2. Vector measurements can also be done using a frequency modulation approach which is similar to repetitive sampling technique #2. In this technique the frequency of the probe signal is increased or decreased by a small IF frequency. Using a lockin amplifier and modifying the reference phase, the entire high frequency sinusoid can be reconstructed. Unfortunately this method is much more complicated to implement in hardware and requires further research.

This research has also demonstrated that EFM has adequate spatial resolution for probing most RFIC conductor geometries. The measured loading capacitance of 2 fF makes the instrument superior to most contact probes available on the market.

## References

- [1] R.Y. Yu, M. Reddy, J. Puhl, S.T. Allen, M. Case and M.J.W. Rodwell, "Millimeter-wave on-wafer waveform and network measurements using active probes", IEEE Trans. Microwave Theory Tech., 43, pp. 721-729, 1995.
- [2] J. Thong, ed., "Electron beam testing technology: microdevices, physics, and fabrication technologies". Plenum, New York, 1993.
- [3] K. Ozaki, H. Sekiguchi, S. Wakana, Y. Goto, Y. Umehara, and J. Matsumoto, "Novel optical probing system with submicron spatial resolution for internal diagnostics of VLSI circuits", Proc. IEEE Intl. Test Conf., Washington, pp. 269-275, 1996.
- [4] R.K. Lai, J.-R. Hwang, and J. Nees, "A Fiber-mounted, micromachined photoconductive probe with  $15 \text{ nV/Hz}^{1/2}$  sensitivity", Appl. Phys. Lett., 69, pp. 1843-1845, 1996.
- [5] G.E. Bridges, "Vector-voltage scanning force probe for non-contact MMIC measurement", Electronics Lett., 35, pp. 1724-1725, 1999.
- [6] Eric W. Sira, Terry Burcham, "Wideband Probing Techniques for Planar Devices", Solid State Technology, August 1989.
- [7] GGB Industries Inc., Naples, Florida, USA. (<http://www.picoprobe.com>)
- [8] Hironori Takahashi, Shin-ichiro Aoshima and Yutaka Tsuchiya, "Sampling and Real-Time Methods in Electro-optic Probing Systems", IEEE transactions on instrumentation and measurement, vol. 44, no. 5, Oct 1995.
- [9] G. Rabbat, "Handbook of Advanced Semi-Conductor Technology and Computer Systems", Chapter 5 Electron Beam Testing, Siemens Research Laboratories, 1988.
- [10] D. Winkler, R. Schmitt, M. Brunner, B. Lischke, "Flexible picosecond probing of integrated circuits with chopped electron beams", IBM J. Res Develop, vol. 34, No. 2/3, March/May 1990.
- [11] Valluri R.M. Rao, and Avtar Saini, "Electron Beam Probing for design verification at Intel", Microelectronic Engineering 24, M.Mittal, 1994.
- [12] Gerhard David, Tae-Yeoul Yun, Matthew H. Crites, John F. Whitaker, Todd R. Weatherford, Kay Jobe, Scott Meyer, Mario J. Bustamante, Bill Goyette, Stephen Thomas III and Kenneth R. Elliot, "Absolute Potential Measurements Inside Microwave Digital IC's Using a Micromachined Photoconductive Sampling Probe", IEEE Transactions on Microwave Theory and Techniques, Vol 46, No. 12, 1998

*References*

- [13] Manoj D. Weiss, Matthew H. Crites, Eric W. Bryerton, John F. Whitaker and Zoya Popovic, "Time-Domain Optical Sampling of Switched-Mode Microwave Amplifiers and Multipliers", *IEEE Transactions on Microwave Theory and Techniques*, Vol. 47, No. 12, 1999
- [14] D.J. Thomson, "24.733 Course Notes", 1999
- [15] NT-MDT Contact Ultrasharp silicon cantilevers CSCS12/W2C Data Sheet
- [16] D. Sarid, "*Scanning Force Microscopy with Applications to Electric, Magnetic and Atomic Forces*", Oxford University Press, Inc., 200 Madison Avenue, N.Y., N.Y. 1991.
- [17] G. Meyer and N.M. Amer, "Novel Optical Approach to Atomic Force Microcopy," *Applied Physics Letters*, vol. 53, no. 24, pp. 2400-2402, 12 December 1988.
- [18] S. Hou, F. Ho, D.M. Bloom, *Electron. Lett.*, Vol. 28, No. 25, 1992, 2302
- [19] C. Bohm, F. Saurenbach, P. Taschner, C. Roths E. Kubalek, *J. Phys. D: Appl. Phys.*, 26(1993)
- [20] A.S. Hou, B.A. Nechay, F. Ho, and D.M. Bloom, "Scanning Probe Microscopy for Testing Ultrafast Electronic Devices," *Optical and Quantum Electronics*, vol 28, no. 7, pp. 819-841, July 1996.
- [21] B.A. Nechay, F. Ho, A.S. Hou, D.M. Bloom, "Applications of an atomic force microscope voltage probe with ultrafast time resolution", *Journal of Vacuum Science*, Vol. 13, No. 3, 1995
- [22] Leyk and E. Kubalek, *Electron. Lett.*, vol. 34, no. 2, 1998, 196-197
- [23] W. Mertin, A. Leyk, U. Behnke, V. Wittpahl, "Contactless Gigahertz Testing", *International Test Conference*, 1998
- [24] J.M.R. Weaver and D.W. Abraham, "High Resolution Atomic Force Microscopy Potentiometry," *Journal of Vacuum Science and Technology B*, vol 9, no. 3, pp. 1559-1561, 1991.
- [25] SR510 Lockin-Amplifier Manual
- [26] C.J. Falkingham, I.R.H Edwards, G.E. Bridges, "Non-Contact Internal-MMIC Measurement Using Scanning Force Probing", *IEEE Intl. Symp. MTT-S*, June (2000)

*References*

- [27] G.E. Bridges, R.A. Said, M. Mittal, D.J. Thomson, "Sampled waveform measurement in integrated circuits using heterodyne electrostatic force microscopy", *Rev. Sci.*, November 1994
- [28] S Rast, C Wattinger, U Gysin, E Meyer, "The noise of cantilevers", *Nanotechnology*, 2000
- [29] TGA8061 Application Note, Texas Instruments
- [30] Canadian Microelectronics Corporation, "GaAs Design Kit V2.1 for Cadence Analog Artist: Design Rules", SAGRF, Northern Telecom
- [31] GTMicrowave, "A Broadband I&Q Modulator", Application note, 2001
- [32] Ian Edwards, "Automated Non-Contact Internal Measurement of High Speed Microwave Integrated Circuits by Method of Electrostatic Force Microscopy", Bsc. Graduation Thesis, 2000
- [33] Raymond S. Kwok, Dawei Zhang, Qiang Huang, Todd Kaplan, Jihong Lu and Guo-Chun Liang, "Superconducting Quasi-Lumped Element Filter on R-Plane Sapphire", *IEEE Transactions on Microwave Theory and Techniques*, May 1999, Vol. 47, No. 5, Pages 586-591
- [34] U. Behnke, B. Wand, W. Mertin, E. Kubalek, "Voltage contrast measurements on sub-micrometer structures with an electric force microscope based test system", *Microelectronics Reliability*, 1999